ABSTRACT

Title of Dissertation:	NEAR-LIMIT SPHERICAL DIFFUSION FLAMES AND COOL DIFFUSION FLAMES
	Kendyl Waddell (Doctor of Philosophy) 2023
Dissertation directed by:	Professor Peter B. Sunderland, Department of Fire Protection Engineering

To combat the rising threats of climate change, current combustion technologies must evolve to become cleaner and more efficient. This requires a better understanding of the fundamental properties of combustion. One way to gain this is through microgravity experiments, where the lack of buoyancy reduces flames to their most basic components, simplifying modeling efforts. The low-temperature combustion of warm and cool flames, which has applications in advanced engine technologies and implications in terrestrial and spacecraft fire safety, is favored in microgravity. In this work, microgravity spherical diffusion flames are generated aboard the International Space Station using a spherical porous burner. A transient numerical model with detailed chemistry, transport, and radiation is used to simulate the flames. This incorporates the UCSD mechanism with 57 species and 270 reactions. Hot, warm, and cool diffusion flames are all studied. Experimental flame temperature was measured using thin-filament pyrometry, which was calibrated using a blackbody furnace. The measured temperatures agreed reasonably well with numerical simulations for a wide range of conditions, and were in the range of 950-

1600 K, with an estimated uncertainty of ± 100 K. The temperatures of the porous spherical burner were measured by a thermocouple embedded in its surface. These measured temperatures, combined with numerical simulations of the gas phase, yield insight into the complex heat transfer processes that occur in and near the porous sphere.

Previous work has found that ethylene microgravity spherical diffusion flames extinguish near 1130 K at atmospheric pressure, regardless of the level of reactant dilution. The chemical kinetics associated with this consistent extinction temperature are explored using the transient numerical model. Species concentrations, reaction rates, and heat release rates are examined. Upon ignition, the peak temperature is above 2000 K, but this decreases until extinction due to radiative losses. This allows the kinetics to be studied over a wide range of temperatures for the same fuel and oxidizer. At high temperature, the dominant kinetics are similar to those reported for typical normal-gravity hydrocarbon diffusion flames. There are well defined zones of pyrolysis and oxidation, and negligible reactant leakage through the reaction zone. As the flame cools, there is increased reactant leakage leading to higher O, OH, and HO_2 concentrations in the fuel-rich regions. The pyrolysis and oxidation zones overlap, and most reactions occur in a narrow region near the peak temperature. Reactions involving HO_2 become more significant and warm flame chemistry appears. At atmospheric pressure, this low-temperature chemistry delays extinction, but does not produce enough heat to prevent it.

As ambient pressure is increased, low-temperature chemistry is enhanced, allowing the flame to extend into the warm flame and cool flame regimes.

Experimental results show that increasing the pressure from 1 atm to 3 atm decreased the ethylene extinction temperature by almost 60 K. Numerical simulations showed similar behavior, as well as the emergence of cool flame behavior when the pressure was increased to 50 atm. This allows the kinetics of spherical warm and cool diffusion flames and the role of increased HO_2 participation to be examined.

There are few options for studying cool diffusion flames experimentally that do not require expensive facilities that are unavailable to the average researcher. A method is presented for observing cool diffusion flames inexpensively using a pool of liquid *n*-heptane and parallel plates heated to produce a stably stratified stagnation flow. The flames were imaged with a color camera and an intensified camera. Measurements included gas phase temperatures, fuel evaporation rates, and formaldehyde yields. These are the first observations of cool flames burning near the surfaces of fuel pools. The measured peak temperatures were between 705 – 760 K and were 70 K above the temperature of the surrounding air. Autoignition first occurred at 550 K.

NEAR-LIMIT SPHERICAL DIFFUSION FLAMES AND COOL DIFFUSION FLAMES

by

Kendyl Askia Coffey Waddell

Dissertation submitted to the Faculty of the Graduate School of the
University of Maryland, College Park, in partial fulfillment
of the requirements for the degree of
Doctor of Philosophy
2023

Advisory Committee:
Professor Peter Sunderland, Chair
Professor Christopher Cadou, Dean's Representative
Assistant Professor Fernando Raffan-Montoya
Professor Stanislav Stoliarov
Professor Arnaud Trouvé

Dedication

To my family, for their constant unconditional love and support.

Acknowledgements

First and foremost, I would like to acknowledge the support and guidance of my advisor, Dr. Peter Sunderland. Beyond his technical expertise, his kindness and understanding were invaluable to me as I pursued this degree against the backdrop of a global pandemic. I could not have asked for a better mentor, and I will be forever grateful.

There are so many people throughout my life without whom this would not have been possible. Countless teachers, coaches, scout leaders, friends, and colleagues have given me help and advice throughout the years. I would like to thank them all for their support.

I would like to give special thanks to the researchers I have worked with over the course of my doctoral studies, including Dr. Axelbaum, Dr. Constales, Dr. Nayagam, and Dr. Yablonsky. I am especially grateful to the members of my dissertation committee, Dr Cadou, Dr. Raffan-Montoya, Dr. Stoliarov, and Dr. Trouve. Thanks to my fellow graduate students, Dr. Philip Irace, Minhyeng Kim, and Han Ju Lee. Thanks to the teams at NASA and ZIN Technologies for helping coordinate and execute the ISS experiments. Thanks to all the undergraduate researchers who helped out in the lab.

Research is impossible without funding, and thanks to NASA and the NSF for funding this work. I would also like to acknowledge the support of the UMD Clark Doctoral Fellowship Program, UMD Flagship Fellowship program, and the GEM Fellowship.

Last but certainly not least, I would like to thank my family for supporting me every step of the way. All of my grandparents, aunts, uncles, and cousins have contributed in ways big and small to making this dream a reality. Special thanks to Austin and Khalil for setting the bar high enough that I had to work hard to clear it, and to Chloe for adding a new dimension to the family dynamic. The biggest thanks go to my parents, who laid the groundwork early and set me up to do whatever I wanted and provided constant love and support my entire life. Love to all.

Table of Contents

List of Tables

List of Figures

Chapter 1 Introduction

Development of the internal combustion (IC) engine paved the way for the massive technological advancements of the 20th century. Due to their high power to weight ratio and the abundance of their fuel, IC engines are widely used for transportation and power generation. However, most of the fuels these engines consume come from non-renewable sources and will eventually be depleted. IC engines also produce many dangerous emissions such as nitric oxides (NO_x) and soot, which are harmful to human health, and carbon dioxide (CO_2), which is a potent greenhouse gas that is warming Earth's climate. Because of this, there is increasing pressure to increase the efficiency of these engines to reduce emissions and fuel demand, or perhaps move away from them altogether. A potential solution exists in the form of electric motors, but these have yet to match the performance and reliability of IC engines in all applications, rely on materials that can be hard to come by, and use electricity that is often still generated by the same fossil fuels it is desired to get away from. To develop cleaner, more efficient combustion technologies, some of the fundamental behaviors of combustion must be better understood. The research in this work focuses on studying the fundamental behavior of near-limit diffusion flames, specifically microgravity spherical diffusion flames and cool diffusion flames above liquid pools.

1.1 A Brief Overview of IC Engines

The first commercial IC engine was built by Belgian-French engineer J. J. E. Lenoir in 1860. It was a spark ignition (SI) engine with a two-stroke cycle, with up to 6 hp and an efficiency of 5% [1,2]. In 1867, German engineer N. A. Otto developed

an atmospheric engine with a two-stroke cycle and an efficiency of 11%. Otto upgraded his design to a four-stroke cycle in 1876, drastically decreasing the weight of the engine while improving the efficiency to 14%. This achievement, in conjunction with an 1884 French patent, built the framework for modern IC engines by laying out the conditions for maximum engine performance and efficiency [1,2]. Although myriad improvements have been made since to reduce weight and increase power and efficiency, this type of engine is similar to those that power the world today.

R. Diesel patented the diesel engine in 1892 [1,2]. This design differed from other engines in that it utilized a much higher pressure, allowing the fuel to auto-ignite rather than be ignited by an external source. This type of engine is known as a compression ignition (CI) engine. CI engines have higher compression and expansion ratios, and are more efficient, than SI engines. However, early diesel engines were louder, larger, and more polluting than gas engines, and thus never became as widely adopted. Modern diesel engines have largely eliminated these problems but are yet to become as ubiquitous as gasoline powered SI engines.

The fuel that IC engines run on is derived from crude oil, a fossil fuel that is extracted from deep below Earth's surface. SI engines typically burn gasoline, a volatile fuel composed of many different midsized hydrocarbons. CI engines typically burn diesel fuel, which is less volatile than gasoline and has a higher energy content. The problem is that crude oil is a finite resource, and eventually the world will need a new method for powering IC engines. By improving the efficiency of these engines, the world's oil supply can be stretched to last longer. Alternative fuels such as natural

gas, alcohols, hydrogen, and synthetic fuels are also considered potential solutions to this problem.

Low thermal losses and high compression and expansion ratios are necessary for improved engine designs. The problem with higher compression ratios is that they lead to knock, a phenomenon where the fuel-air mixture auto-ignites in an uncontrolled fashion, leading to decreased performance and potentially damaging engine components. Knock is controlled by low temperature chemistry. Increasing the octane rating of gasoline helps avoid knock. Early methods of increasing gasoline's octane rating focused on the addition of tetraethyl lead to the fuel. While effective, this method led to elevated levels of lead particulates in the atmosphere, which had dangerous effects on human health. Governments worldwide eventually banned the addition of lead to gasoline, and today's gasoline increases the octane rating through catalytic reformation instead [1,3].

The thermal efficiency of an engine is defined as the amount of energy that is used to do work divided by the amount of energy produced by combustion. Energy that is not used is lost as heat to the environment. Efficiency is controlled by the Carnot cycle and is limited by the lower and upper operating temperatures of the engine. The upper limit on operating temperature is dictated by engine material and fuel auto-ignition properties. If the temperature gets too high the materials used to construct the engine can break down and knock is more likely to occur. Modern diesel engines are 20-40% more efficient than SI engines [2].

1.2 IC Engine Pollutant Emissions

The other main driver behind continued IC engine research, besides increasing efficiency, is decreasing pollutant emissions. The problem of air pollution became apparent in Los Angeles in the 1940s, due to a combination of large population density and natural weather conditions [1,3]. More research into this smog revealed that it was caused in large part by emissions from the tailpipes of automobiles. Main emissions of concern include hydrocarbons (HC), carbon monoxide (CO), nitrogen oxides (NO_x), and particulate matter (PM).

When gasoline is burned in a SI engine, it does not react completely. Different HC compounds are formed through incomplete reactions and expelled as exhaust. Any unburned fuel from the combustion process is expelled as well. Roughly 1-1.5% of the initial fuel ends up as various HCs [2]. In the atmosphere these HCs act as irritants and odorants, and some can be carcinogenic. They also react with other gases to create smog [2,3]. The level of HCs produced in an engine is strongly dependent on the fuel-air ratio. As the amount of fuel relative to the amount of air increases, there is not enough oxygen to fully react with the fuel. This condition often occurs during engine start up and high acceleration. HC production also increases if fuel-air ratio drops below a certain value, such as when an engine misfires. The sweet spot for minimum HC emissions is when there is slightly more air than fuel [1,2]. Another reason for HC emissions is a lack of complete reaction between fuel in oxidizer. This occurs because the two can never be perfectly mixed, and the flame can become quenched as it approaches the walls or at the end of the combustion cycle as the temperature drops. HCs can also be produced when some fuel gets trapped in

crevices in the combustion chamber, when fuel flows directly from the intake to the exhaust, or when fuel or oil get deposited on the walls of the combustion chamber. CI engines have roughly one-fifth the HC emissions of SI engines because they operate at lower fuel-air ratios. Some HC particles condense onto the soot these engines produce and are expelled. These engines also can never have complete combustion, so unburned diesel fuel is emitted. They also suffer from fuel getting trapped in the combustion chamber and fuel and oil deposition [1,2].

CO is produced when engines operate at high fuel-air ratios, since there is not enough oxygen to fully convert the carbon in the fuel to CO_2. SI engine exhaust is approximately 0.2 to 5% CO [2]. Since CI engines operate at low fuel-air ratios, they have correspondingly low CO emissions. CO is a highly toxic gas that can kill if it enters the bloodstream at even very low concentrations [1–3].

NO_x, mostly in the form of NO but with some NO_2, are produced in engines due to high temperatures and the presence of N_2 and O_2. N_2 and O_2 do not react with each other at lower temperatures, but as the temperature rises to the 2500 to 3000 K range, typical engine temperatures, they can react to form NO. The high temperatures cause stable molecules like N_2, O_2, and H_2O to break down to reactive N, O, and OH radicals. These radicals combine to form NO_x. Since NO_x production is dependent on flame temperature, it is highest when the fuel-air ratio is close to stochiometric values. SI and CI engines tend to produce similar levels of NO_x. NO_x is a major precursor in the production of smog. Smog is formed by the photodissociation of NO_2 in the presence of sunlight. Dissociation of NO_2 also leads to the formation of surface level ozone, another dangerous pollutant that is harmful to human health [1–3].

Elevated levels of smog and surface level ozone have been important reasons why NO_x emissions are so closely studied and reduced over the years, and why new technologies to further reduce them are needed.

PM in engine exhaust usually takes the form of solid carbon particles referred to as soot. Soot is formed at high fuel-air ratios when the engine is producing maximum power. Since there is not enough oxygen at these conditions to fully convert the carbon to CO_2, some of the carbon forms soot particles. These particles have a characteristic black color and are more prevalent in CI engines, where they can be controlled by exhaust filters. Soot particles range from 10 to 80 nm [1,2]. PM is small enough that it can enter the bloodstream through the lungs and damage the cardiovascular system.

Once it became clear that these compounds were being emitted from IC engines and had such negative effects, governments began passing legislation that limited acceptable levels of these pollutants. To comply with these new regulations new engine technologies had to be developed. Several of the pollutants mentioned depend on the fuel-air ratio of the engine, but unfortunately not to the same degree. For example, reducing the fuel-air ratio would reduce the amount of CO and PM emissions, but could increase NO_x emissions if reduced too drastically. This is of particular concern in CI engines, where reduction of NO_x leads to an increase in soot formation, and vice versa. Other technologies such as thermal and catalytic converters were developed that convert pollutants to benign forms before they are expelled into the atmosphere. Thermal converters use a heated chamber to oxidize HC and CO emissions to CO_2 before they are expelled. Catalytic converters work in the same

manner but use catalysts to reduce the heat required for oxidation to occur. They also reduce NO_x emissions by reducing NO_x to N_2. Unfortunately, these converters are not perfect, and are particularly ineffective during engine startup as they need time to heat up [1–3]. It is preferable to design engines that avoid producing these harmful pollutants in the first place, although that is easier said than done.

Multiple technologies are in development to increase IC engine efficiency and/or reduce emissions. One method to reduce soot emissions is to dilute the fuel to the point where soot can no longer form. Another method that can reduce NO_x and soot emissions while increasing efficiency is the use of cool flame chemistry to design engines that operate at lower temperatures.

1.3 Microgravity Spherical Diffusion Flames

Microgravity conditions simplify the combustion process by removing buoyancy effects, resulting in a diffusion-controlled process. Flames in microgravity can be considered spherical and 1 dimensional, making them much easier to model than flames in normal gravity. The lack of buoyancy leads to ultra-low strain rates and long residence times that are difficult to obtain in normal gravity environments. Early microgravity combustion experiments employed drop towers or parabolic flights, which have limited durations and can produce less than perfect microgravity conditions. With the launch of the International Space Station (ISS) in 1998, it became possible to study fire in a microgravity environment for long durations.

Previous microgravity experiments have used candles and droplets as fuel sources, but these have inherent limitations and cannot capture all the dynamics of spherical flames. Both candles and droplets have a finite amount of fuel, and the fuel

flow rate is controlled by the heat flux from the flame. The convection direction is always the same, with fuel flowing into oxidizer. A spherical porous burner that supplies gaseous fuel allows greater control of the system since the mass flow rate can be independently controlled, and fuel can be supplied continuously. The convection direction can also be changed independently of the flame structure. The microgravity research here employs a spherical porous burner.

Recent microgravity studies of this type have used ethylene (C_2H_4), ethane, propane, and butane as fuels and focused on radiative extinction, steady state behavior, sooting limits, and cool flames [4–8]. Alongside the experiments, a transient numerical model was employed to examine the aspects of the flames that could not be observed experimentally due to diagnostic or safety limitations. The model allows species concentrations, temperature profiles, and reaction rates to be studied in detail. Chapters 2-4 discuss experimental and numerical results of microgravity spherical diffusion flame research.

Combustion products in microgravity do not leave the reaction zone as quickly, allowing for much higher radiative losses than those seen in typical flames. This leads to a phenomenon known as radiative extinction, where the radiative losses from a flame exceed its heat release, causing the flame to extinguish. Radiative extinction is unique to microgravity flames. It has been shown, using experiments performed aboard the ISS as well as numerical results from a model that is also employed here, that C_2H_4 spherical diffusion flames at atmospheric pressure radiatively extinguish at a constant flame temperature and fuel mass flux [5]. The

kinetics that lead to this consistent extinction behavior are discussed in Chapter 3, and the effect of increasing ambient pressure is examined in Chapter 4.

The logical next question after determining that microgravity flames exhibit this unique extinction behavior is: is it possible to avoid this point and produce a flame that exists as long as fuel is supplied? If the radiative losses from the flame no longer exceed its heat release, and temperature is no longer dropping, then the flame has reached steady state. The existence of steady state flames has been the topic of numerous studies without a definitive answer [9–11], and is of fundamental importance to spacecraft fire safety. The most recent study on this topic, based on the same experimental configuration and numerical model considered herein, concluded that steady state flames can exist in the presence of radiation [6].

Cool flames produce temperatures much lower than their hot flame counterparts and are governed by low temperature chemistry. Cool flames play a crucial part in hot flame ignition, and there are emerging engine technologies that rely on low temperature combustion [12,13]. Since cool flame formation is favored in microgravity, a good understanding of their behavior is important for spacecraft fire safety. In 2021, spherical cool diffusion flames were observed aboard the ISS using a spherical porous burner for the first time [7]. The fuel for these experiments was butane, and cool flame formation was only observed for a narrow range of conditions.

At the center of all three of the previously mentioned microgravity studies is the spherical porous burner. This burner is heated by the flames and can transfer this heat back to the flames as they weaken. The amount of heat transferred to the burner affects the flame temperature and is therefore highly relevant when studying

extinction and steady state flames. A heated burner is also critical to cool flame ignition, as all cool flames observed in [7] required elevated burner temperatures to ignite. Therefore, the need to understand the heat transfer between the burner and the flame is paramount. It is also an important consideration when modeling these flames, as the burner surface defines the inner boundary. Chapter 2 discusses the behavior of the porous spherical burner and the effect it has on overall flame properties.

Another critical measurement for the three studies mentioned is the flame temperature. The most common way to measure temperature is with thermocouples, but these have their drawbacks. They can cause large disturbances in a flame by causing local extinction due to heat losses and only measure temperature at one spot at a time. Because of these limitations, it is preferred to use other temperature measurement techniques that are less intrusive and provide spatial data. One such technique is thin-filament pyrometry (TFP). TFP works by inserting small (14 μm in the present work) silicon carbide (SiC) fibers into the flame. These fibers glow when heated, and the intensity of the glowing can be related back to temperature using a properly calibrated camera. In Chapter 2 the calibration procedure, conducted using a blackbody furnace, for the camera used during the experiments is described, along with the analysis of TFP images and the resulting flame temperatures. The TFP method described here was used to obtain the flame temperature measurements in [4], and were also used to help confirm the presence of cool flames in [7].

1.4 Cool Pool Diffusion Flames

Low temperature combustion relies on the chemistry of cool flames, which were first experimentally observed in the early 19th century by Davy [14]. In the

centuries since, understanding of these flames has evolved along with advances in experimental and numerical techniques. Cool flames have temperatures of only 500 – 1000 K [12], and only increase local gas temperature by 2-200 K [15]. They are also characterized by low reactant consumption and large production of formaldehyde [16,17].

Recently, low-emission engine technologies such homogeneous charge compression ignition (HCCI), premixed charge compression ignition (PCCI), reactivity controlled compression ignition (RCCI) engines have been studied. HCCI engines inject well-mixed fuel and oxidizer into the combustion chamber much in the same way that SI engines do, while the injection method for PCCI engines is based on CI engines. RCCI engines use a mix of fuels with different reactivities to combine low and high temperature effects. In these engines, autoignition of cool flames is an integral part of the combustion process [18–26].

Low temperature combustion (LTC) engines operate on the same fundamentals as SI and CI engines, in that thermal energy released from a combustion process is used to produce work. LTC engines are types of CI engines, meaning no external spark is used to ignite the fuel. The fuel air mixture is compressed to the point that auto-ignition occurs, but the key difference is that this auto-ignition is of a cool flame, not a hot flame. This is achieved by the use of very low fuel-air ratios. In an LTC engine, ignition occurs in multiple locations throughout the mixture simultaneously. The pressure increase in this type of engine thus occurs much faster than in CI engines, while the temperature increase is much lower. Thus, LTC engines

benefit from high compression ratios while reducing heat losses to the walls of the combustion chamber, due to a smaller difference in temperature [21,22,24,25].

LTC engines also benefit from a reduction in some of the harmful emissions associated with IC engines, especially NO_x and PM [18–26]. Both pollutants require high temperatures to be produced, higher than the peak cool flame temperatures of ~1000 K and are highly reduced in LTC engine exhaust. LTC engines have been shown to reduce NO_x emissions by three orders of magnitude and soot emissions by a factor of six compared to diesel engines, while operating at a 16% higher efficiency [22]. These engines can also run on a wide variety of fuels, any fuel that exhibits cool flame behavior could theoretically be used.

The development of LTC engines also has its challenges. The ignition in LTC engines cannot be precisely controlled as in SI and CI engines. This makes it difficult for the engine to perform under a wide range of operating conditions. At high loads, HCCI and PCCI engines experience unacceptable levels of noise and knock. This problem is being addressed with RCCI engines, which combine the properties of low and high temperature combustion to achieve higher efficiency at a wide range of conditions. Due to the lower heat release from LTC the engines suffer from a reduced power output, limiting the technology to lower duty applications. Cool flames also suffer from low reactant consumption and thus LTC engines have increased HC and CO emissions compared to SI and CI engines. The temperatures are low enough that HCs trapped in crevices or along the walls of the combustion chamber do not ignite, and CO is not oxidized to CO_2. LTC engines also emit several compounds in large quantities that CI and SI engines do not. Chief among these is formaldehyde, a known

irritant and carcinogen. Formaldehyde can also lead to production of surface level ozone. Polycyclic aromatic hydrocarbons are another emission of concern due to their carcinogenic properties [24]. To address these problems, a better understanding of the cool flame chemistry that governs these engines is required. This would allow detailed models to be developed to test the performance of these engines in a wide range of conditions. Cool flames can also exist outside of the normal flammability limits for hot flames, making research into their behavior important for fire safety.

To better understand cool flames and their applications, they must be studied and modeled by a wide range of researchers. Most cool diffusion flame (CDF) studies have been performed using equipment and resources not available to the average researcher. Microgravity droplet and spherical burner experiments require years of planning and are only available to a select few, and the number of experiments that can be performed is limited. Other works in normal gravity have employed expensive counterflow configurations and often require the addition of ozone or plasma to ignite the flames. In Chapter 5 a novel method for producing cool diffusion flames from liquid pools using an inexpensive parallel heater setup is described. These experiments lay the groundwork for continuing research of CDFs that will enhance current chemical kinetics models.

Chapter 2 Experimental Observations of Spherical Diffusion Flames

2.1 Introduction

There have been numerous studies on the dynamics of burner supported spherical diffusion flames in microgravity. These flames are supported by a spherical porous burner, as the flame burns, heat is lost to the burner and its temperature rises. No study to date has modeled the temperature of the porous sphere, all previous studies have chosen to either keep the temperature constant or use the experimentally measured values. Atreya and colleagues [27–30] assumed all heat added to the burner heated the fuel gas, and the burner temperature remained constant. The burner temperature was also held constant in works by Santa et al. [31,32] and Lecoustre et al. [33–35]. These works all focused on numerical simulations of experiments carried out in the NASA 2.2-s drop tower, where the times were too short for the burner temperature to rise significantly. Mills and Matalon defined a parameter that describes the burner heat transfer and examined its effects on flame properties in [9], and assumed the burner temperature remained constant in [10]. Tse et al. [11] examined effects of heat loss to the burner by conduction, but computationally held the burner temperature constant or used the experimental burner temperature. Irace et al. [4] prescribed the experimental burner temperature for simulations and showed how the flame properties change if burner temperature is held constant. Markan et al. [36,37] did model the heat flux to a burner in microgravity, but the burner in that case is non-spherical, and the surface temperature was assumed to be constant.

Thin-filament pyrometry (TFP) is a temperature measurement technique that has been studied for many years. It involves inserting a fiber, usually made of SiC, into a hot gas, and converting the brightness of the glowing fiber to temperature. The local gas temperature is found from the fiber temperature using a radiation correction. TFP is less obtrusive than thermocouples and yields linewise, rather than pointwise, temperatures. The technique and the theory behind it are described in depth by [38] and [39]. In previous works, TFP has been performed using either a thermocouple calibration or two-color ratio pyrometry. Here, TFP was calibrated directly from blackbody measurements.

2.2 ACME Chamber Insert

2.2.1 Chamber Configuration

Microgravity experiments were performed aboard the International Space Station (ISS) in the Combustion Integrated Rack (CIR) as part of the Advanced Combustion via Microgravity Experiments (ACME) project. The ACME chamber insert is shown in Fig, 2.1 below with labels indicating the relevant diagnostics. Note that the electrode mesh in Fig, 2.1 was used in other experiments but was not present during the current work.

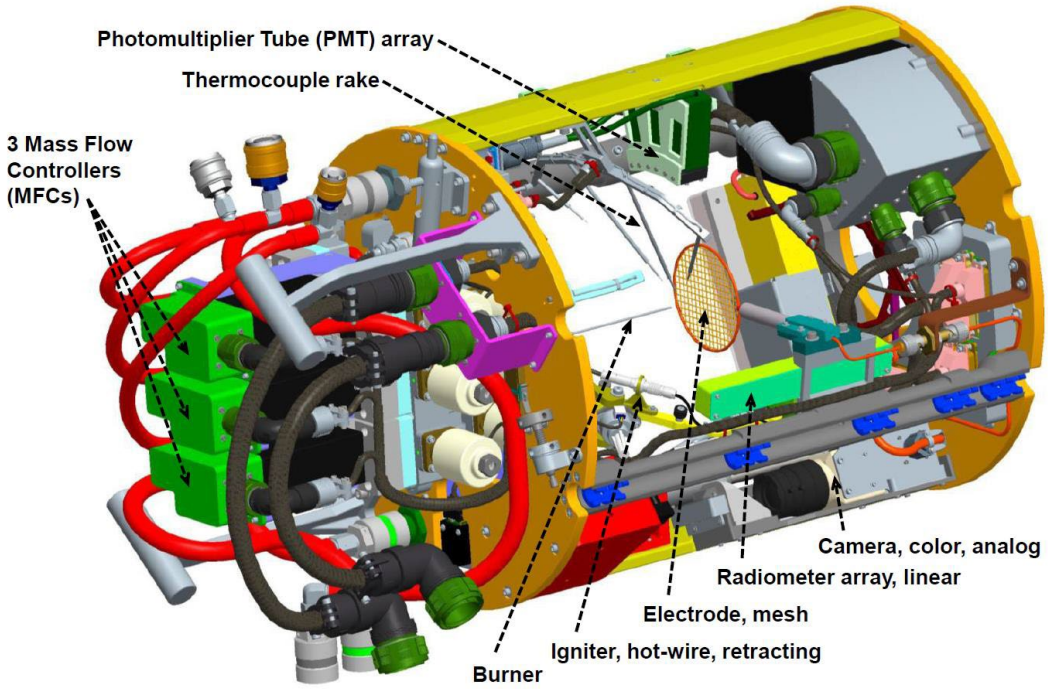

Fig, 2.1. Model of ACME chamber insert, with labels for relevant diagnostics.

Fuel/oxidizer/diluent was delivered to the burner using 3 separate mass flow controllers (MFCs). Fuels used include ethane (C_2H_6), ethylene (C_2H_4), propane (C_3H_8), and butane (C_4H_{10}). The oxidizer was oxygen (O_2), and the diluent was nitrogen (N_2). Both normal (i.e., fuel flowing into oxidizer) and inverse (i.e., oxidizer flowing into fuel) flames were studied. Only diffusion flames were studied, fuel and oxidizer were never fed to the burner at the same time. Uncertainty in the MFCs is estimated to be ± 5%. Chamber pressure varied from 0.5 to 3 atm.

The burner was a 6.4 mm diameter porous stainless-steel sphere to which fuel is supplied via a 1.17/1.5 mm (inside/outside diameter) tube. For increased strength, this was encased in a larger 1.6/1.83 mm (inside/outside diameter). The porous sphere was constructed by sintering together sintered disks of 316 stainless steel with 10-micron media grade. The porosity of these disks is approximately 41% and the

density is 4.6 g/cm3. The porosity of the porous sphere is unknown but is expected to be 1.5-2x higher than the porosity of the individual disks. The supply tube extends to the center of the sphere and, neglecting the interior of the supply tube, there is presumably no cavity within the porous sphere.

The temperature of the porous sphere was measured using a sheathed 0.25 mm diameter type-K thermocouple embedded approximately 1 mm into the burner. An image of the burner prior to installation is shown in Fig. 2.2 below.

Fig. 2.2. 6.4 mm diameter spherical burner used for microgravity experiments. A 0.25 mm type-K thermocouple is embedded in the burner surface.

2.2.2 Diagnostics

Fig, 2.1 also shows the locations of key diagnostic equipment in the ACME chamber. These include Photomultiplier tubes (PMTs), thermocouples, radiometers, and cameras.

Three PMTs were used to measure light emissions from the flames. Their construction was identical, and they are differentiated by the filters used, which corresponded to specific wavelengths. PMT1 had an OH* filter with a wavelength of 310 nm, PMT2 had a broadband filter, and PMT3 had a CH filter with a wavelength of 430 nm. These PMTs had an adjustable gain for detecting a wide range of experimental conditions.

Six far-field thermocouples were present during the experiments. Two of the thermocouples were located 200 mm from the center of the burner and were present for all experiments. The location of the other four thermocouples depended on whether the short or long thermocouple rake was installed. For the short rake, they were 45, 60, 100, and 100 mm from the center of the burner. For the long rake, they were 13, 25, 50, and 100 mm from the center of the burner. The two innermost thermocouples were type-B, and all others were type-K. All thermocouples had wire diameters of 0.2 mm. While the bead diameters were not measured, they are estimated to be 0.4 mm, twice the size of the wire diameter.

Thermopile radiometers were used to measure radiative emissions and were installed at various angles to capture the full flame. No filter was installed on the radiometers, and they were calibrated using a blackbody furnace.

Four cameras were installed in the ACME chamber, their configuration is shown in Fig. 2.3. Three were used to capture flame images. The operations camera is an analog camera that recorded color video of the flames and transmitted them to

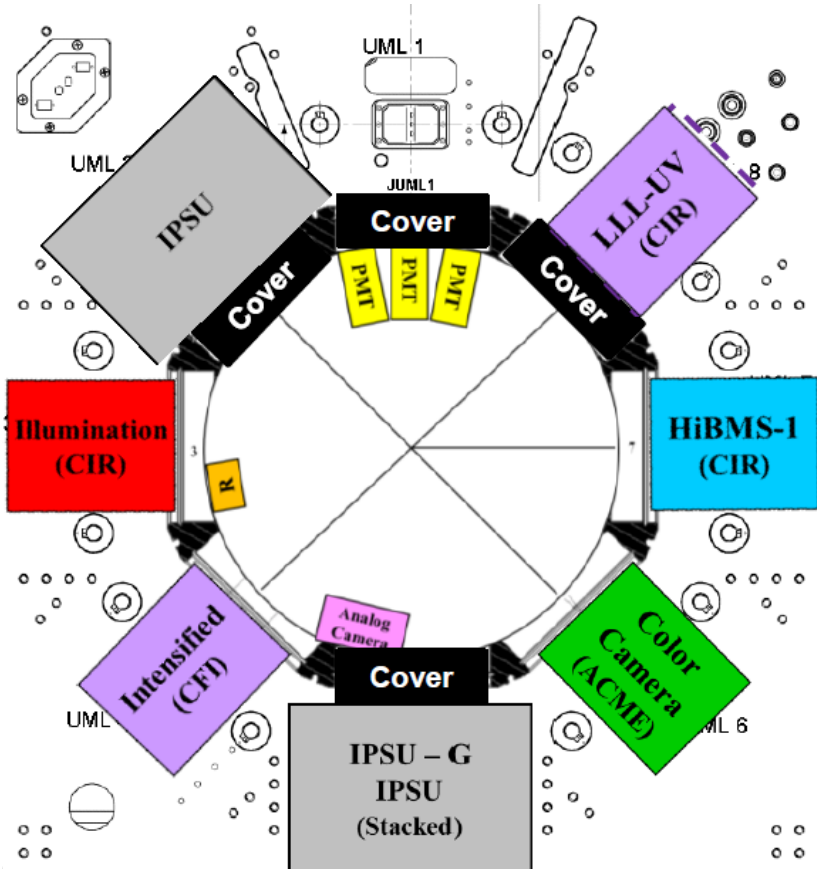

Fig. 2.3. ACME chamber camera configuration

Earth in real time during the experiments. Images from this camera were used for initial flame observations and flame radius measurements. For each flame image, an ellipse is fit at the location where the intensity of the blue color channel is midway between its peak and ambient intensity. The flame diameter is taken as the axis of the ellipse perpendicular to the fuel support tube. The flame is typically quenched in the vicinity of the burner support tube, making it difficult to interpret the location of the flame sheet in that region. Uncertainty in measured flame size is estimated to be ± 4%.

The ACME camera is a high-definition digital color camera with adjustable zoom, focus, and iris settings. This camera was used primarily for pyrometry

measurements, as well as capturing high quality color images of flames. The Cool Flames Investigation Camera (intensified camera) is a monochrome camera with a filter used to detect emissions of formaldehyde. This camera was used to detect cool flames, which were too dim to be seen by other cameras. The High-Bit Depth Multispectral (HiBMs) camera was a monochrome camera that was used in conjunction with a backlight to detect soot formation. Only the operations, ACME, and intensified cameras were used to obtain flame images. Representative images from these three cameras are shown in Fig. 2.4.

Flame temperatures were measured using Thin-Filament Pyrometry (TFP). More detail is provided on TFP in the following sections. Briefly, it is a measurement technique where thin silicon carbide fibers are inserted into the flame where they are heated and visibly glow. The intensity of this glowing is related back to temperature using calibration data. In the ACME chamber an array of 5 fibers is used, spaced 5 mm apart, as shown in Fig. 2.5. These fibers are inserted into the flame after visible soot has dissipated, and the array could either remain stationary or move up and down once in the flame.

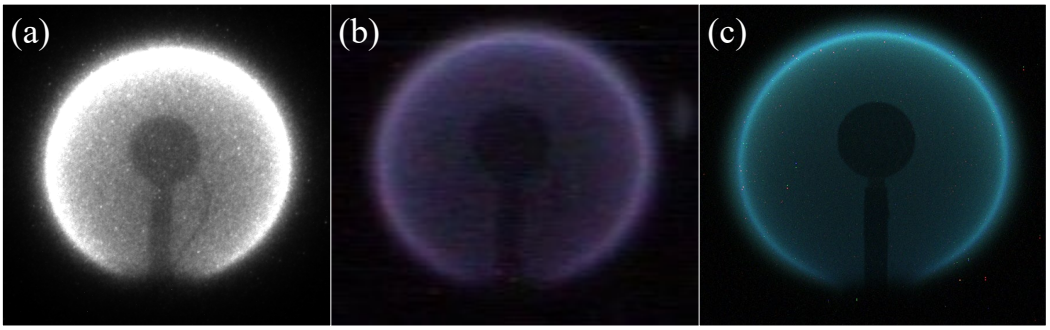

Fig. 2.4. Representative images from the (a) intensified camera, (b) operations camera and (c) ACME camera. Flames are in normal configuration and the fuel is C_2H_4.

Fig. 2.4 shows representative images of a flame ignited aboard the ISS. While the flame appears spherical, it should be noted its center is not coincident with the center of the burner, but rather shifted downwards. The reason for this is not fully understood, but there are two likely factors. The first is the presence of the fuel supply tube at the south pole of the flame. Thermal losses to this tube result in the flame being quenched in the area immediately surrounding it. The flame is noticeably dimmer in its southern hemisphere, and when reviewing videos soot can be seen moving along the circumference of the flame in the direction of the supply tube. This indicates that there is a large temperature gradient along the flame, which could contribute to its displacement.

The other potential reason for the shift in flame location also involves the supply tube. It is possible the connection between the supply tube and the porous sphere is not perfect, resulting in flow leakage out of the bottom of the sphere, pushing the flame downwards. The internal pore geometry of the sphere is also unknown, but there could be imperfections that result in more flow being directed towards the bottom of the sphere, also pushing the flame downwards.

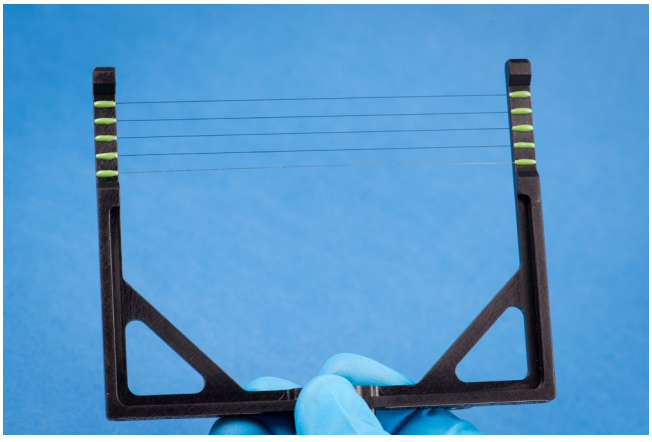

Fig. 2.5. Array of SiC fibers for TFP measurements. The 5 fibers are spaced 5mm apart.

2.3 Camera Characterization and TFP Calibration

TFP measurements were performed using the ACME camera. This camera (model Prosilica GC1380H) has a resolution of 1360 (H) × 1024 (V) pixels. Each pixel is 6.45 × 6.45 μm, for a total sensor size of 8.772 (H) x 6.605 (V) mm. The camera was fitted with a Navitar Zoom 700 lens, with motorized control over zoom, iris, and focus settings. Because the flames varied in size and brightness, a wide variety of camera settings were used over the course of the experiments. In order to accurately perform TFP measurements no matter the settings, an extensive characterization of the camera response was performed. Two filters were available for the ACME camera, a clear fused silica (FS) filter and a BG-7 filter. Calibration was performed with both lenses, but the BG-7 filter had too much reduction in the red signal and was not used.

2.3.1 Camera Characterization

To normalize the intensities for different camera settings, accurate f-numbers are required. F-number is defined as:

$$L_f/d, \tag{2.1}$$

where L_f is focal length and d is aperture diameter. The Navitar lens has a focal length range of 18-108 mm (6x magnification) and a f-number range of f/2.5 to closed. The lens measures zoom and iris as a function of motor counts, rather than in engineering units. With a known range, these counts can be successfully correlated to focal length. The actual aperture diameter range is unknown, but through some measurements and assumptions, the relative aperture diameter as a function of counts can be determined.

ZIN Technologies captured multiple images of an integrating sphere, keeping the focal length constant, and varying the iris. An iris range of 0 counts (wide open) to 75,000 counts (fully closed) was used. Images were recorded in RAW format and converted to TIFF files using ImageJ for analysis. Red, green, and blue pixel intensities are shown in Fig. 2.6, and were determined for each image by taking the mean of a 100x100 pixel region at the center of the image. Intensities are normalized from 0 to 1, where 1 corresponds to a saturated signal.

The iris is assumed to be circular, meaning the intensity varies linearly with iris area. Relative area is the intensity at each iris setting divided by the intensity at a reference point:

$$A = I/I_0, \tag{2.2}$$

where I is the intensity at a given iris setting and I_0 is the intensity at an iris setting of 0 counts. Relative diameter is the square root of the relative area. Plots of relative area and diameter are shown in Fig. 2.7.

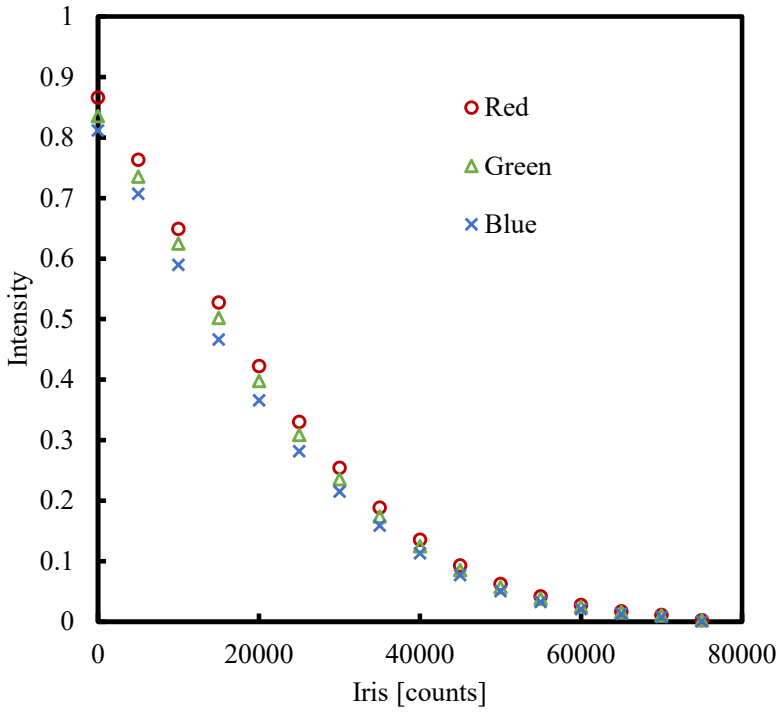

Fig. 2.6. Mean intensity for each iris setting as a function of iris counts.

The result of this is a well-defined relationship between each iris setting and the maximum iris, independent of the physical dimensions of the iris. In Fig. 2.8, relative dimensions are shown as a function of iris counts. A maximum iris diameter can be chosen to calculate diameters at various iris settings.

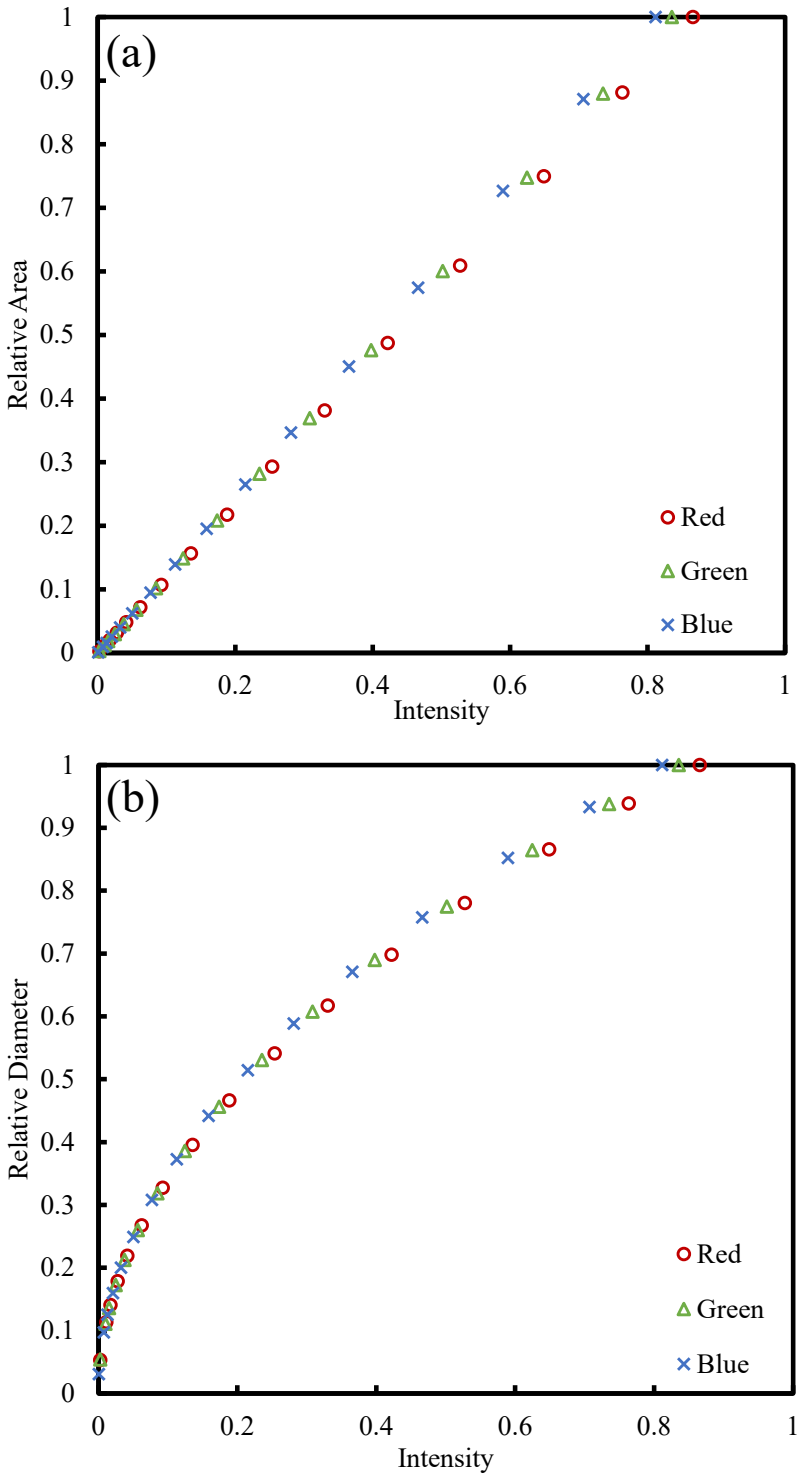

Fig. 2.7. (a) Relative area and (b) relative diameter of the aperture opening as a function of pixel intensity.

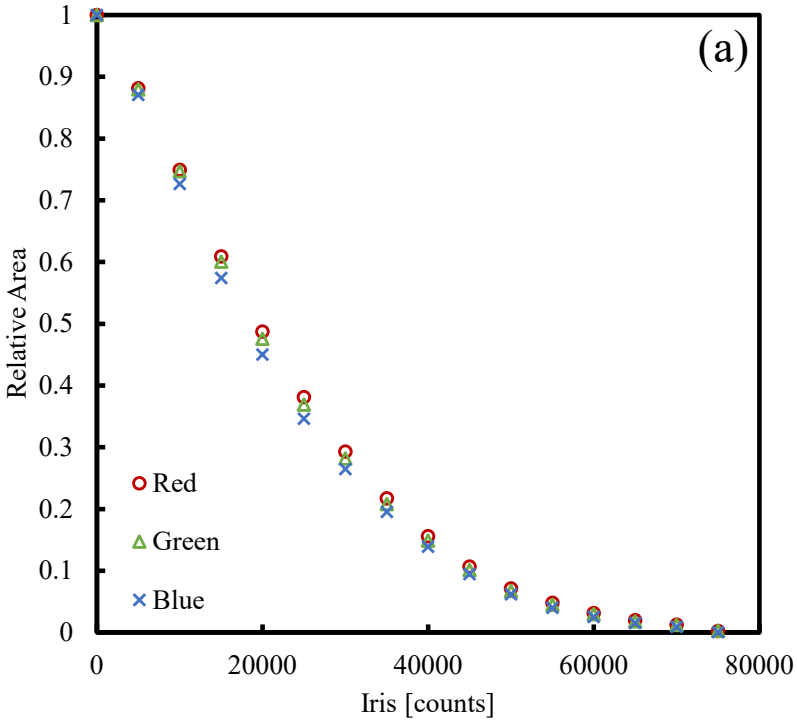

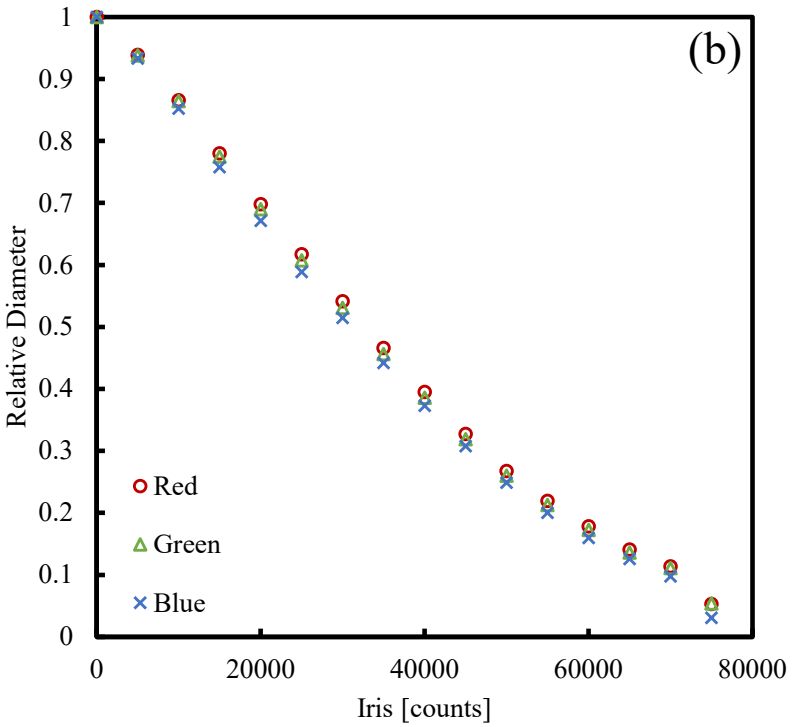

Fig. 2.8. (a) Relative area and (b) relative diameter of the aperture opening as a function of iris counts.

To convert zoom counts to focal length, the assumption is made that a zoom of 0 counts (maximum magnification) corresponds to a focal length of 108 mm, as stated in the lens specifications. The focal length (*f)* is then determined from the equation:

$$f = d_s * WD/FOV, \tag{2.3}$$

where d_s is the sensor dimension, FOV is field of view, and WD is the working distance from the object to the lens, all in units of mm. Since d and WD are constant, the ratio of focal lengths is related to the ratio of FOV:

$$(f/f_0 = FOV_0/FOV) \tag{2.4}$$

With the focal length at 0 counts known, the rest of the focal lengths can be calculated. Diagonal FOV for each zoom setting, and the resulting focal lengths, are shown in Fig. 2.9.

With accurate correlations for focal length and iris diameter, the F-number can be determined for various camera settings. This allows the intensity values to be

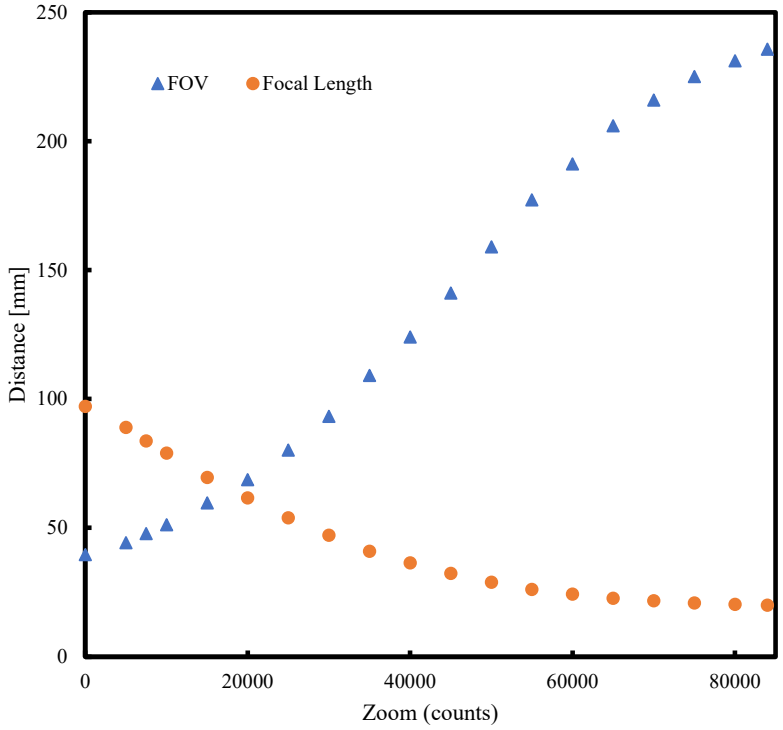

Fig. 2.9. Field of view and focal length as a function of zoom counts.

normalized for different settings, and a single calibration curve to be obtained.

2.3.2 Temperature Calibration

The camera was calibrated using a blackbody source. Blackbody images were captured from 1073 – 1473 K, in 50 K increments. Camera settings were adjusted at each blackbody temperature such that the images were just below saturation. The blackbody images were recorded in RAW format and converted to 16-bit TIFF files using ImageJ, which were demosaiced in MATLAB using an RGGB filter.

For each blackbody image, the mean intensity for the R, G, and B colors is found for a 10 × 10-pixel region at the center of the area of signal. The intensity is normalized to account for different camera settings using:

$$NI = If^2/t, \tag{2.5}$$

where NI is normalized intensity, I is signal intensity of the pixel, f is f-number, and t is exposure time. The camera gain is constant, at its lowest setting, for all TFP and blackbody images and is therefore not included in Eq. (2.5). Owing to the linear response of the camera [40,41], *NI* equals the incident spectral power times a fitting constant, C_3, that accounts for the camera sensitivity and the lens. For the blackbody, this can be expressed as:

$$NI = \frac{\varepsilon_{bb}\, C_1\, C_3}{\lambda^5\, [\exp\left(\frac{C_2}{\lambda T}\right) - 1]}\ , \tag{2.6}$$

where ε_{bb} is the blackbody emissivity (0.99), C_1 and C_2 are the Planck's law constants (3.742×10^8 W-μm^4/m^2 and 1.439×10^4 μm-K), λ is the effective wavelength of the color band under consideration (630 nm for R and 570 nm for G), and T is temperature.

The results of the blackbody calibration are shown in Fig. 2.10. The R pixel intensities are used to obtain the data presented herein because R has the highest signal-to-noise ratio. Nearly identical results are obtained using G. The B pixel intensities are too low to be used. An attempt was made to use two-color ratio TFP pyrometry [40–42], but the color ratio curves obtained from the blackbody calibration for this camera are multi-valued in this temperature range and thus cannot be used.

For TFP aboard the ISS, the exposure time is between 0.05 – 0.4 s, and multiple exposure times are used for each test. The *f*/# is between 2.5 – 10.2, and the diagonal field of view varies between 69 – 80 mm.

The aperture of the blackbody furnace used for the camera calibration is large enough that the signal intensity is spread over many pixels. The SiC fiber diameter,

however, is smaller than the camera resolution, so the camera is intentionally defocused during ISS tests to illuminate enough pixels. To account for the fiber width in the image plane, a fill factor is introduced, defined as the unheated fiber's width in the image from ray tracing divided by the width of a pixel. The fill factors here are between 0.17 and 0.35, depending on the zoom setting.

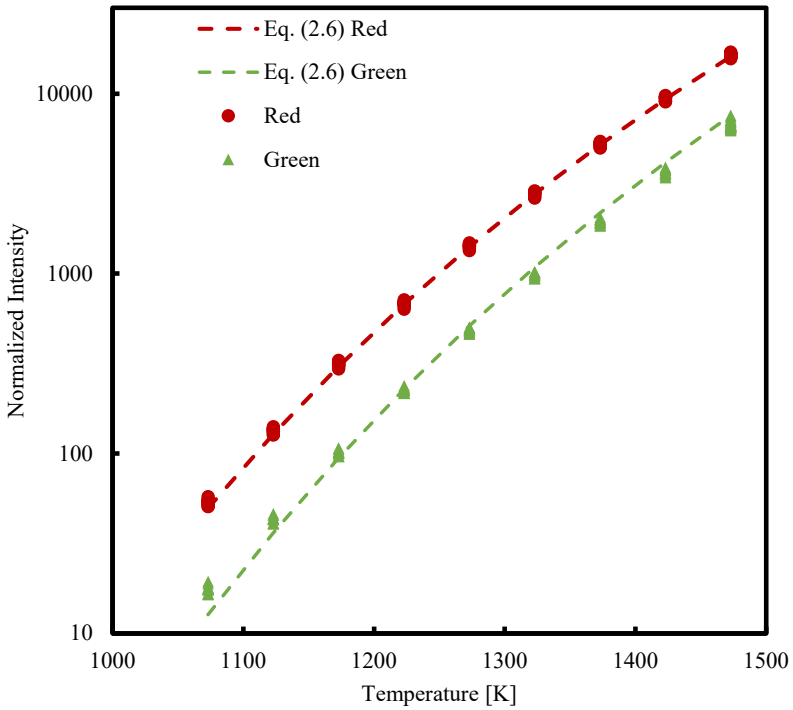

Fig. 2.10. Normalized intensity as a function of temperature. Curves denote the results from Eq. (2.6) and symbols denote blackbody measurements. The fitting constant, C_3, is 23.8 and 34.1 m2-μm/W-s for R and G, respectively.

Fiber images are recorded in HOBJ format and converted to 16-bit color TIFF files using OMA2 [43]. Representative fiber images are shown in Fig. 2.11. Here, the brighter image is saturated and could not be used to obtain a temperature. When multiple fibers were present, the closest fiber to the north pole of the flame that was confirmed to be in the plane of the flame (i.e., had two peaks in intensity) was used. In this case, Fiber 1 was used. For each column of pixels (i.e., perpendicular to the fiber),

pixel intensities from just above and below the fiber's luminescence are identified as the local background. These are averaged and subtracted from the intensity of each pixel in the column. The R pixel intensities for each column are then averaged and each average is divided by the fiber fill factor. This process is repeated for each column that crosses the glowing fiber. This identifies two local TFP maxima, corresponding to the two locations where the fiber crosses the flame. The two maxima are averaged for each image and then converted to NI using Eq. (2.5).

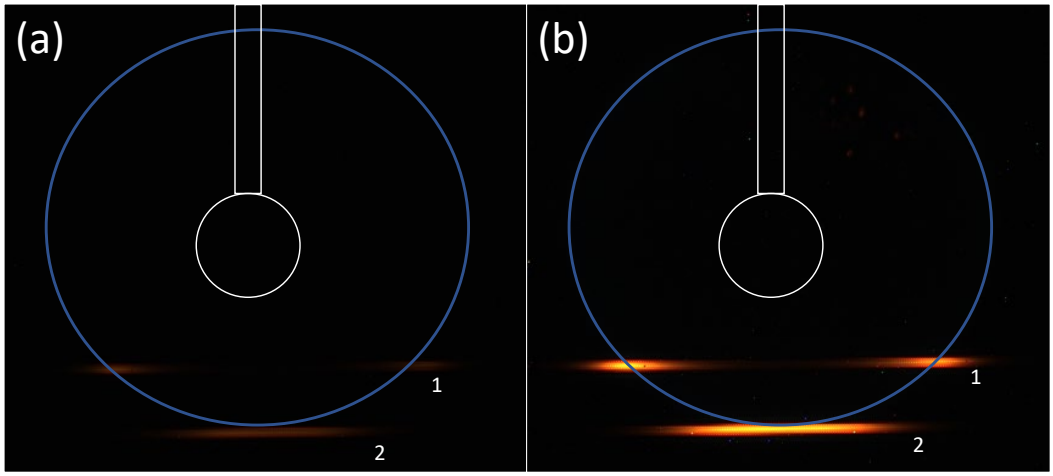

Fig. 2.11. TFP images of the same flame from the ACME camera. *f*/# is 2.5, a focal length is 32 mm, and exposure time is (a) 0.05 s and (b) 0.4 s. Outlines of burner tube, porous, sphere, and flame are shown.

Since the ACME data camera and lens were calibrated, they have been on the ISS for several years and used for many tests. It is believed that both the transmittance of the optical path and the camera sensitivity have been reduced significantly since the calibration was performed. To account for this, the determined NI is divided by a transmissivity factor of 0.36, chosen to approximately match the simulated temperatures from [4]. Quantity NI is converted to fiber temperature using Eq. (2.6), where blackbody emissivity is replaced with fiber emissivity (0.88).

Fiber temperature is corrected to gas temperature by accounting for radiative

losses following [38],

$$T_{gas} - T_s = \frac{\sigma \varepsilon d}{k_{gas}} (T_s^4 - T_\infty^4) \left[0.8237 - 0.5\, ln\left(\frac{ud}{a}\right) \right], \qquad (2.7)$$

where σ is the Stefan–Boltzmann constant, ε is the fiber emissivity (0.88), d is fiber diameter (14 μm), T_s is fiber temperature, T_∞ is ambient temperature (25 °C), and T_{gas}, u, a, and k_{gas} are the local gas temperature, velocity, thermal diffusivity, and thermal conductivity, respectively. This equation is derived from an energy balance on a cylinder assuming laminar flow. In applying Eq. (2.7), α and k_{gas} were those of N_2 at the mean of T_s and T_{gas} and the local gas velocity is obtained from the numerical simulations. The uncertainty of an individual TFP measurement reported here is estimated at ± 100 K, owing to the inability to recalibrate the camera, the radiation correction, and uncertainties associated with testing in space. However, the difference in peak temperature for two times during a given test has an estimated uncertainty of ± 10 K.

Microgravity experiments, particularly on the ISS, are challenging. Once the experimental apparatuses are launched, they generally cannot be altered or repaired, and the effects of space (e.g., cosmic rays) on the diagnostics are unknown. Additionally, diagnostic calibrations must be done on Earth prior to launch, and they cannot be recalibrated. Nonetheless, while it is difficult to acquire quantitative data on the ISS, the available diagnostics do provide valuable semi-quantitative data under conditions unattainable on earth.

2.4 Numerical Model

2.4.1 Model Description

Numerical simulations were performed using the SphDiff program used in Refs. [4,29–35], which is a modification of Sandia PREMIX [44]. The model uses the Chemkin-II package [44]. The governing equations are discretized using finite differencing methods and the model uses a modified Newton method to solve the discretized equations. A detailed description of the model can be found in [4,33].

Radiation heat loss from CO, CO_2, and H_2O is calculated using a detailed absorption/emission statistical narrow band model with wavenumbers ranging from 150 to 9300 cm^{-1}, coupled with a discrete-ordinates method with 20 ordinates [33]. Radiation from soot is not considered in these simulations, as luminous soot does not typically form in the flames considered here after the ignition transient, owing to the large radiative loss fraction from gases and resulting rapid decrease in flame temperature.

The computational domain spans from the burner surface (0.32 cm) to 100 cm. The boundary conditions are described in detail in [33]. Temperature and species concentrations are prescribed at the boundaries, and pressure is held constant. The ambient temperature was 298 K. The size of the domain is sufficiently large that there is no change in species or temperature at the outer boundary.

An adaptive grid algorithm is used, as in [4]. The domain is divided into three zones: an inner zone, a reaction zone, and an outer zone. The inner zone follows the same algorithm as [33]. The center of the reaction zone was identified as the location of maximum temperature. The reaction zone has 200 nodes with 0.001 cm grid spacing.

The grid spacing in the outer zone increases by 5% for each grid cell moving outward. 373 grid points were used, which was found to satisfy grid independence.

The UCSD mechanism with 57 species and 270 reactions is used to simulate the chemical kinetics of the flames [45]. Other chemical kinetics mechanisms were confirmed to provide similar results.

There are certain intricacies of the experimental apparatus that cannot be recreated in the numerical model. The experimental chamber is a constant volume vessel, but the pressure increase for each test was small enough that the constant pressure assumption used in the simulations is sufficient. The disturbances introduced by the presence of the supply tube are also unaccounted for. As previously mentioned, during the experiments the center of the flames tended to drift slightly toward the supply tube, but they maintained their spherical shape. Extinction also tended to occur initially at the supply tube in the experiments, and oscillatory behavior was observed. These disturbances are not recreated in the model as the supply tube is not included, and the flame is assumed to be perfectly centered on the burner. This is expected to have little impact on the results.

The model outputs detailed spatial information including temperature, radiation, heat release rates, reaction rates, species production rates, mole fractions, and mass fractions. Flame radius is defined as the location of peak temperature. Mixture fraction is calculated as

$$Z = \frac{\frac{Y_H - Y_{H,ox}}{nW_H} + \frac{Y_C - Y_{C,ox}}{mW_C} + \frac{Y_{O,ox} - Y_O}{(m+n/4)W_O}}{\frac{Y_{H,fu} - Y_{H,ox}}{nW_H} + \frac{Y_{C,fu} - Y_{C,ox}}{mW_C} + \frac{Y_O - Y_{O,fu}}{(m+n/4)W_O}}, \qquad (2.8)$$

where Y_i, and W_i represent the mass fraction and molecular weight of species i,

respectively. The fuel stream boundary is indicated by the subscript *fu,* and the oxidizer stream boundary is indicated by the subscript *ox*. Subscripts *m* and *n* represent the number of carbon and hydrogen atoms, respectively, in the fuel C_mH_n. Thus, $Z = 0$ is the oxidizer boundary and $Z = 1$ is the fuel boundary [46].

2.4.2 Inner Boundary

Of particular interest here is the inner boundary for the simulations, namely the burner surface. Here the boundary condition for the energy equation is the burner temperature, which can either be prescribed or calculated. For cases that are run based on experimental results, the experimentally measured burner temperature is typically used as a model input. Ideally, however, the model would require no experimental input and be able to accurately capture the behavior of the burner. When cases are run that have no experimental data, the burner temperature is typically held constant at the ambient temperature of 298 K. It is important to know the effect of the temperature at the inner boundary on the overall flame properties so accurate conclusions can be drawn from the simulations.

It is possible to calculate the temperature change of the burner using the lumped capacitance method and considering the heat gained by conduction from the flame and incident radiation and lost due to emitted radiation and heating of the fuel gas. A control-volume analysis yields

$$\frac{dE_b}{dt} = \frac{k_g A_b (T_{g,b+1} - T_b)}{(r_{b+1} - r_b)} - \dot{m} c_{p,g} (T_{g,b} - T_{g,i}) + Q_{rad,b}\,, \qquad (2.9)$$

where E_b is the burner internal energy. The first term on the right-hand side is the rate of heat conduction to the burner from the gas, where k_g is the thermal conductivity of the gas, A_b is the burner surface area, T is temperature, and r is radius. Subscript g denotes gas, subscript b denotes burner radius, and subscript $b+1$ denotes the radius of the grid cell next to the burner. The second term on the right-hand side is the heating of the reactant gases from burner inlet temperature to the burner surface temperature, where $\dot{m}$ is mass flow rate and $c_{p,gas}$ is the gas specific heat. Subscript i denotes the temperature of the gas as it exits the supply tube and enters the porous sphere. The third term on the right-hand side is the net incident radiation at the burner surface (Q_{rad}), including radiation from the burner and radiation from the hot gases. A burner emissivity of 0.6 is assumed. Gas properties are found using composition and temperature of the gas at the burner surface.

The most uncertain term in Eq. (2.9) is the gas heating term. The temperatures $T_{g,b}$ and $T_{g,i}$ are not measured experimentally. The reactant gas enters the system at 298 K, but there is possibly some heating as the gas flows through the supply tube. It is also unclear how much heating occurs as the gas passes through the porous sphere itself. The base assumption in the numerical model is that the fuel gas exits the supply tube at 298 K and is heated to the burner surface temperature as it passes through the burner. If this were not the case, the convection term in Eq. (2.9) would be completely neglected.

Once the burner energy change has been determined, its temperature change is calculated from

$$\frac{dE_{burner}}{dt} = \rho_b V_b \phi_b c_{p,b} \frac{\mathrm{d}T_\mathrm{b}}{\mathrm{d}t}, \quad (2.10)$$

where ρ_b is burner density, V_b is burner volume, ϕ is burner porosity, and $c_{p,b}$ is burner specific heat. The heat capacity of the burner material is 500 J/kg K. The burner density is 4.6 kg/m^3, and its porosity was not measured but is assumed to be 79%.

2.5 Results

2.5.1 Model Validation

The numerical model used here has been used extensively in past microgravity spherical diffusion flame work, and consistently captures experimental behavior accurately [4–6,11,30–32]. Due to the diffusion-controlled nature of these flames, flame radius is a good indicator of model behavior. If flame radius is predicted accurately, then transport properties can be considered valid. Transport properties are dependent on temperature, which is dependent on radiation levels and chemical kinetics. The experimental conditions for 17 flames are shown in Table 2.1. All these flames extinguished radiatively, and TFP measurements were taken. The predicted vs. measured flame radius just before radiative extinction is shown in Fig. 2.12. There is good agreement between the model and experiments, with an R^2 value of 0.98.

Table 2.1. Experimental conditions for 17 normal flames that radiatively extinguished aboard the ISS.

Flame	X_{O2}	X_{C2H4}	$\dot{m}_{total}$ [mg/s]	T_{ad} [K]	Z_{st}	P [atm]
A	0.202	1.000	2.53	2366	0.064	1.0
B	0.206	0.476	2.76	2296	0.125	1.0
C	0.201	1.000	2.53	2366	0.064	1.0
D	0.205	0.476	2.76	2296	0.125	1.0
E	0.206	0.476	2.76	2296	0.125	1.0
F	0.208	1.000	1.64	2366	0.064	1.0
G	0.208	1.000	1.64	2366	0.064	1.0
H	0.204	0.288	2.28	2209	0.191	1.0
I	0.207	0.288	4.57	2209	0.191	1.0
J	0.209	1.000	1.64	2366	0.064	1.0
K	0.203	0.288	2.06	2209	0.191	1.0
L	0.285	0.132	4.51	2219	0.422	1.0
M	0.379	1.000	2.53	2818	0.112	1.0
N	0.376	1.000	2.53	2818	0.112	1.0
O	0.372	1.000	2.53	2818	0.112	1.0
P	0.205	1.000	0.66	2366	0.064	1.0
Q	0.351	0.168	4.88	2324	0.363	1.0

Predicted and measured extinction temperatures for the 17 flames are shown in Fig. 2.13. The means are similar, at 1130 ± 23 K for the experiments and 1126 ± 6 K for the simulations, which is consistent with [4,5,30,32]. The larger deviation in experimental values is likely due to the uncertainties in the TFP calibration.

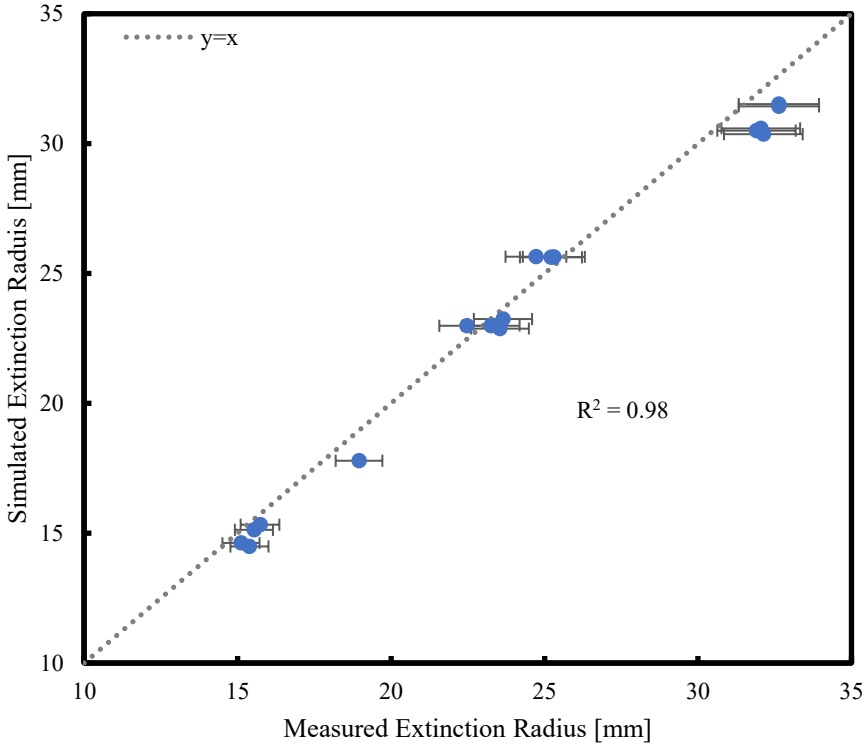

Fig. 2.13. Simulated vs. measured extinction radius for 17 normal flames ignited on the ISS.

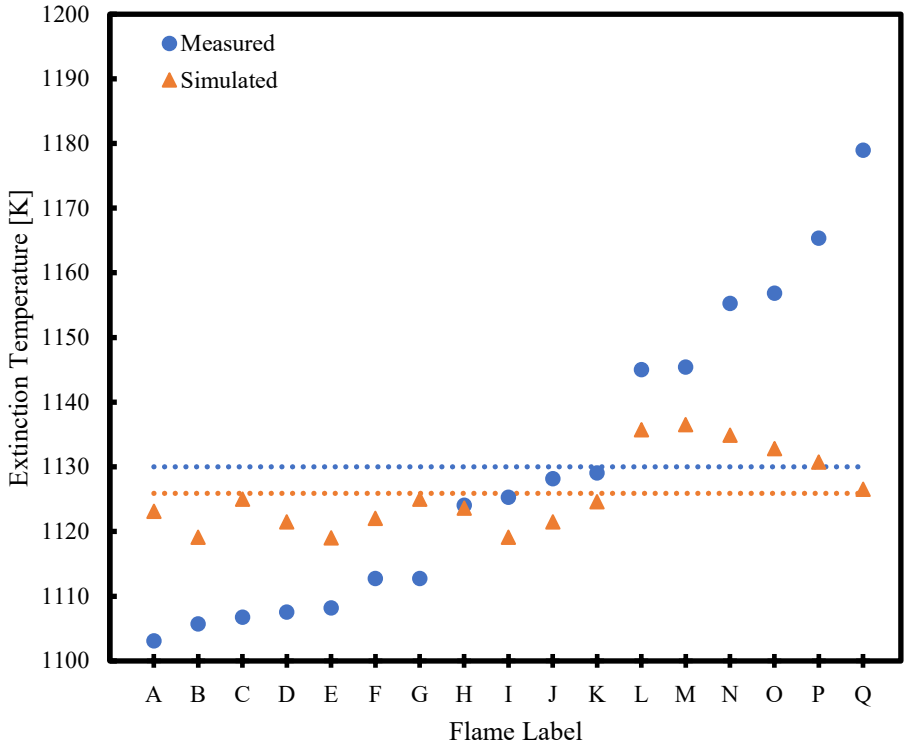

Fig. 2.12. Simulated vs. measured extinction temperature for 19 normal flames ignited on the ISS.

2.5.2 Burner Temperature Measurements

Table 2.2 shows the conditions for the flames considered. These flames were chosen for their broad range of mass flow rate values, and all of them extinguished radiatively.

The measured and simulated burner temperatures are presented in Fig. 2.14 for the normal flames, and Fig. 2.15 for the inverse flames. Fig. 2.14a shows the simulated temperatures with gas heating for the normal flames, and Fig. 2.15a shows the same data for the inverse flames. For low flow rates, the temperature in the case where reactant gas heating is included is representative of the experimental values. As the flow rate increases, the model underpredicts the burner temperature due to the large increase in the gas heating term. This is especially apparent in Flames C, D, G, and H.

Table 2.2. Experimental conditions for studying burner temperature. Both normal and inverse flames are considered.

Flame	Type	X_{O2}	X_{C2H4}	$\dot{m}_{total}$ [mg/s]	T_{ad} *[K]*	Z_{st}	P *[atm]*
A	Normal	0.205	1.000	0.64	2346	0.062	1.02
B	Normal	0.203	0.291	1.98	2179	0.184	1.01
C	Normal	0.376	1.000	2.52	2785	0.106	1.01
D	Normal	0.374	0.502	5.02	2733	0.191	1.31
E	Inverse	0.850	0.096	2.78	2450	0.726	1.02
F	Inverse	0.850	0.201	5.90	2818	0.557	1.01
G	Inverse	0.262	0.274	8.80	2368	0.232	1.01
H	Inverse	0.345	0.275	11.31	2546	0.286	1.01

Fig. 2.14b shows the calculated temperatures when gas heating is neglected for the normal flames, and Fig. 2.15b shows the same data for the inverse flames. Neglecting gas heating causes the burner temperatures to increase, resulting in calculated temperatures rising to levels much more consistent with the experimental

results. This difference is much more profound for flames of high mass flow rates (C, D, G, and H). For the inverse flames this effect is more profound. These results indicate that the fuel gas is not heated by the porous sphere as it passes through it at high flow rates but may be heated at low flow rates.

If the gas travels through the porous sphere without drawing a significant amount of heat from it, there are two possibilities. The first is that the gas exits the burner at the ambient temperature of 298K. If this were the case, it is expected that the modeled flame temperatures would decrease since the flame would lose additional heat towards heating the fuel gas. This effect should be more noticeable in flames with a higher flow

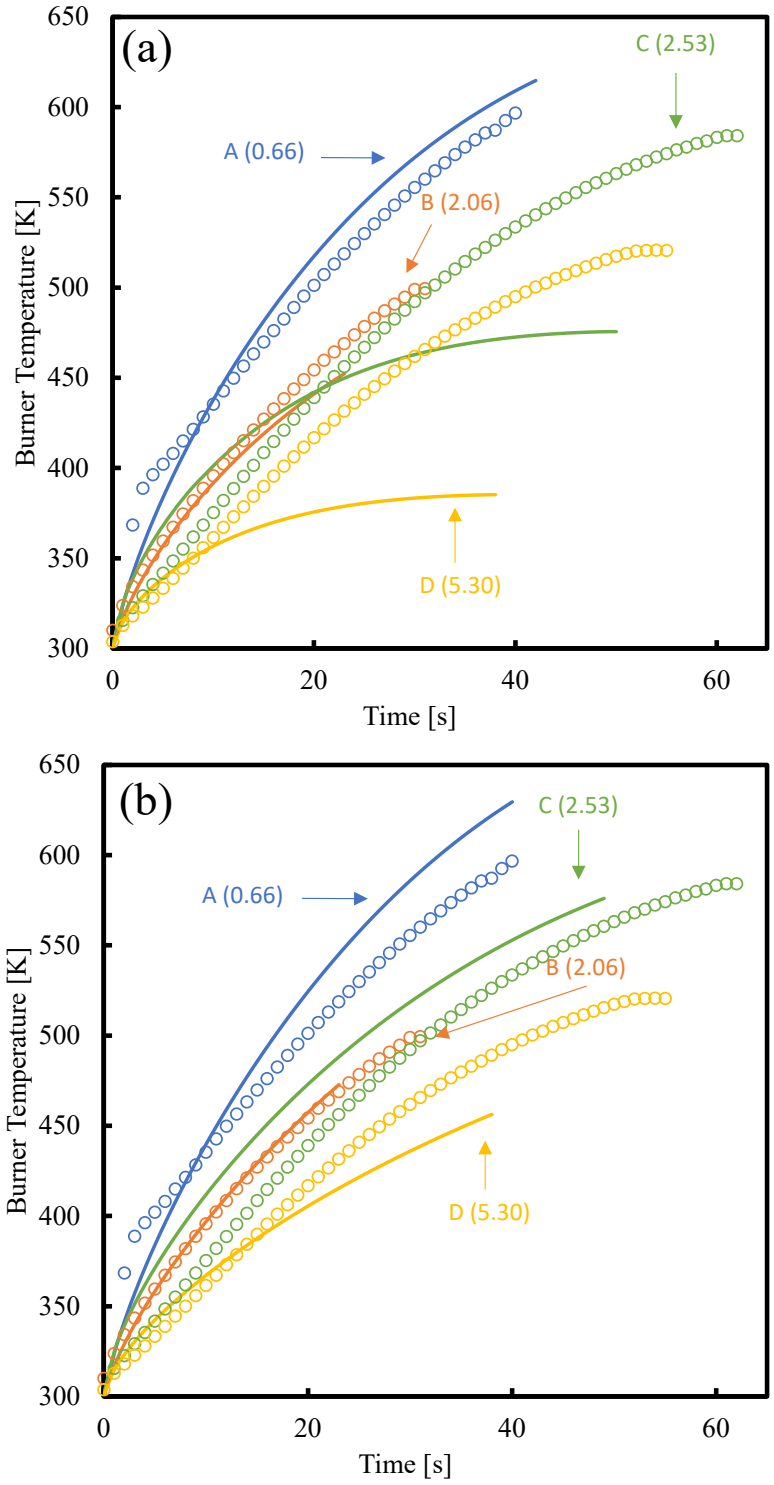

Fig. 2.14. Normal flame burner temperature as a function of time. Lines represent numerical predictions and open circles represent numerical predictions both (a) with gas heating and (b) without gas heating.

rate, meaning current predicted temperatures of those flames should be higher than

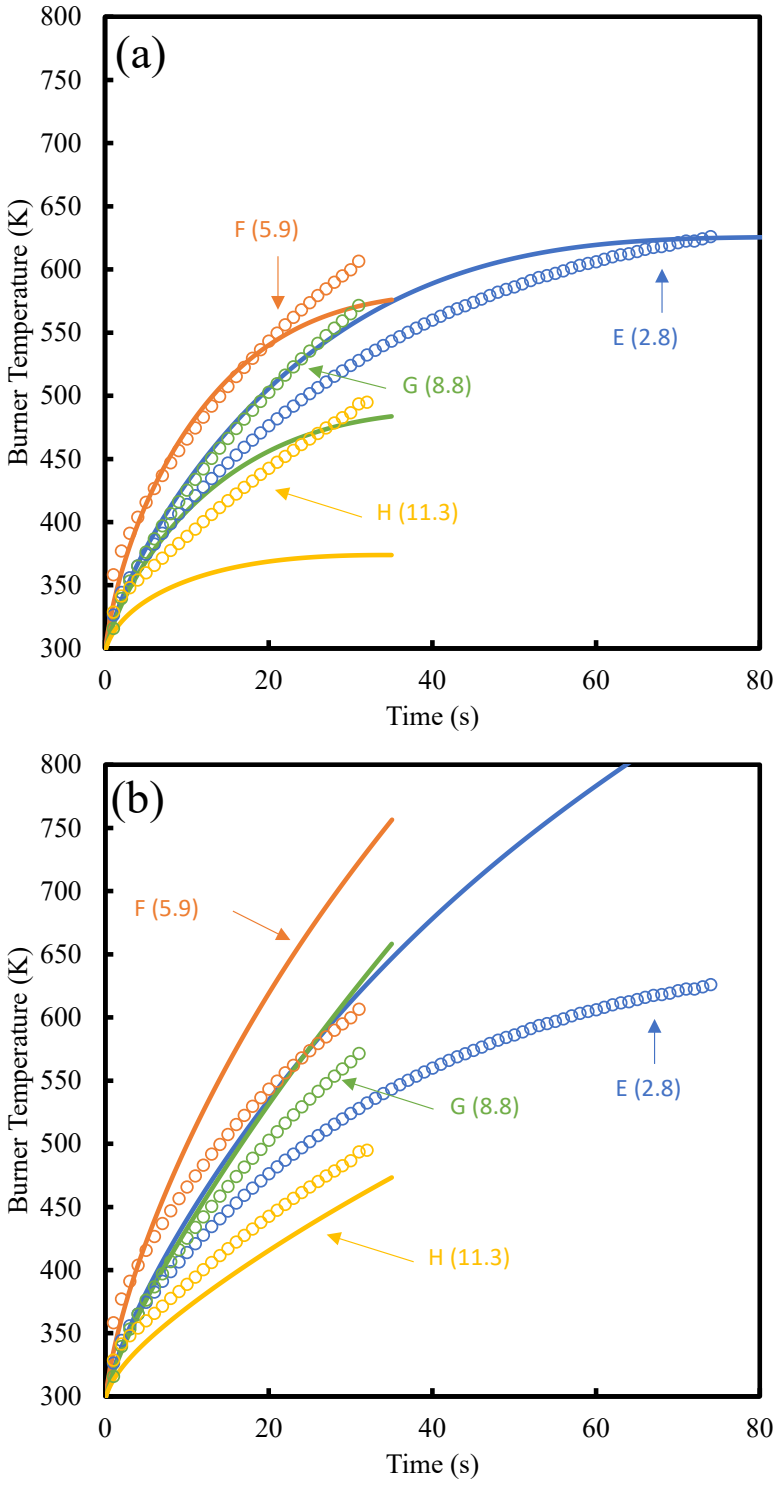

Fig. 2.15. Inverse flame burner temperature as a function of time. Lines represent numerical predictions and open circles represent numerical predictions both (a) with gas heating and (b) without gas heating.

experimental values. The other possibility is that the gas is heated as it passes through

the supply tube, and/or heated directly by the hot gases at the burner surface. In this scenario the modeled flame temperatures should remain the same, since the gas is still exiting the burner at the experimentally measured burner temperature.

2.5.3 Flame Temperature Measurements

Fig. 2.16 shows the numerically predicted flame temperatures for the normal flames when the experimental burner temperature is prescribed, indicated by solid lines, and when the burner temperature is held constant, indicated by dashed lines, alongside the radiation corrected fiber temperatures, indicated by open circles. The experimental temperatures tend to rise farther above the model temperatures as the flow rate increases. Temperature difference as the flame nears extinction increases from ~6 K for Flame A to ~60 K for Flame D. This implies that the prediction of flame temperature is not impacted by flow rate, or else the opposite effect would be observed. At high flow rates the flame temperature is underpredicted by the model rather than overpredicted. The assumption that the gas temperature at the burner surface is equal to the burner temperature does not seem to have a large effect on the system at large.

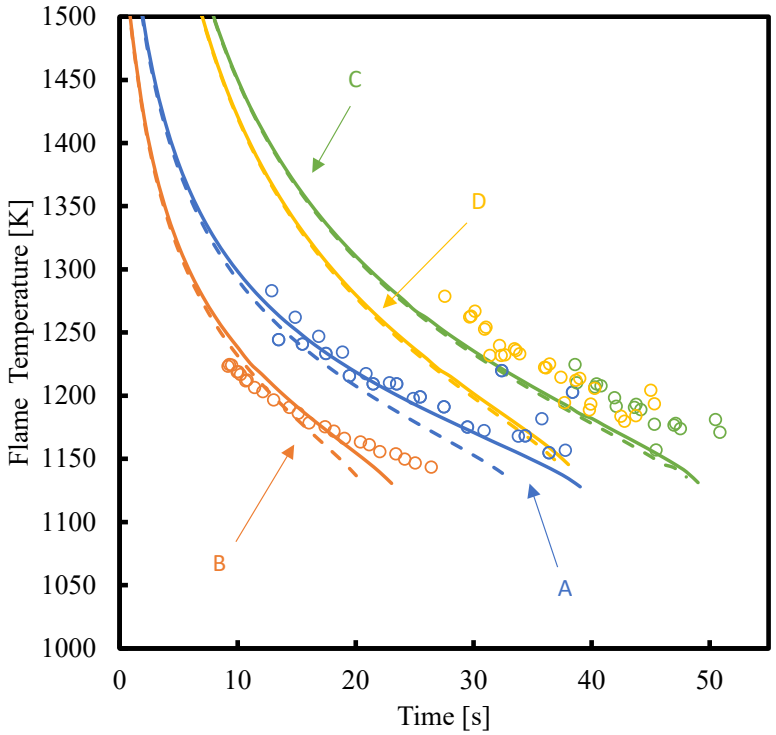

Fig. 2.16. Flame temperature vs. time for the normal flames. Radiation corrected gas temperatures are represented by open circles, numerically predicted gas temperatures with the experimental burner temperature prescribed are represented by solid lines, and numerically predicted gas temperatures with the burner temperature held constant at 300 K are represented by dashed lines.

2.5.4 Flame Radius Measurements

When the burner temperature is held constant at 298 K, more heat is lost to the burner, which should result in a decrease in flame temperature and increase in flame radius. Numerically predicted flame radius is shown in Fig. 2.17 for the normal flames. Both the cases where the experimental burner temperature was used and the cases where the burner temperature was held constant are shown. The effect of holding burner temperature constant at 298 K is most prominent in Flames A and B. These smaller flames exhibit a much larger contribution from the conduction term owing to their smaller radii. As flame radius increases, burner temperature becomes increasingly

decoupled from flame temperature. At 30 s, the case with constant burner temperature is 18 K lower than the case with experimental burner temperature for Flame A. Meanwhile, Flame D only exhibits a difference of 3 K between the two cases.

For Flames A and B, the radius is higher when the burner temperature is held constant. For Flames C and D, the radius is either the same or lower for the constant burner temperature case. 30 s into Flame A, the flame temperature for the constant burner temperature case is lower than the experimental case by 1.5%, and the radius is higher by 0.9%. By contrast, 30 s into Flame D the constant burner temperature case is cooler by 0.3%, and smaller by 0.2%.

It is apparent that burner temperature does not have a significant effect on the larger aspects of the system in most cases. For low flow rates the assumption that the

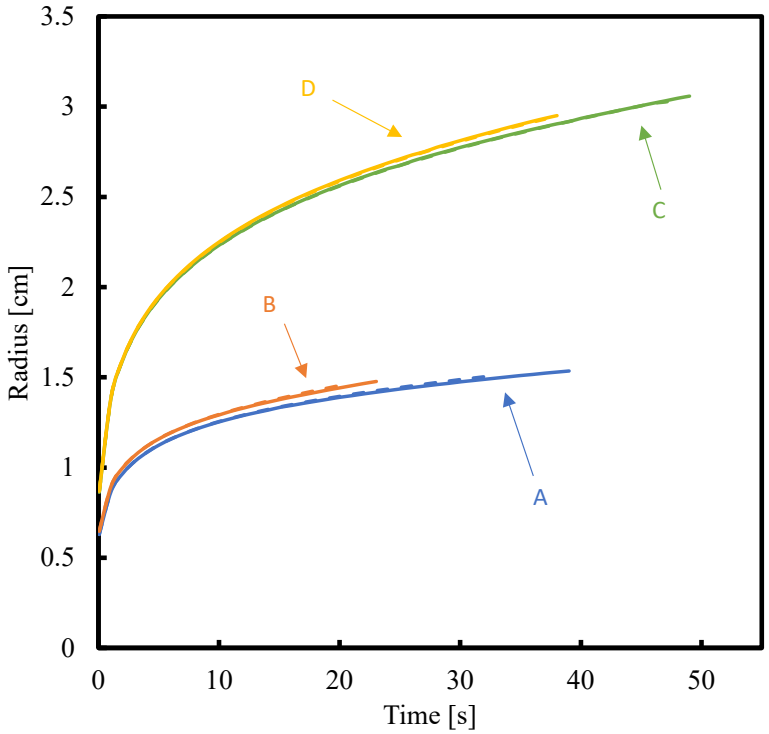

Fig. 2.17. Numerically predicted flame radius vs. time for the normal flames. Solid lines were calculated with the experimental burner temperature and dashed lines were calculated with the burner temperature held constant at 300 K.

gas temperature is equal to the burner temperature at the burner surface is more accurate, and thus the model accurately captures the behavior of the system. For high flow rates this assumption is inaccurate, but the overall flame properties are still modeled accurately. This indicates that there is some other method for heating the gas entering the system, be it heating from the supply tube, direct gas heating, or something else, that results in the gas exiting the burner at a temperature close to the measured burner temperature.

2.6 Summary

An overview of the experimental apparatus used for conducting microgravity burner-supported spherical diffusion flame experiments on the ISS was presented. The TFP method for measuring flame temperature was explained. An overview of the transient numerical model used to simulate the flame was presented. Flame temperature measurements made using TFP were shown to agree with the trends predicted by the numerical model. Experimentally measured extinction radii were shown to agree exceptionally well with the numerical predictions.

The effect of gas flow rate on burner temperature was examined. The numerical model was shown to be able to predict experimentally measured burner temperature with the assumption that the heating of the fuel gas was ignored. This assumption is not necessary for low flow rates but becomes more important as the flow rate increases. If the fuel gas is not heated by the porous sphere itself, it must be heated by the flame or in the supply tube. Flame temperature measurements and predictions indicated the gas does indeed leave the burner at a temperature close to the burner temperature.

The effect of holding burner temperature constant at 298 K on flame temperature

and radius was shown. Burner temperature was shown to have a noticeable effect on the flame temperature and smaller effect on flame radius for small flames, and a smaller effect on temperature and radius for large flames. These results indicate that the temperature of the porous sphere has little effect on the overall flame properties, except in cases where the flame is small and close to the burner.

Chapter 3 Spherical Flame Kinetics at Atmospheric Pressure

3.1 Introduction

Ethylene (C_2H_4) is an important intermediate in the oxidation of higher order hydrocarbons. A better understanding of its oxidation is imperative to designing accurate engine models over a wide range of temperatures. With the emergence of low temperature advanced engine technologies, a better understanding of C_2H_4 oxidation pathways at low temperatures is paramount. Microgravity provides a unique opportunity to study the combustion of C_2H_4 over a wide range of temperatures for otherwise matched conditions. Microgravity spherical diffusion flames ignite at high temperatures, after which the temperature decreases due to radiative losses. When the flame reaches a critical temperature, found in multiple studies to be 1130 K for C_2H_4 at atmospheric pressure [4,5,29,32], it extinguishes radiatively.

The combustion pathway of C_2H_4 is well understood for counterflow diffusion flames with a peak temperature above 1500 K [46,47]. C_2H_4 mainly reacts with H, with lesser reaction contributions from OH and O due to their low concentrations in the fuel region. These radicals, H, OH, O, and, to a lesser extent, HO_2, form the main radical pool that contributes to product formation. Much of the heat release comes from the oxidation of acetylene (C_2H_2) and the formation of formaldehyde (CH_2O), with the formation of CO_2 and H_2O from CO and H_2 via OH also having significant contributions [46,47].

In microgravity, long residence times and low strain rates could change the high temperature oxidation mechanism of C_2H_4. As the peak temperature decreases with time and the flame approaches extinction, new pathways may emerge that further alter the chemistry. Long residence times are also known to promote the formation of warm flames (800 – 1100 K) and cool flames (below 800 K) [13]. This work aims to examine the changing kinetics that lead to radiative extinction, and the role of warm flame chemistry.

3.2 Methods

The numerical model employed here is the same as in previous chapters, and details can be found in Chapter 2. For the simulations performed here the inner boundary was maintained at the ambient temperature of 298 K. The UCSD mechanism was employed again here.

3.3 Results and Discussion

3.3.1 Flame Conditions

The flame conditions are summarized in Table 2.2. These conditions are similar, but not identical, to tests performed on the ISS. They were chosen to match the adiabatic

Table 3.1. Numerical simulation conditions

X_{fuel}	X_{O2}	$\dot{m}_{fuel}$ [mg/s]	Z_{st}	T_{ad} [K]	p [atm]
0.159	0.333	1.5	0.4	2366	1

flame temperature of a fuel-air flame, while increasing the stoichiometric mixture fraction (Z_{st}). Simulations performed at other Z_{st} values produced similar results.

3.3.2 Temporal Evolution

The temporal evolutions of peak temperature, flame radius, and radiative loss fraction (Q_R/Q_C) are shown in Fig. 3.1. The flame ignites with a peak temperature close to the adiabatic flame temperature. As the flame grows, radiative heat losses increase relative to the amount of heat release, dropping the flame temperature until the flame extinguishes.

To examine the effect of temperature change on the flame, it is useful to look at the flame properties at two separate times. The first time is just after ignition, when the peak temperature is 2000 K (high temperature), and the second is just before extinction, when the peak temperature is 1130 K (low temperature). Fig. 3.2a shows spatial profiles of temperature, fuel mole fraction, and oxidizer mole fraction at these two peak temperatures. The temperature profile is much broader at low temperatures, and there is appreciable leakage of fuel and oxidizer across the region of peak temperature. Increased oxidizer levels on the fuel side lead to new chemical pathways at low temperatures.

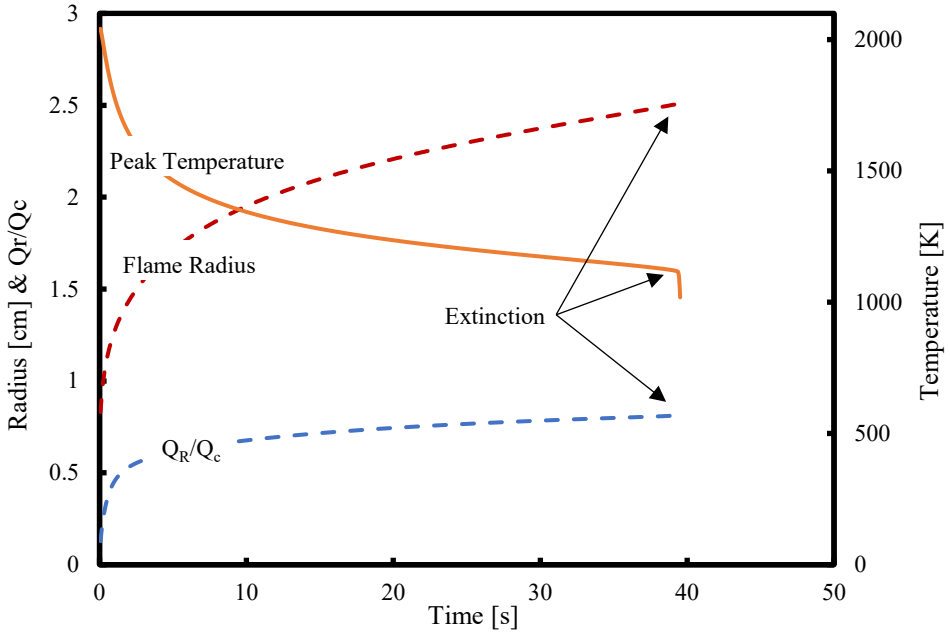

Fig. 3.1. Temporal evolution of peak temperature, flame radius, and radiative loss fraction.

Fig. 3.2b shows a comparison of temperature, fuel mole fraction, and oxidizer mole fraction at high and low temperature, but in terms of mixture fraction (Z) rather than physical space. The following plots in this chapter will be in terms of Z, corresponding plots in physical space can be found in Appendix B. The location of Z_{st} is slightly on the fuel side of peak temperature for both conditions, and at low temperature the discrepancy between the two locations increases, due to reduced fuel consumption and increased oxidizer levels on the fuel side. The temperature gradients are also steeper when the peak temperature is higher.

3.3.3 Species Profiles

Fig. 3.3 shows spatial mole fraction profiles of the other major species in the system, CO_2, H_2O, CO, H_2, C_2H_2, and CH_2O. Products CO_2 and H_2O are present at elevated levels throughout the region of interest for both temperatures. The mole fractions of CO and H_2 have decreased with temperature, but still show an appreciable

concentration. The main difference in major species profiles at high and low temperature comes from C_2H_2 and CH_2O. C_2H_2 is an important species at high temperature, but at low temperature its concentration has decreased dramatically. CH_2O experiences the opposite trend, with low concentrations at high temperature and significantly increased concentrations at low temperature. This is a consequence of the shifting chemistry.

Fig. 3.4 shows spatial mole fraction profiles of the main radical species in the system, H, OH, O, and HO_2. The first three have similar profiles at both temperatures, but occur over a narrower range of *Z*. Their magnitudes have greatly decreased at low

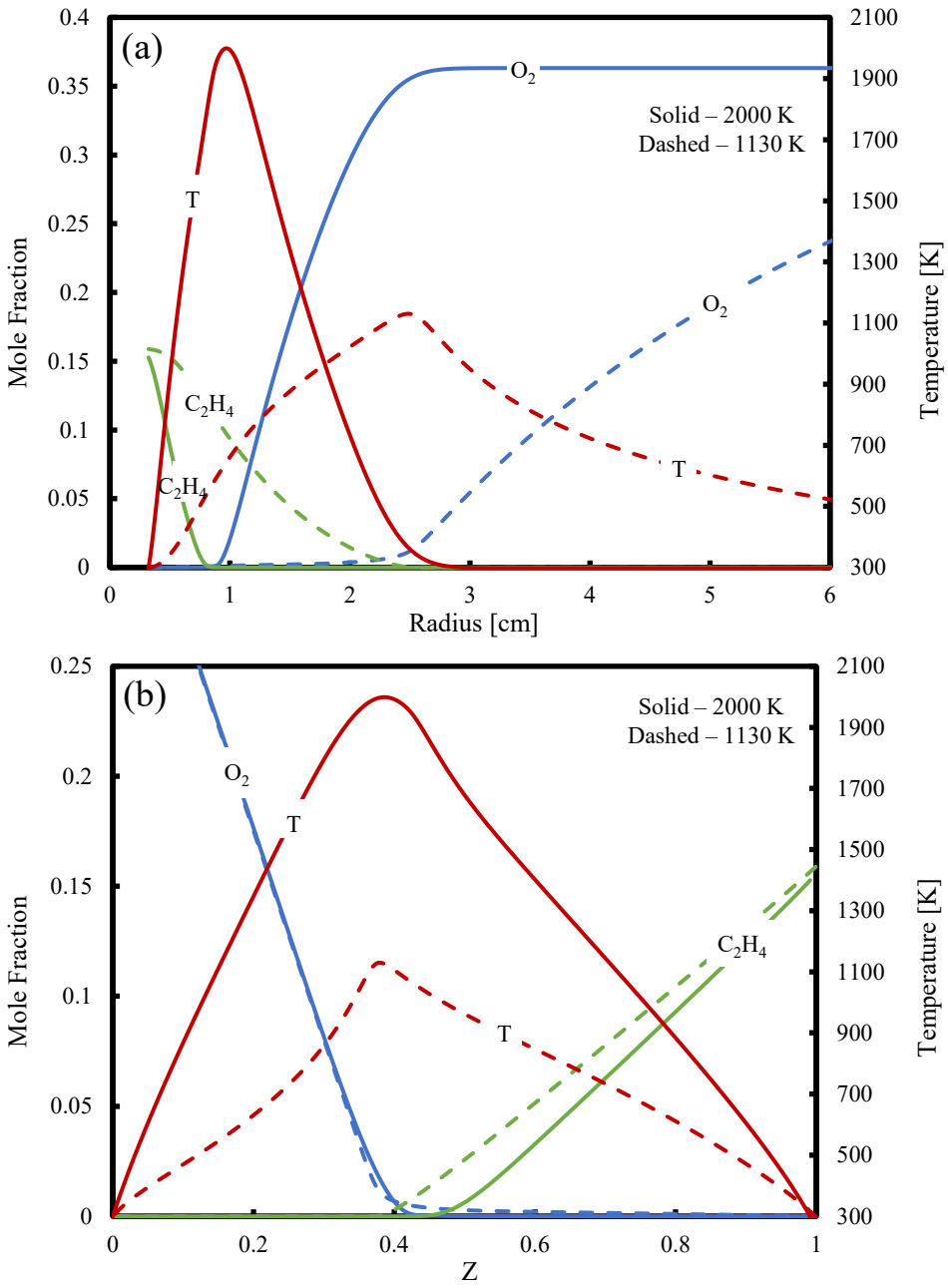

Fig. 3.2. Spatial profiles of peak temperature and fuel and oxidizer mole fraction in (a) physical space and (b) mixture fraction space.

temperature. Increased reactant leakage facilitates the appearance of new reaction pathways leading to the elevation of HO_2 radical levels throughout the flame region, and especially on the fuel side. The replacement of H by HO_2 as the most prevalent radical on the fuel side leads to an increase in oxidative chemistry at low temperature.

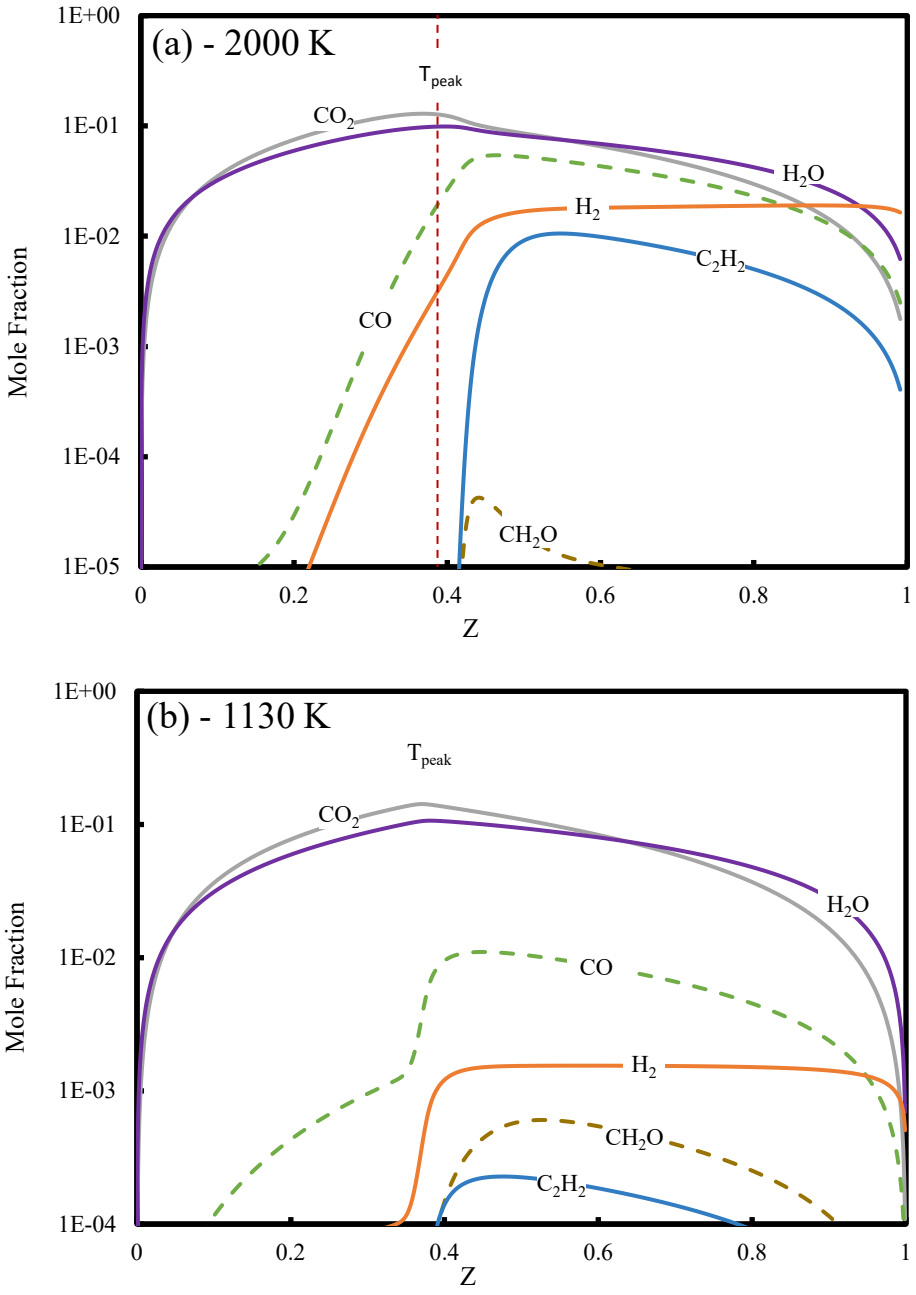

Fig. 3.3. Spatial profiles of CO_2, H_2O, CO, H_2, CH_2O, and C_2H_2 mole fractions at (a) 2000 K and (b) 1130 K.

3.3.4 Reaction Rates

Spatial profiles of net reaction rate and temperature in the flame region for peak temperatures of 2000 and 1130 K are shown in Fig. 3.5. A list of relevant reactions and their corresponding numbers from the UCSD mechanism can be found in Table 3.2. To

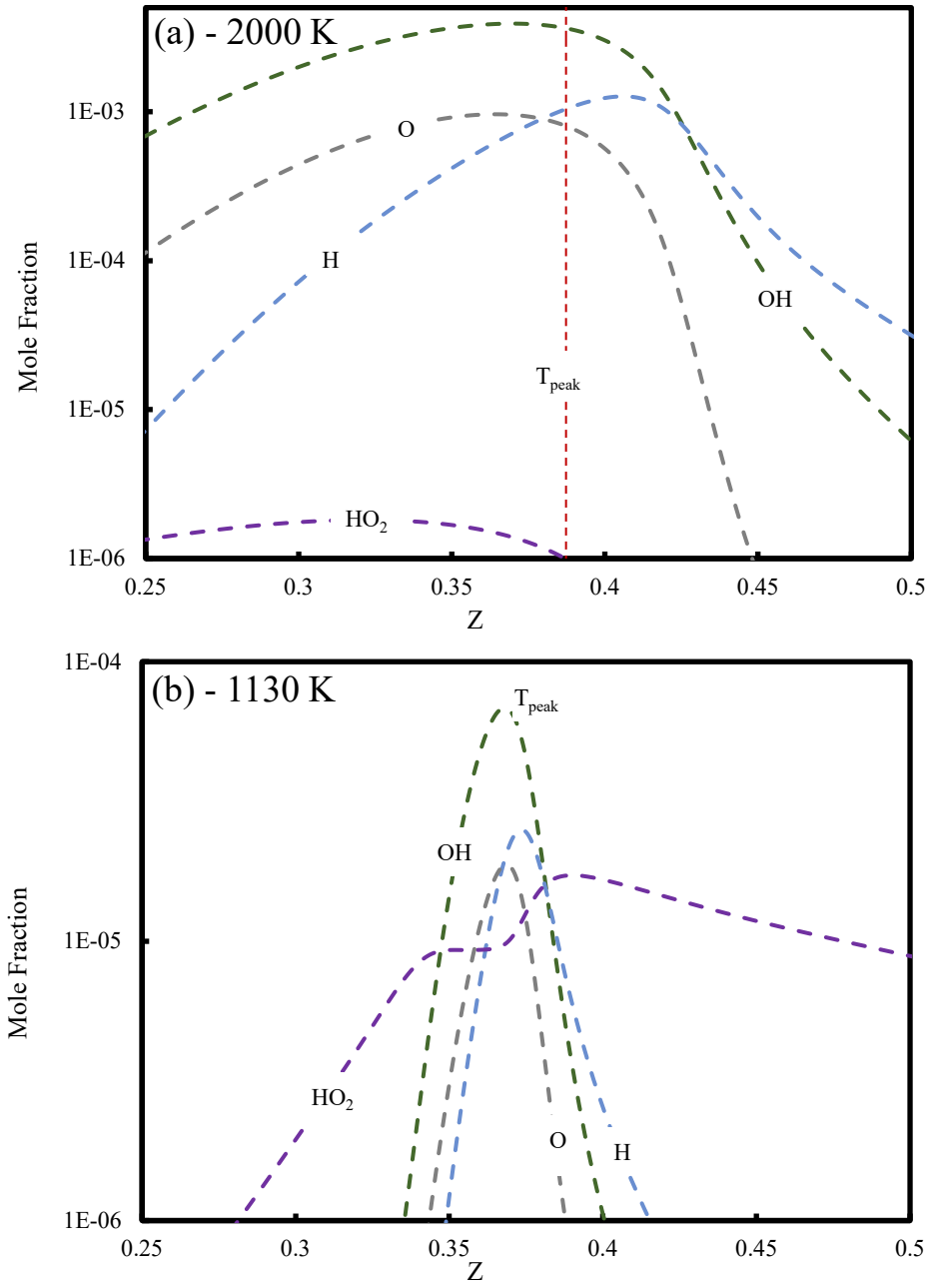

Fig. 3.4. Spatial profiles of O, OH, H, and HO_2 mole fractions at (a) 2000 K and (b) 1130 K.

improve clarity, the spatial profile is only shown for a subset of the listed reactions. Net reaction rate is defined as the difference between the forward and reverse reaction rates for each reaction. The rate of most reactions drops off with temperature, although there are some exceptions.

At high temperature there are two easily distinguishable zones in the flame: a pyrolysis zone where C_2H_4 is converted to C_2H_2 and an oxidation zone consisting of radical cycles and the formation of products. Both zones occur primarily on the fuel side. At low temperatures these two zones overlap and are not as easy to distinguish.

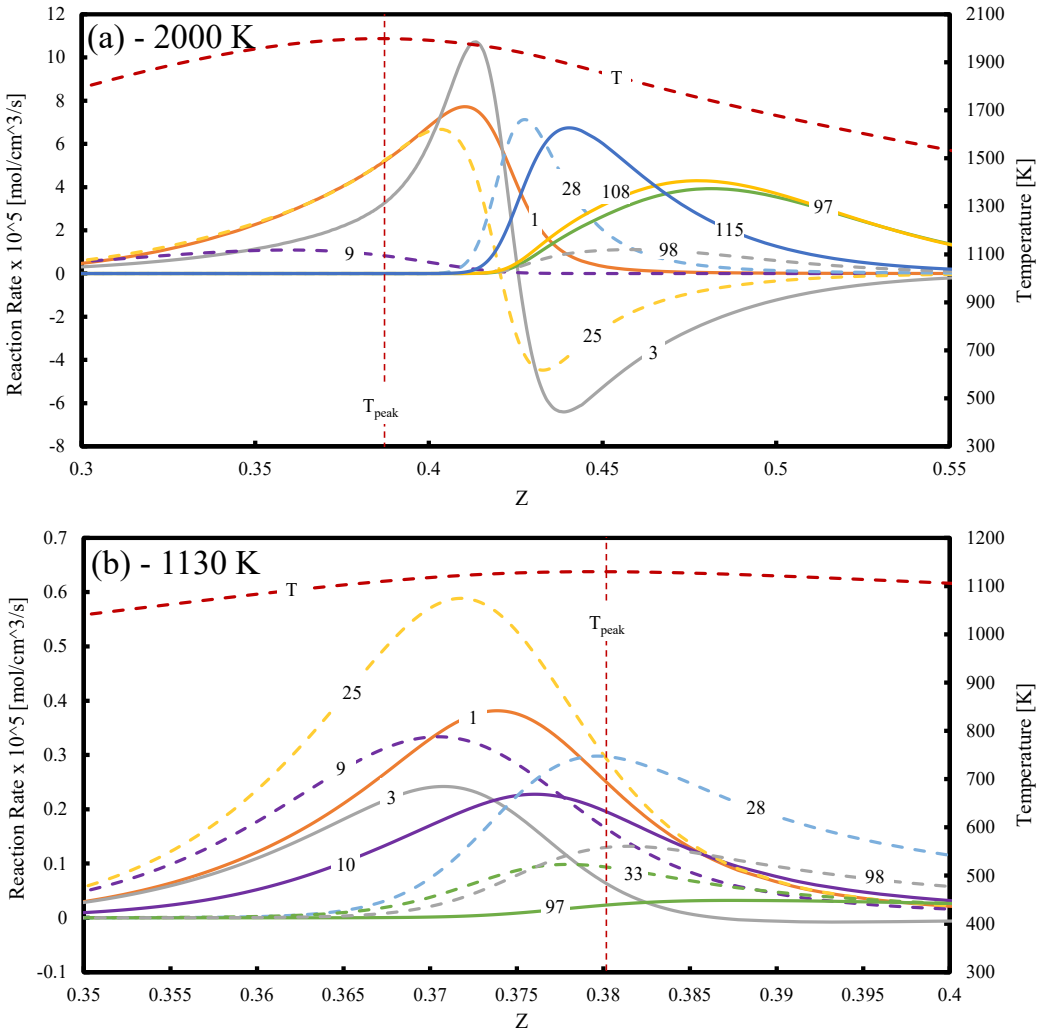

Fig. 3.5. Spatial profiles of reaction rate for selected reactions at (a) 2000 K and (b) 1130 K.

Spatial profiles of reaction rate help explain the shifting species concentrations with temperature. The main C_2H_2 production reaction is R108, which consumes the C_2H_3 produced by R97 and R98 at high temperature. At low temperature this reaction is almost nonexistent, removing the path for C_2H_2 production. The C_2H_3 that was

Table 3.2. Short list of important reactions for C_2H_4 oxidation. F indicates the forward reaction rate dominates, and R indicates the reverse reaction rate dominates.

Reaction	High Temperature		Low Temperature	
	Pyr.	Oxi.	Pyr.	Oxi.
1: $H + O_2 \leftrightarrow OH + O$		F		F
2: $H_2 + O \leftrightarrow OH + H$		F		
3: $H_2 + OH \leftrightarrow H_2O + H$	R	F		F
4: $H_2O + O \leftrightarrow 2OH$		F		F
6: $H + OH + M \leftrightarrow H_2O + M$		F		
9: $H + O_2 (+M) \leftrightarrow HO_2 (+M)$		F		F
10: $HO_2 + H \leftrightarrow 2OH$			F	F
11: $HO_2 + H \leftrightarrow H_2 + O_2$			F	F
12: $HO_2 + H \leftrightarrow H_2O + O$			F	F
13: $HO_2 + O \leftrightarrow OH + O_2$				F
14: $HO_2 + OH \leftrightarrow H_2O + O_2$		F		F
25: $CO + OH \leftrightarrow CO_2 + H$	R	F		F
28: $HCO + M \leftrightarrow CO + H + M$	F		F	
33: $HCO + O_2 \leftrightarrow CO + HO_2$			F	
36: $CH_2O + H \leftrightarrow HCO + H_2$	F		F	
38: $CH_2O + OH \leftrightarrow HCO + H_2O$	F		F	
49: $CH_3 + O \leftrightarrow CH_2O + H$	F		F	
96: $C_2H_5 (+M) \leftrightarrow C_2H_4 + H (+M)$			R	
97: $C_2H_4 + H \leftrightarrow C_2H_3 + H_2$	F		F	
98: $C_2H_4 + OH \leftrightarrow C_2H_3 + H_2O$	F		F	
99: $C_2H_4 + O \leftrightarrow CH_3 + HCO$			F	
108: $C_2H_3 (+M) \leftrightarrow C_2H_2 + H (+M)$	F			
109: $C_2H_3 + O_2 \leftrightarrow CH_2O + HCO$			F	
110: $C_2H_3 + O_2 \leftrightarrow CH_2CHO + O$			F	
115: $C_2H_2 + OH \leftrightarrow CH_2CO + H$	F			
117: $CH_2CO + H \leftrightarrow CH_3 + CO$	F		F	
134: $CH_2OH + O_2 \leftrightarrow CH_2O + HO_2$			F	
135: $CH_2OH + M \leftrightarrow CH_2O + H + M$	F			
137: $CH_2CO + OH \leftrightarrow CH_2OH + CO$	F		F	
146: $CH_2CHO \leftrightarrow CH_2CO + H$			F	

forming C_2H_2 now instead reacts with O_2 to form CH_2O (R110).

The main HO_2 production reaction at both temperatures is R9, which exists primarily on the oxidizer side for both conditions and has a consistent rate throughout, maintaining HO_2 levels in that region. The difference at low temperature is the emergence of R33 and R134, which have nearly identical profiles. These reactions, made possible by increased oxidizer levels on the fuel side, increase HO_2 levels in that region.

There are two reactions, R3 and R25, where the reverse reaction dominates in the pyrolysis zone and the forward reaction dominates in the oxidation zone at high temperature.

$$H_2 + OH \leftrightarrow H_2O + H \quad \text{(R3)}$$

$$CO + OH \leftrightarrow CO_2 + H \quad \text{(R25)}$$

The net rate for these reactions, along with the temperature and OH/H ratio, are shown in Fig. 3.6. There are a couple of reasons why these reactions can perform such a reversal. First, there is sufficient CO_2 and H_2O across the flame region to allow for a significant contribution from the reverse reaction rate. Second, the temperature in the system is high enough for the reverse reaction to occur. As temperature drops, the reverse reaction rate decreases until the forward reaction dominates throughout the entire domain. The equilibrium point between the forward and reverse rates coincides with the point in the system where H begins to dominate over OH. At high temperature, this point occurs on the fuel side of both peak temperature and Z_{st}, at roughly the edge of the pyrolysis zone.

To give a more general overview of the differences between high and low temperatures, the reaction rates and heat release rates were integrated across the entire domain. The resulting data is shown in Fig. 3.7. At high temperature, a large portion of heat release comes from R6, R9, R14, and R25, the main radical to product formation

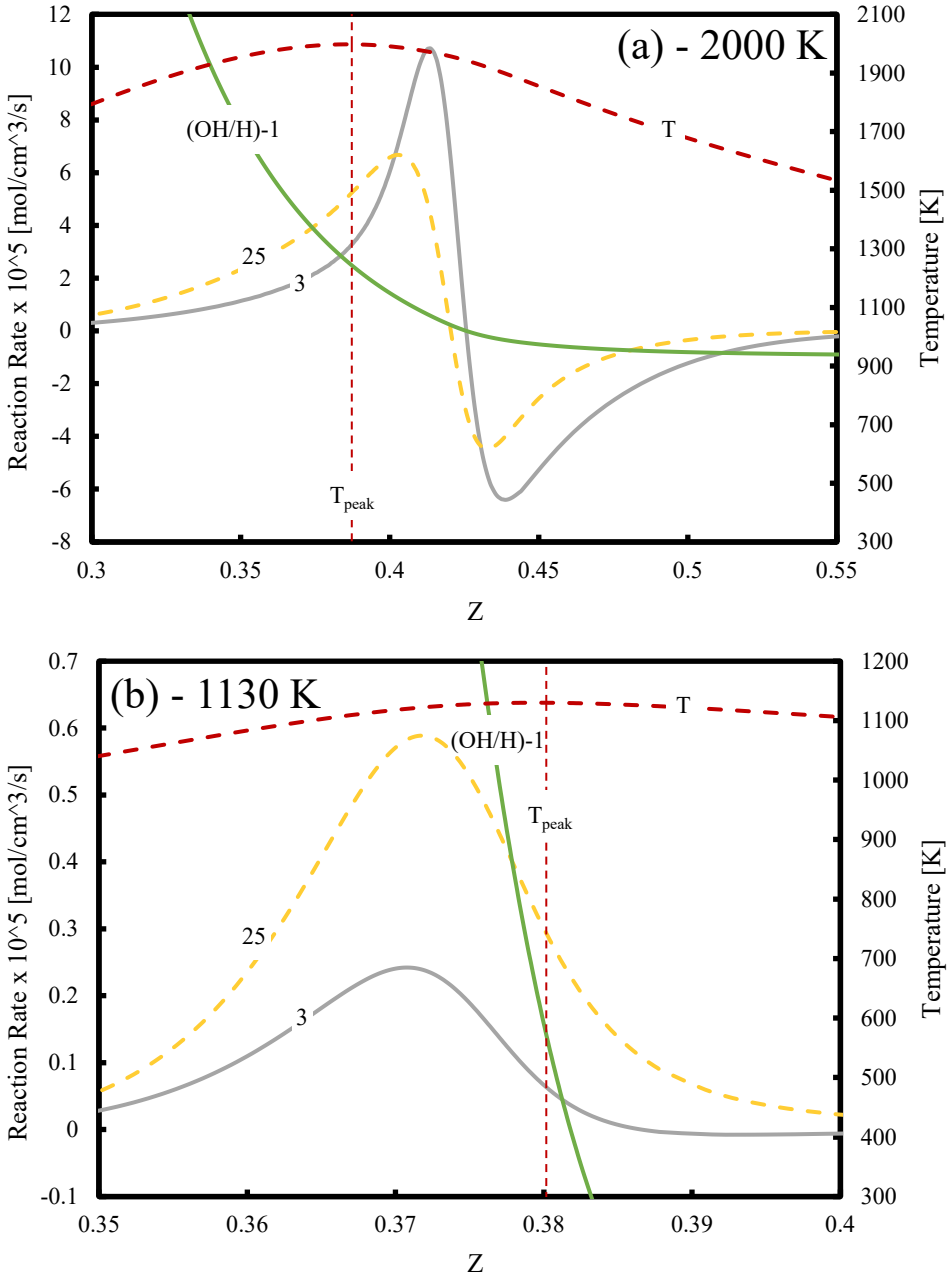

Fig. 3.6. Spatial profiles of reactions R3 and R25, temperature, and OH/H ratio at (a) 2000 K and (b) 1130 K.

reactions. This is much the same at low temperature, except for R6, a reaction between H and OH, which has been reduced to almost nothing. The H radicals instead prefer to react with HO_2 to form OH (R10). This reaction, made possible by increased HO_2 levels, is critical to sustaining combustion.

3.3.5 Reaction Pathways

As noted previously, reactant leakage across the flame zone increases with decreasing temperature, leading to an increase in oxidating species in the presence of

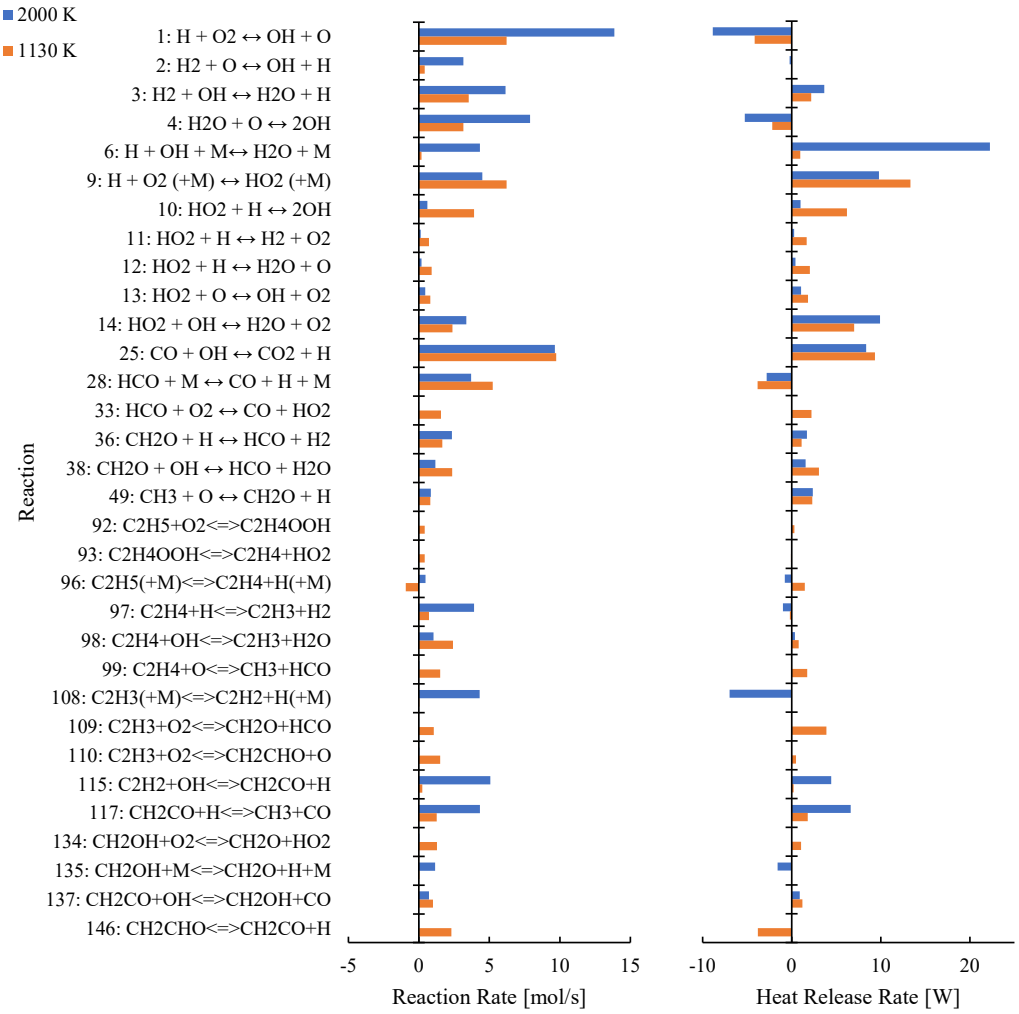

Fig. 3.7. Reaction rates and heat release rates integrated across the entire computational domain at 2000 K and 1130 K.

fuel. At high temperature the fuel mainly reacts with H (R97) and OH (R98) to form C_2H_3. While R98 is similarly important at low temperature, the significance of R97 has decreased, and the fuel is more likely to react O (R99). There is also a competing C_2H_4 + H reaction that forms C_2H_5 at low temperature (R96). This C_2H_5 then reacts with O_2 to form C_2H_4OOH (R92), an important species for warm and cool flame chemistry. The C_2H_4OOH then dissociates to form C_2H_4.

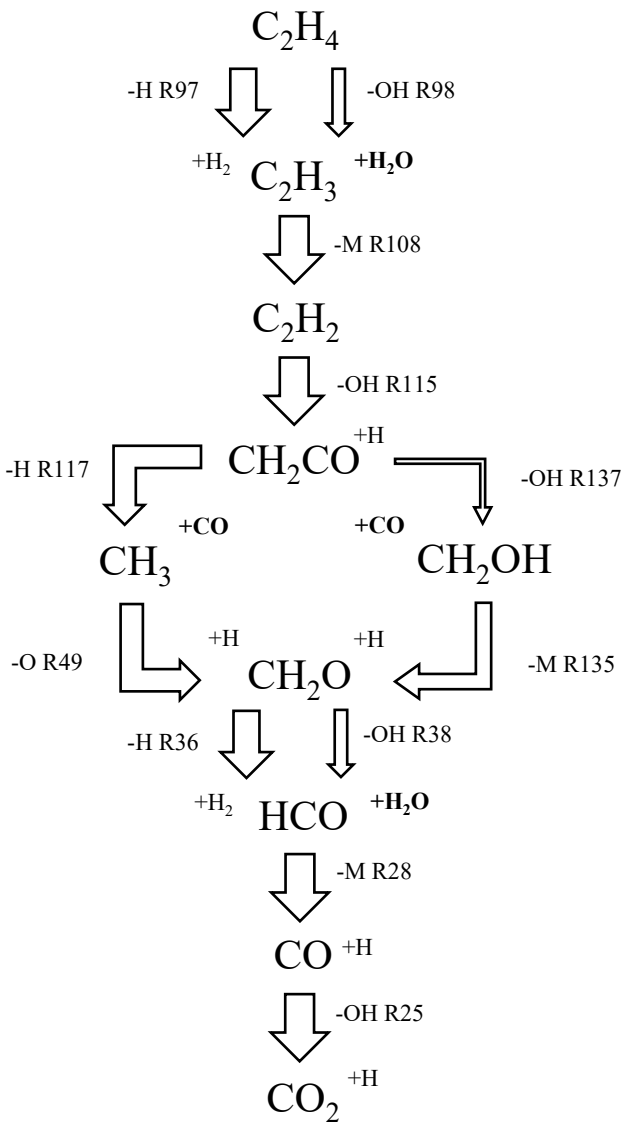

Fig. 3.8. Reaction pathways from C_2H_4 to CO_2 at 2000 K. Arrow width corresponds to relative importance of a particular path.

At high temperature the C_2H_3 reacts with a third body to form C_2H_2 (R108) which then reacts with OH to form CH_2CO (R115). The CH_2CO then has two paths to reach CH_2O. In the preferred path it reacts with H to form CH_3 (R117) which then reacts with O to form CH_2O (R49). In the secondary path it reacts with OH to form CH_2OH (R137), which reacts with a third body to form CH_2O (R135). The CH_2O reacts with either H (R36) or OH (R38) to form HCO, with R36 being preferred at high temperature. HCO then reacts with a third body to form CO (R28), which reacts with OH to form CO_2 (R25). This reaction pathway from C_2H_4 to CO_2 at high temperature is summarized in Fig. 3.8a.

Fig. 3.9 shows how the reaction pathway changes at low temperature. Many of the species are the same, with the exception that C_2H_2 no longer plays a major part in the mechanism. New pathways have emerged due to most reactions now taking place in the presence of oxidating species. Increased relative levels of O_2, OH, and O means reactions are more likely to occur with these species than with H. C_2H_3 now reacts with O_2 (R110) rather than any third body, and consequently forms CH_2CHO instead of C_2H_2. CH_2CHO then dissociates to form CH_2CO (R146), which, as before, has two paths to reach CH_2O. At high temperature the path through CH_3 is significantly more prevalent, but at low temperature the two paths proceed at more even rates. In the CH_2OH path, the reaction proceeds with O_2 rather than a third body to form CH_2O (R134). Additional HCO and CH_3 are also provided through R99, and there exists an alternate path to forming CO from HCO through reaction with O_2 (R33). Overall CO_2 formation is similar between high and low temperatures.

H_2O production occurs through several different steps. At high temperature R6 is

a major producer of H_2O, but this is not the case at low temperature. Instead, the rates of H_2O production reactions R12, R38, and R98 have increased and the rate of H_2O destruction reaction R4 has decreased, resulting in an increase in overall H_2O formation.

There are a few reactions critical to flame extinction. The first is R9, a significant

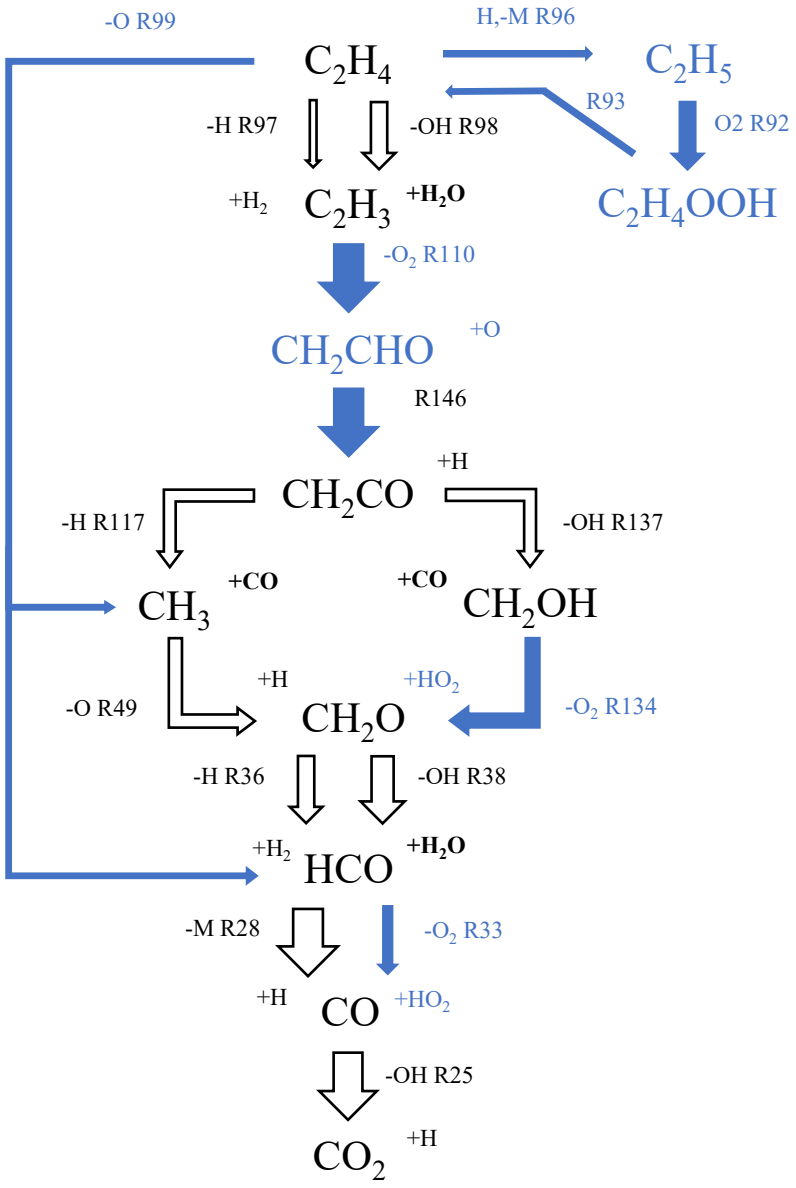

Fig. 3.9. Reaction pathways from C_2H_4 to CO_2 at 1130 K. Arrow width corresponds to relative importance of a particular path. Changes in the low temperature reaction pathway are indicated in blue.

heat release reaction at low temperature. Whereas the rate of most intermediate reactions decreases with temperature, R9 increases and can supply the flame with more heat. R33 and R109 follow a similar pattern. If the flame were to survive below 1130 K, the rate of these reactions would need to be further increased.

Another crucial reaction is R96, which introduces C_2H_5 to the system.

$$C_2H_4 + H\ (+M) \leftrightarrow C_2H_5\ (+M) \qquad \text{(R96)}$$

Note that R96 is written in the opposite direction in the mechanism, but the reverse reaction dominates at low temperatures. As shown in Fig. 3.8, the C_2H_5 further reacts to form C_2H_4OOH, which then forms C_2H_4, in R92 and R93.

$$C_2H_5 + O_2 \leftrightarrow C_2H_4OOH \qquad \text{(R92)}$$

$$C_2H_4OOH \leftrightarrow C_2H_4 + HO_2 \qquad \text{(R93)}$$

The overall result of these reactions is:

$$H + O_2\ (+M) \leftrightarrow HO_2\ (+M), \qquad \text{(R9)}$$

which is the same as R9. Reactions of this type are known to be critical to the chemistry of warm flames [13]. Thus, if the rate of R96 was increased, and consequently the rates of R92 and R93, the additional heat release could be enough to sustain the flame at lower temperatures. Since R9 and R96 are pressure dependent, it follows that an increase in pressure could facilitate warm flame formation, allowing the flame to survive to lower temperatures.

3.3.6 Global Reactions

Based on the mechanism presented in Fig. 3.8, the major reactions that contribute to the oxidation of C_2H_4 to CO_2 are presented in Table 3.2. They are separated by whether they are significant at high temperature or low temperature, and by in what

zone of the flame they primarily occur (i.e., pyrolysis or oxidation). Table 3.2 also indicates whether the forward or reverse reaction rate dominates in each zone. The result of this categorization is four sub-mechanisms: high temperature pyrolysis, high temperature oxidation, low temperature pyrolysis, and low temperature oxidation.

With this information, the global reactions which correspond to these sub-mechanisms can be determined using the C-matrix method, a special linear-algebraic procedure [48]. Within this procedure the species are divided into two groups: minor species, which have very small concentrations, and major species, which have concentrations that could not be neglected. The C-matrix method eliminates the minor species using the determination of the Reduced Row Echelon Form (RRE Form) of the stoichiometric C-matrix and identifies the global reactions uniquely. Such ordering of the occurring substances is chosen, in which all minor species are listed first, and major species second.

Here, the minor species are C2H3, CH2CO, CH2OH, CH3, H, HCO, O, and OH, and the major species are C2H2, C2H4, CH2O, CO, CO2, H2, H2O, and O2. The resulting global reactions for the four sub-mechanisms are shown in Table 3.3, along

Table 3.3. Global reactions for each zone, and overall global reactions, for high and low temperature.

	Pyrolysis	Oxidation	Global
High Temperature	$C_2H_4 + 4\ H_2O = 2\ CO_2 + 6\ H_2$ $C_2H_2 + 4\ H_2O = 2\ CO_2 + 5\ H_2$ $CH_2O + H_2O = CO_2 + 2\ H_2$ $CO + H_2O = CO_2 + H_2$	$2\ CO + O_2 = 2\ CO_2$ $2\ H_2 + O_2 = 2\ H_2O$	$C_2H_4 + 3\ O_2 = 2\ CO_2 + 2\ H_2O$ $2\ C_2H_2 + 5\ O_2 = 4\ CO_2 + 2\ H_2O$ $CH_2O + O_2 = CO_2 + H_2O$ $2\ CO + O_2 = 2\ CO_2$ $2\ H_2 + O_2 = 2\ H_2O$
Low Temperature	$C_2H_4 + 2\ O_2 = 2\ CO + 2\ H_2O$ $2\ CH_2O + O_2 = 2\ CO + 2\ H_2O$ $2\ H_2 + O_2 = 2\ H_2O$	$2\ CO + O_2 = 2\ CO_2$ $2\ H_2 + O_2 = 2\ H_2O$	$C_2H_4 + 3\ O_2 = 2\ CO_2 + 2\ H_2O$ $CH_2O + O_2 = CO_2 + H_2O$ $2\ CO + O_2 = 2\ CO_2$ $2\ H_2 + O_2 = 2\ H_2O$

with the overall global reactions. The only difference between the overall global reactions at high and low temperature is the removal of the C_2H_2 reaction, since C_2H_2 levels have dropped significantly at low temperature.

The selection of major species can be verified by confirming that the majority of C, H, and O atoms in the system are accounted for by these major species. This comparison is shown in Fig. 3.10. Since the majority of C, H, and O atoms are in fact accounted for by the major species, the selection of major species is valid.

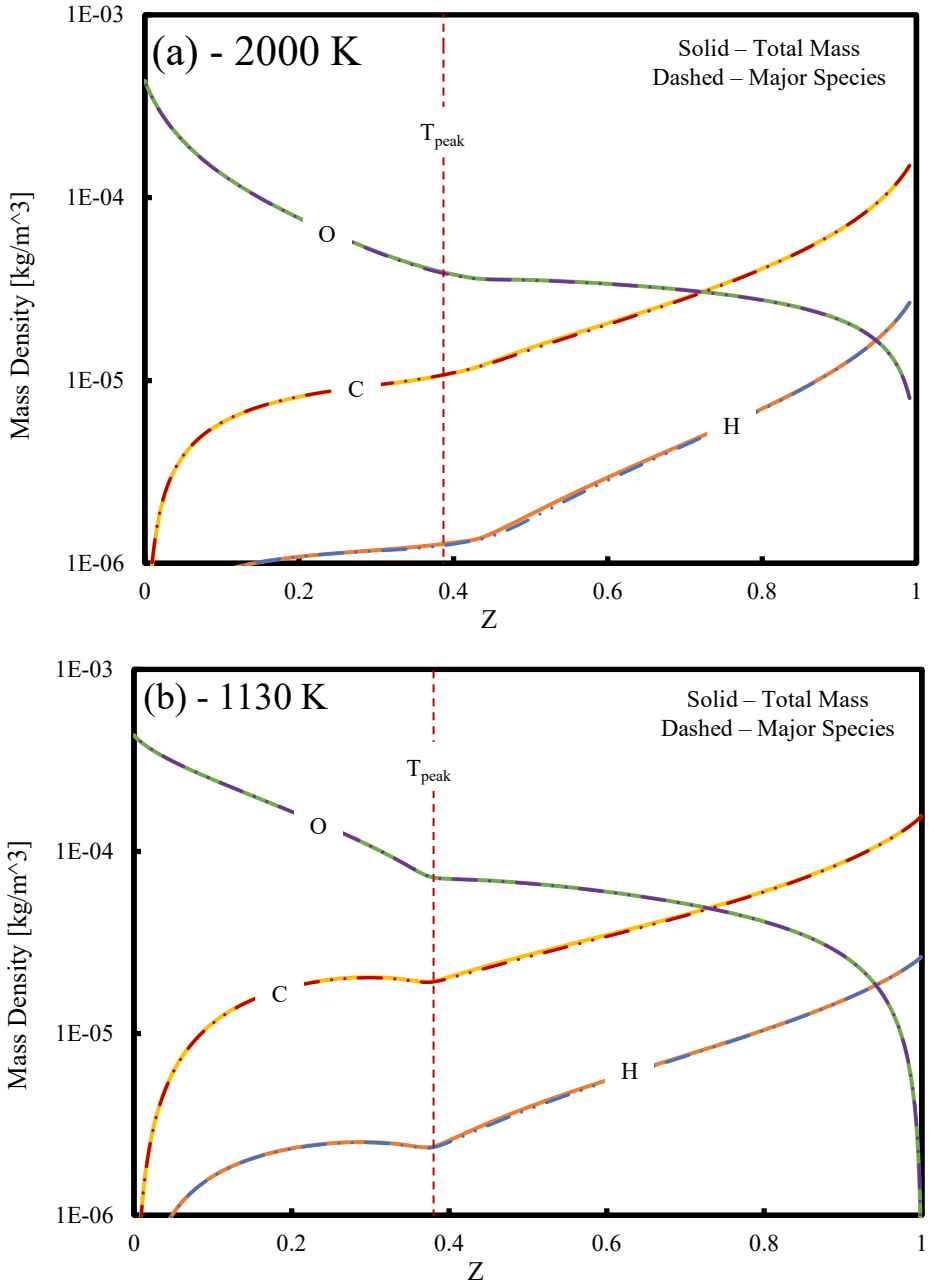

Fig. 3.10. Contribution of major species to total C, H, and O atoms in the system at (a) 2000 K and (b) 1130 K.

3.4 Summary

The kinetics leading to radiative extinction of ethylene microgravity spherical diffusion flames were studied. The main conclusions are as follows.

1. As the peak temperature decreases more fuel and oxidizer leak across the region of peak temperature, leading to the emergence of new reaction pathways. Simultaneously the stoichiometric location shifts toward the fuel side.
2. The new pathways facilitate HO_2 formation, which helps sustain the radical pool as temperatures decrease. HO_2 levels increase across the entire flame region, and its reactions contribute significantly to the overall heat release rate at low temperatures.
3. C_2H_4 mainly reacts with H at high temperature, with a small contribution from OH due to long residence times and elevated OH levels from the destruction of CO_2 and H_2O. At low temperature, C_2H_4 destruction sees more equal contributions from H, OH, and O.
4. Warm flame chemistry involving C_2H_5, C_2H_4OOH, and HO_2 emerges at low temperature, but is not enough to sustain the flame before it extinguishes.

The next chapter will discuss the effects of increasing ambient pressure and whether this will facilitate warm and cool flame chemistry.

Chapter 4 Spherical Flame Kinetics at Elevated Pressure

4.1 Introduction

In the preceding chapter the kinetics of ethylene microgravity spherical diffusion flames were discussed. Due to the influence of pressure dependent reactions on HO_2 production and low temperature chemistry, it was posited that increasing ambient pressure would enhance the low temperature chemistry and allow the flame to survive at lower temperatures. Elevated pressures are known to promote cool flame formation, due to the kinetics that govern negative temperature coefficient (NTC) behavior [49]. Cool diffusion flame (CDF) experiments with a spherical burner aboard the International Space Station (ISS) found that butane CDFs would only form at a pressure of 2 atm despite the same conditions being tested at 1 atm [7].

Cool flames have been observed for C_2H_4 before [50], and others have describe some of the low temperature oxidation reactions of C_2H_4, as it is an important intermediate for heavier alkanes [51]. C_2H_4 is not known to exhibit particularly strong NTC behavior, so large increases in pressure may be needed to facilitate cool flame formation. This chapter will examine how the kinetics of C_2H_4 microgravity spherical diffusion flames change at elevated pressures, and what warm and cool flame chemistry emerges.

4.2 Methods

4.2.1 Experimental

Experiments were conducted aboard the ISS; a complete description of the experimental apparatus can be found in Chapter 2. The fuel here is ethylene, and the

experimental flames considered here were in the inverse configuration, while the numerical simulation was in the normal configuration. Pressure varied from 0.5 to 3 atm.

4.2.2 Numerical

The numerical model employed here is the same as in previous chapters, and details can be found in Chapter 2. For the simulations performed here the inner boundary was maintained at the ambient temperature of 298 K. The UCSD mechanism was employed again here. It has been validated for low temperature chemistry and for pressures up to 50 atm [49,52].

The main effect of pressure on the numerical model is in the rates of reactions involving a third body, M. Typically, M is always included for a reaction requiring a third body to conserve momentum, but this is not the case in Chemkin. Chemkin handles pressure dependence in three forms, depending on how the reaction is specified in the input files. The first form is:

$$A + B \leftrightarrow C, \tag{4.1}$$

reactions of this form are considered to be independent of pressure. The second form is:

$$A + B + M \leftrightarrow C + M, \tag{4.2}$$

reactions of this form are considered to be in the low-pressure limiting region. The third form is:

$$A + B\ (+M) \leftrightarrow C\ (+M), \tag{4.3}$$

reactions of this form are considered to be in the fall off region. Additional inputs are required, and the pressure dependence is calculated using either the Troe or Lindemann

formula. For simplicity, these forms will be used here as well when describing reactions that may include a third body.

4.3 Results

4.3.1 Experimental Results

The conditions for three flames from the ISS are shown in Table 4.1. These were inverse flames, with oxidizer diluted with nitrogen issuing into a fuel/nitrogen

Table 4.1: Experimental conditions

Test	X_{fuel}	X_{O2}	$\dot{m}_{O2}$ [mg/s]	Z_{st}	T_{ad} [K]	p [atm]
A	0.100	0.850	3.41	0.716	2480	1
B	0.100	0.850	3.41	0.716	2480	3
C	0.100	0.850	3.41	0.716	2480	0.5

mixture. All three flames had the same conditions except for chamber pressure, with was 1 atm for Flame A, 3 atm for Flame B, and 0.5 atm for flame C.

The resulting temperature vs. time data based on TFP measurements are shown in Fig. 4.1. The result of changing pressure is that peak flame temperature decreases with increasing pressure. Flame A and C extinguish at similar temperatures, but Flame B extinguishes roughly 50 K lower. This further reinforces the idea that increased ambient pressure promotes low temperature chemistry and can allow these flames to exist at lower temperatures.

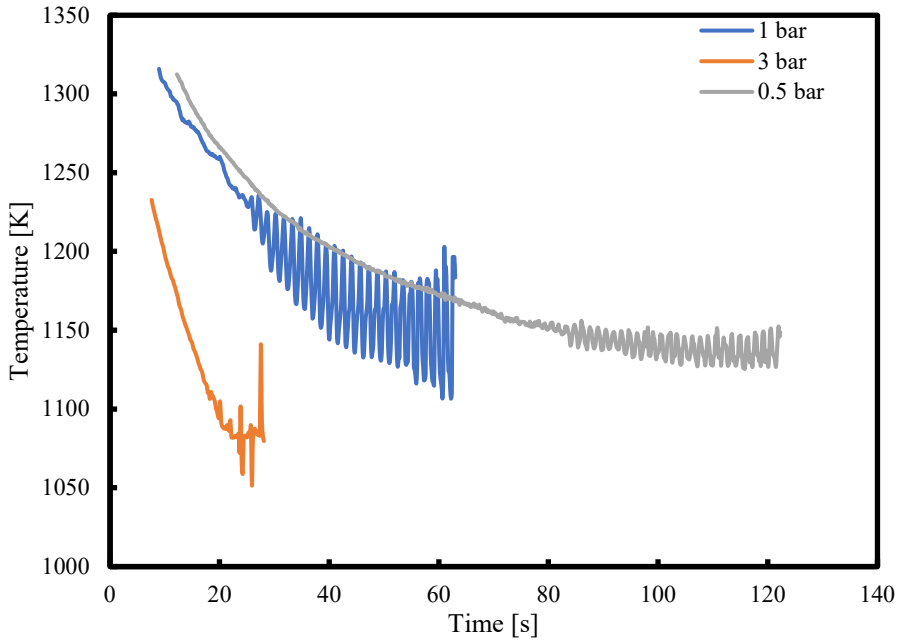

Fig. 4.1. TFP temperature for experimental inverse flames with the same dilution at 3 different pressures.

4.3.2 Numerical Simulation

With this in mind, another simulation was performed with the same conditions as in Chapter 3, with the ambient pressure increased to 50 atm, as shown in Table 4.2. The temporal evolutions of peak temperature, flame radius, and radiative loss fraction (total radiation relative to total heat release, Q_R/Q_C) are shown in Fig. 4.2. The early period, when the flame is a hot flame, is similar to the behavior at 1 atm. The flame ignites at a high temperature and as the flame grows radiative losses increase, decreasing the temperature. The difference is that the flame no longer extinguishes at the normal temperature, but rather the temperature keeps dropping below 1100 K all the way down to around 800 K. Since the effect of radiation decreases with

Table 4.2: Numerical simulation conditions

X_{fuel}	X_{O2}	$\dot{m}_{fuel}$ [mg/s]	Z_{st}	T_{ad} [K]	p [atm]
0.159	0.333	1.5	0.4	2366	50

decreasing temperature, the rate at which the temperature drops slows to the point that this only happens after 550 s. This region when the peak temperature is above 1100 K is considered the hot flame regime, and the region when the peak temperature is between 1100 K and 800 K is considered the warm flame regime.

Once the flame reaches 800 K, it undergoes a sharp transition to a cool flame. The flame starts to extinguish as is typical, with Q_C decreasing sharply due to the loss of combustion reactions and Q_R remaining relatively stable, causing Q_R/Q_C to increase sharply. Then, cool flame chemistry kicks in and begins to release new heat, bringing the Q_R/Q_C back down. The cool flame temperature is low, and it produces few new radiating products, so the cool flame temperature increases with time, as opposed to the hot or warm flames. The initial cool flame temperature is ~650 K, and it rises to ~700 K before the flame experiences another sudden transition and attempts

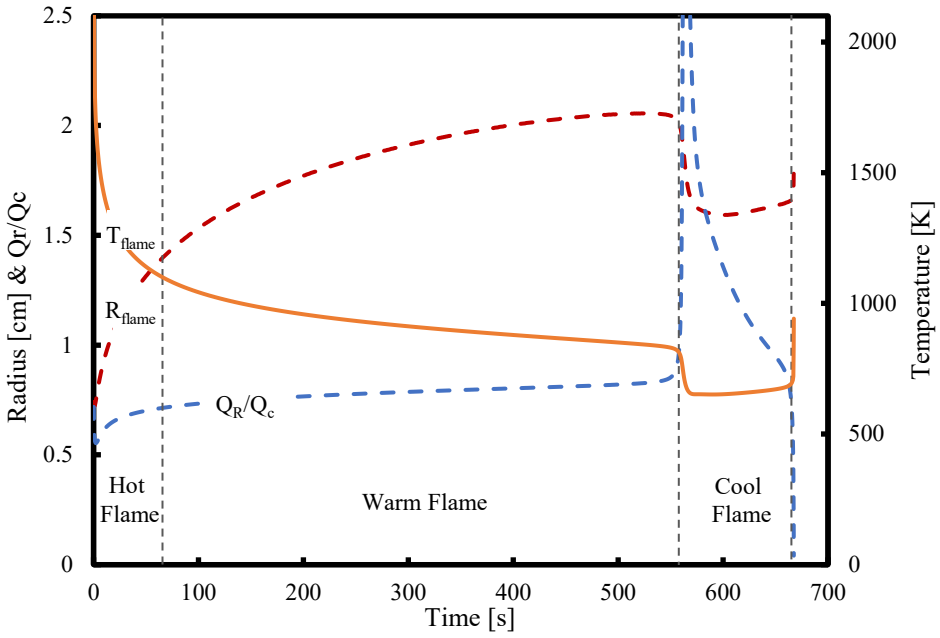

Fig. 4.2. Simulated temporal evolution of peak temperature, flame radius, and radiative loss fraction for a normal flame at 50 atm. Vertical lines indicate the hot flame (T > 1100 K), warm flame (1100 K > T > 800 K), and cool flame (T < 800 K) regimes.

to reignite to a hot flame, as evidenced by shar increases in temperature and Q_C. At this point the gradients are too much for the model to handle, and it crashes. If the simulation were able to continue running after this point, it is expected that the hot flame would reestablish, and the cycle would repeat. This phenomenon was also seen in [7], where repeated cool flame to hot flame ignitions were observed for butane spherical diffusion flames.

4.3.3 Spatial Profiles

This behavior allows the flames properties to be studied over a wide range of temperatures for the same level of reactant dilution. To facilitate this examination, four times were chosen to examine the spatial properties of the flame: when the peak temperature was 2000 K, 1130 K, 830 K, and 660 K. These correspond to the high temperature hot flame, low temperature hot flame, warm flame, and cool flame regimes, respectively. Fig. 4.3a shows profiles of temperature, fuel mole fraction, and oxidizer mole fraction for the warm flame and cool flame in physical space, and Fig. 4.3b shows the same profiles in mixture fraction (Z) space. The following plots in this chapter will be in terms of Z, corresponding plots in physical space can be found in Appendix C. The low temperature hot flame and warm flame profiles are similar to the high temperature hot flames, except the profiles are broader and there is slightly increased reactant leakage. The location of Z_{st} is similar for the hot and warm flames, and moves from slightly on the fuel side at 2000 K and 1130 K to slightly on the oxidizer side at 830 K. This is due to more reactant leakage across the flame as temperature decreases. For the cool flame reactant leakage has increased

significantly, and the location of Z_{st} is now considerably displaced to the oxidizer side of peak temperature.

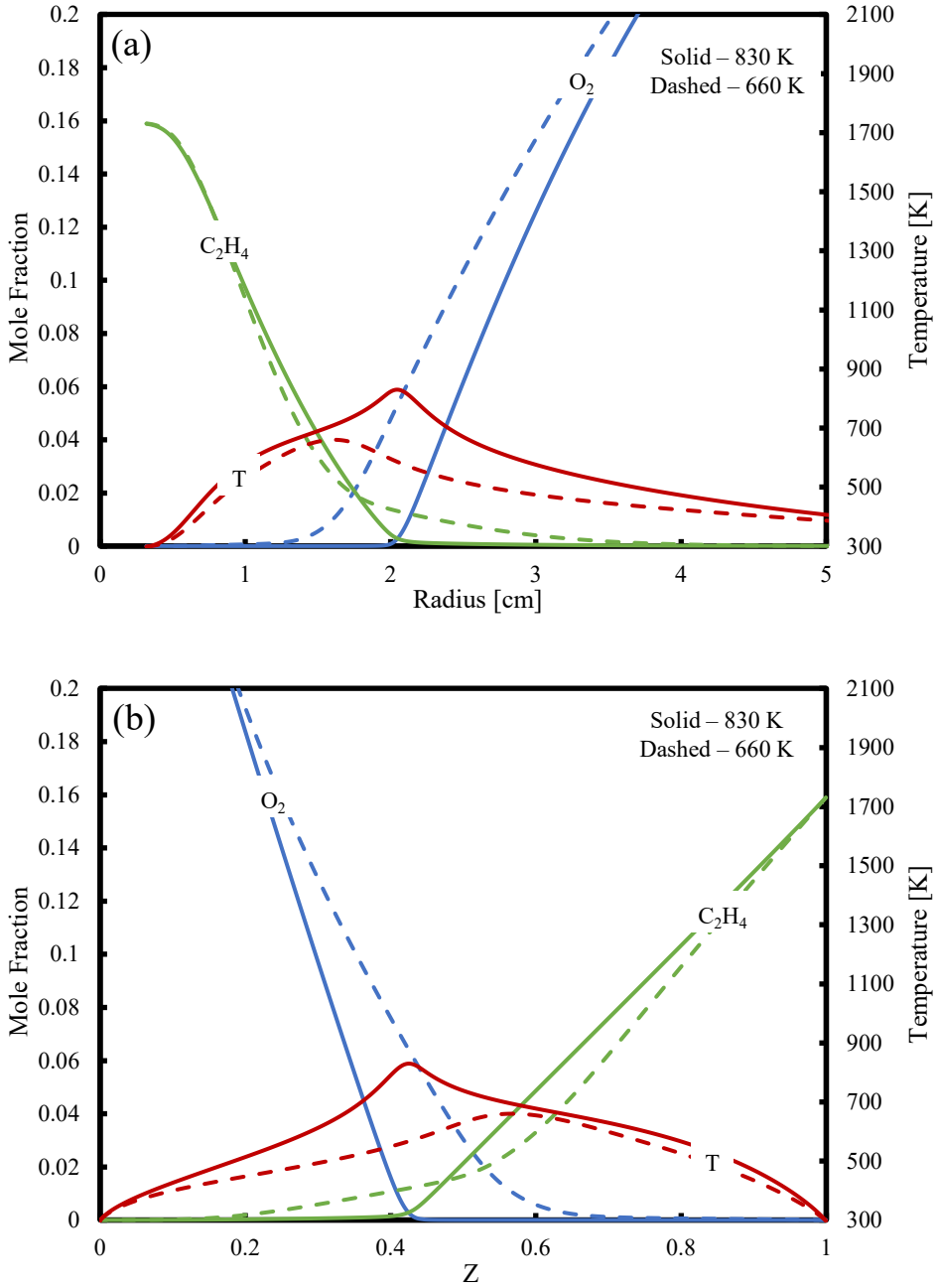

Fig. 4.3. Spatial profiles of peak temperature and fuel and oxidizer mole fraction for the warm and cool flame in (a) physical space and (b) mixture fraction space.

4.3.4 Mole Fractions

Spatial profiles of CO_2, H_2O, CO, H_2, C_2H_2, CH_2O, and H_2O_2 are shown in Fig. 4.4 and

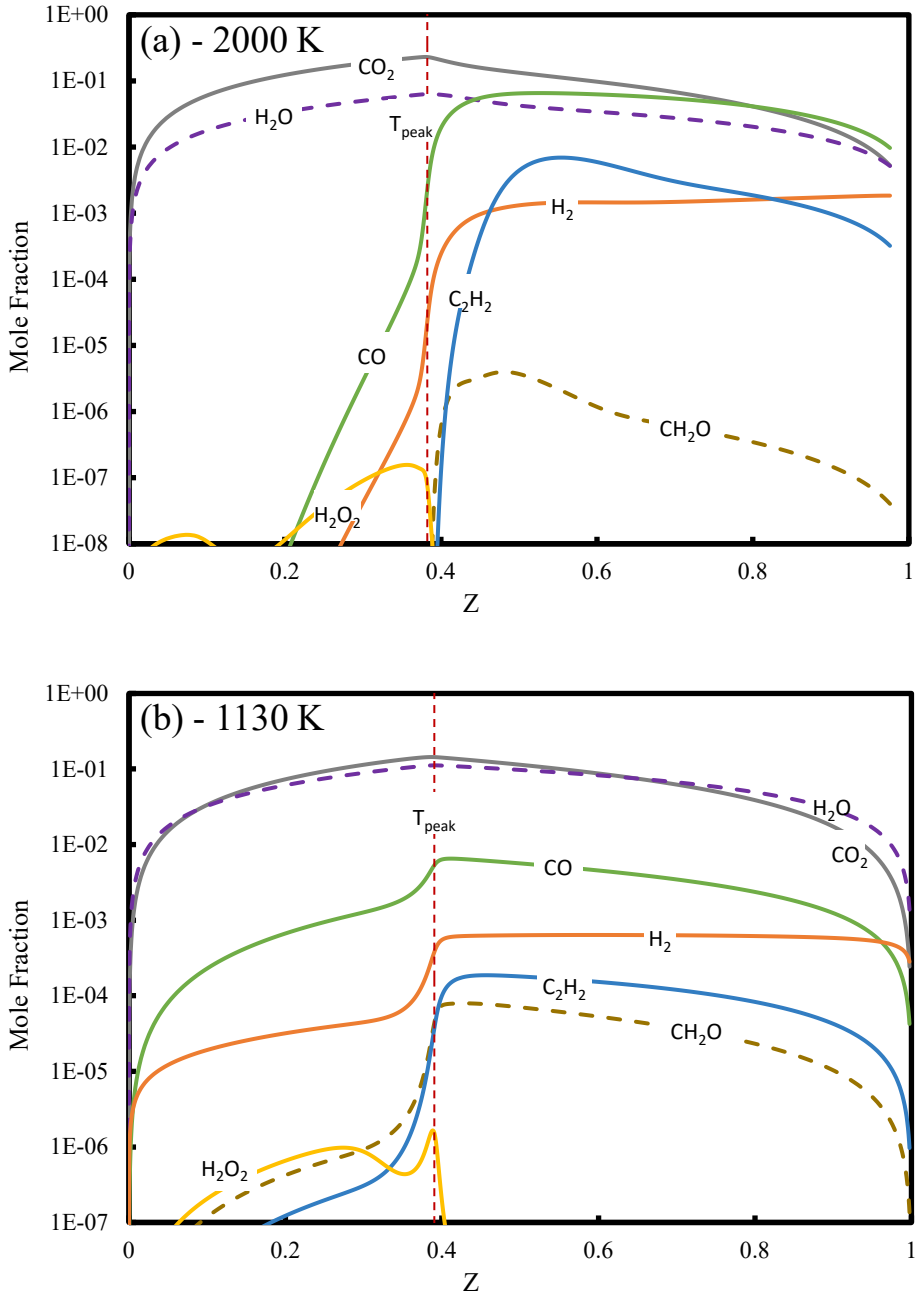

Fig. 4.4. Spatial profiles of CO2, H2O, CO, H2, CH2O, C2H2 and H2O2 mole fractions at (a) 2000 and (b) 1130 K.

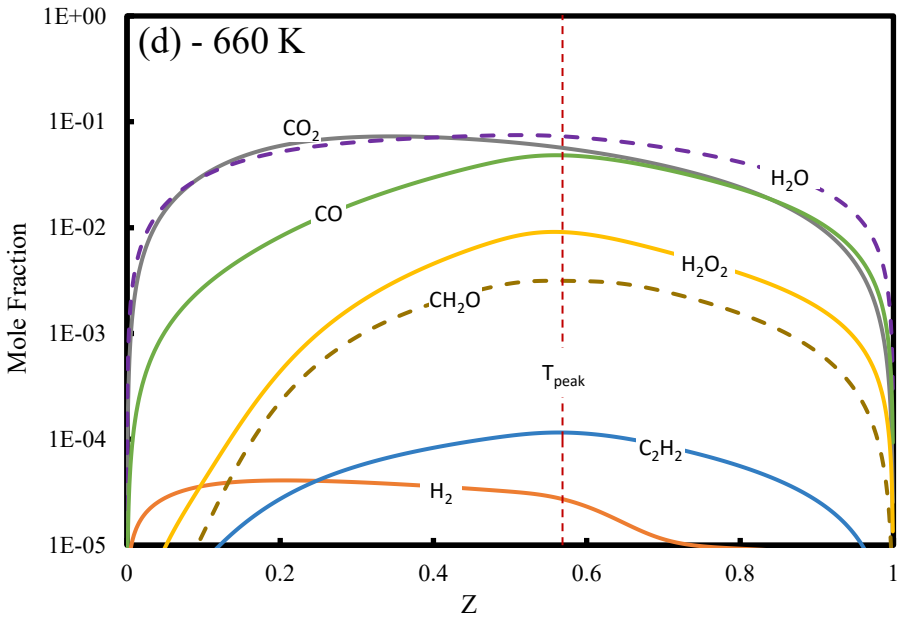

Fig. 4.5. For the hot flame this is much the same as the 1 atm case, with CO_2 and H_2O present at elevated levels throughout the region of interest, and the mole fractions of CO and H_2 decreasing with temperature. As the flame enters the warm

flame regime CO concentration increases relative to the CO_2 and H_2O concentrations, while the H_2 concentration continues to decrease. During the cool flame there is little CO_2 and H_2O formation and significant CO production, resulting in the CO concentration elevating to a similar value to that of the major products.

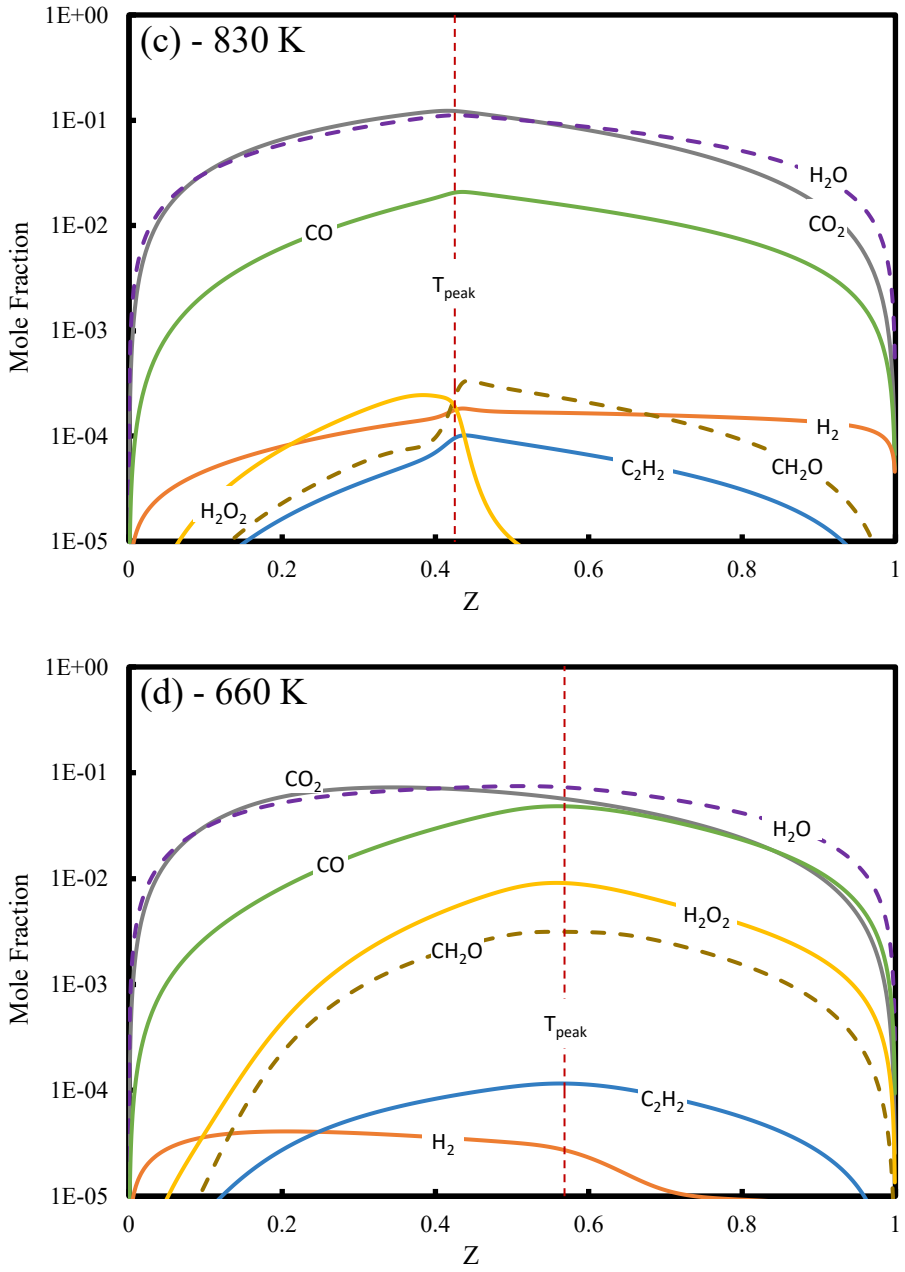

Fig. 4.5. Spatial profiles of CO2, H2O, CO, H2, CH2O, C2H2 and H2O2 mole fractions at (c) 830 K and (d) 660 K.

As in the atmospheric pressure case, the C_2H_2 concentration is elevated at high temperature while the CH_2O concentration is low. As temperature decreases the concentrations of the species experience the opposite trend until there is significantly more CH_2O than C_2H_2 in the cool flame regime. H_2O_2 concentration also increases as temperature decreases, to the point that H_2O_2 concentration is higher than CH_2O concentration for the cool flame.

Fig. 4.6 and Fig. 4.7 show spatial mole fraction profiles of H, OH, O, and HO_2. OH is the most prevalent of these at high temperature, and HO_2 levels at high temperature are increased compared to the atmospheric pressure case. By the time the flame reaches 1130 K, HO_2 is the dominant radical throughout the flame region. This

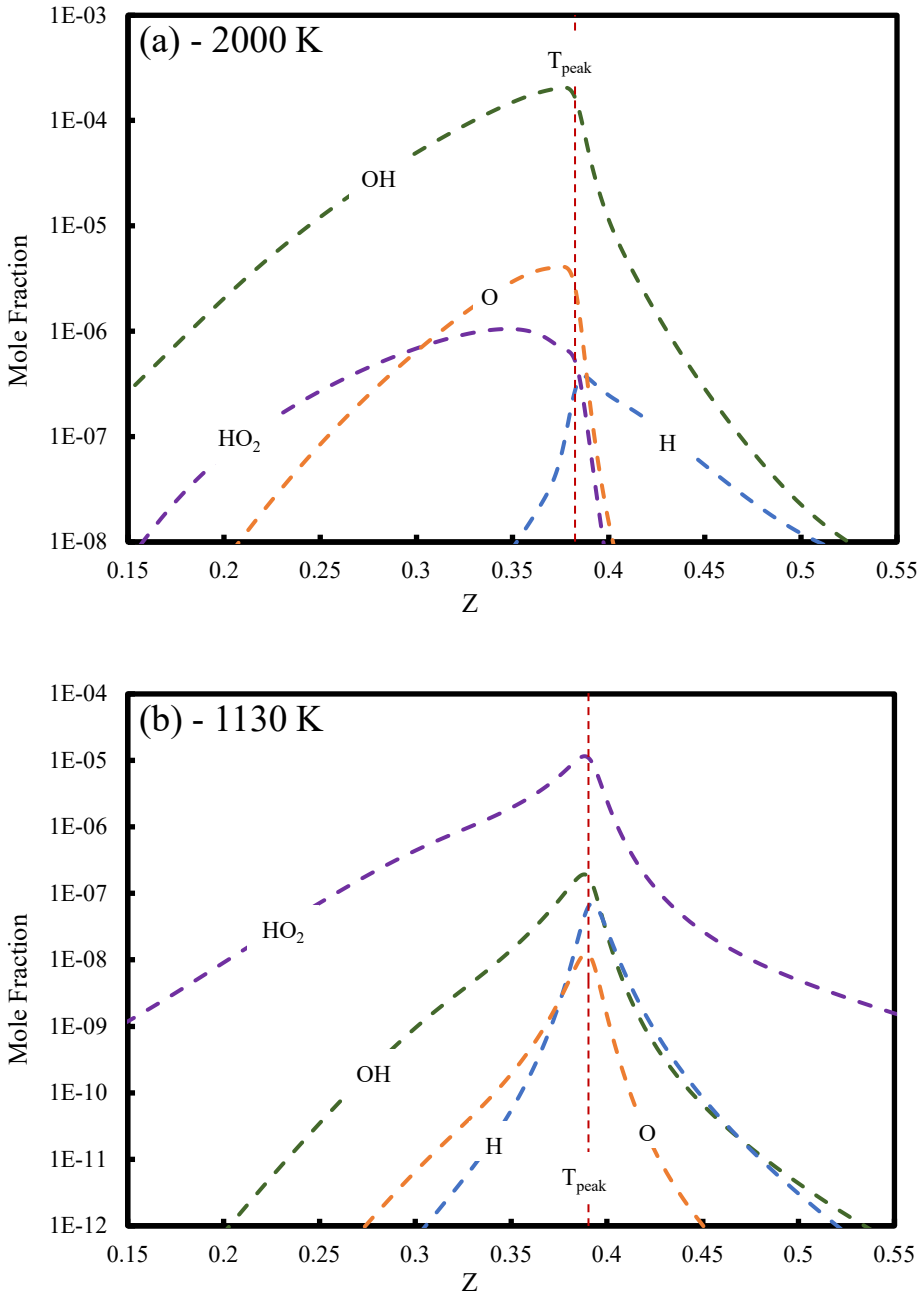

Fig. 4.6. Spatial profiles of O, OH, H, and HO_2 mole fractions at (a) 2000 and (b) 1130 K.

continues throughout the rest of the flame, with the HO_2 concentration decreasing in the warm flame regime and then holding steady throughout the cool flame, and the concentrations of H, OH, and O continually decreasing. In the cool flame the profiles of these radicals are much broader than they are for the hot and warm flame regimes.

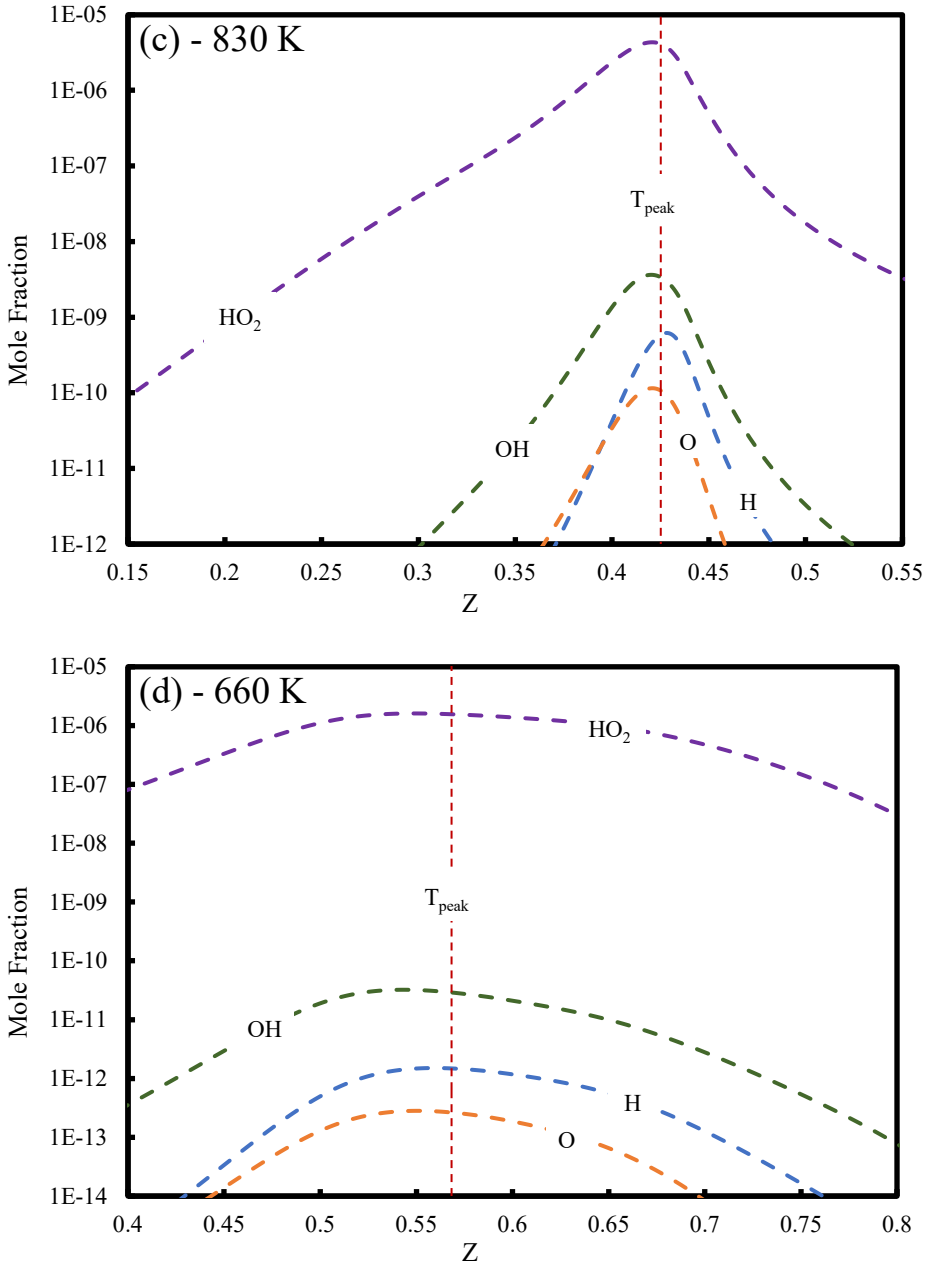

Fig. 4.7. Spatial profiles of O, OH, H, and HO_2 mole fractions at (c) 830 K and (d) 660 K.

4.3.5 Reaction Rates

Fig. 4.8 and Fig. 4.9 show spatial profiles of net reaction rate for the four temperature regimes. At high temperature there are distinct pyrolysis and oxidation zones, and these zones are even more distinct than they were for the same temperature at 1 atm. The oxidation zone coincides with the location of peak temperature, and the pyrolysis zone is on the fuel side. Both zones still exist at 1130 K and 830 K, but there is more overlap between them. Now the oxidation zone is primarily on the oxidizer side, and the pyrolysis zone is mainly on the fuel side. At 660 K there is one broad zone across the location of peak temperature in which most reactions occur.

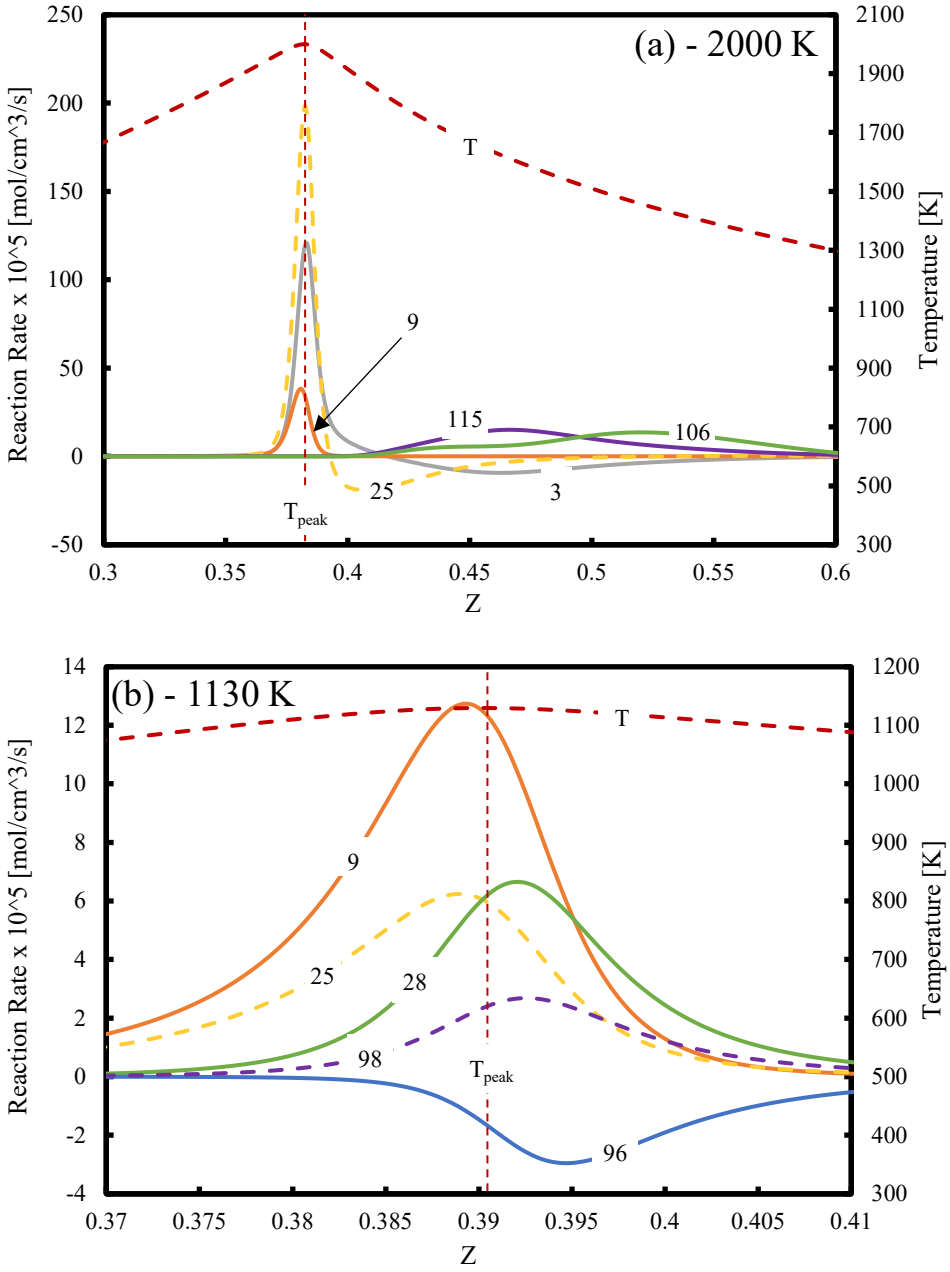

Fig. 4.8. Spatial profiles of reaction rate for selected reactions at (a) 2000 and (b) 1130 K.

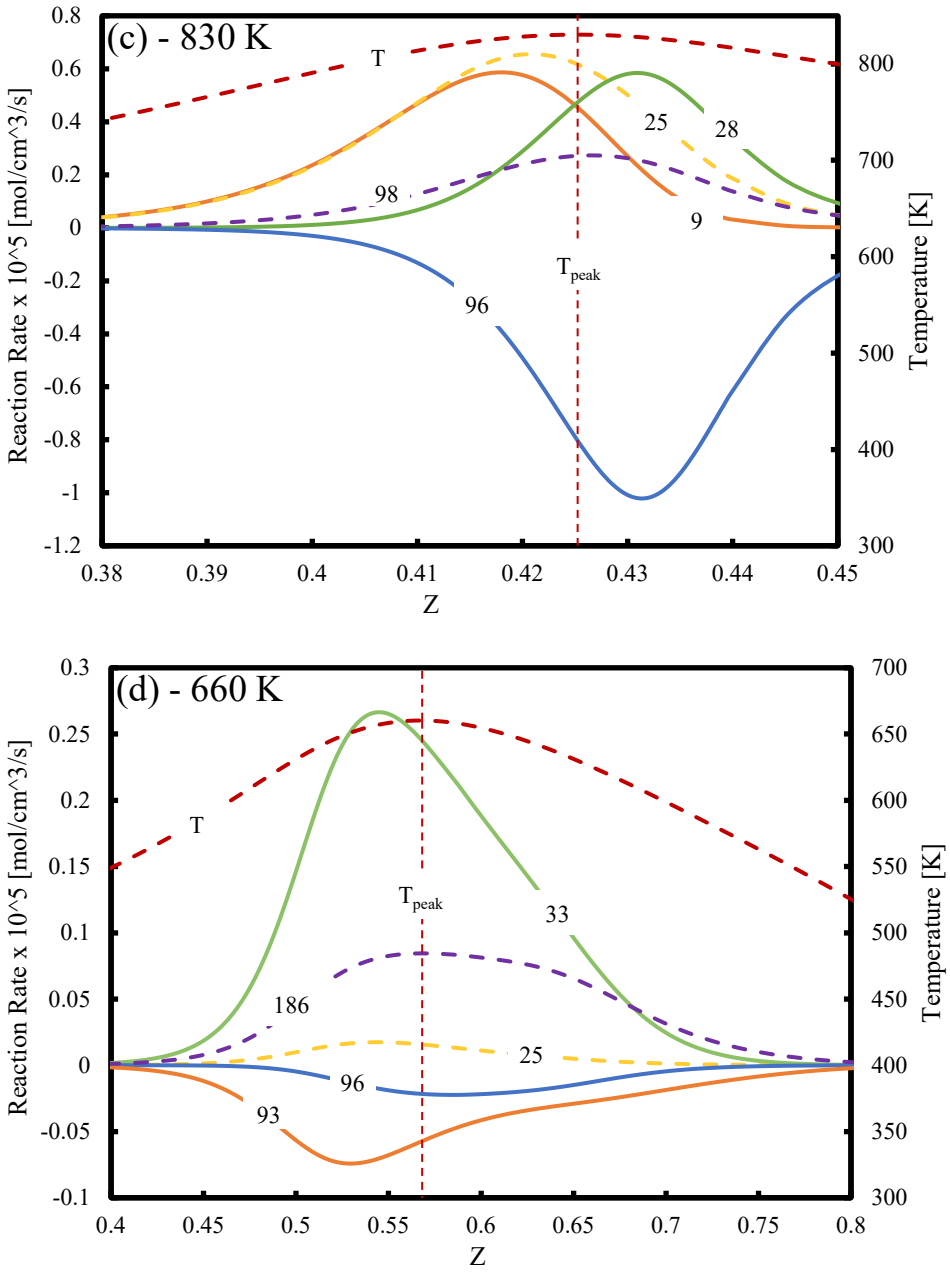

Fig. 4.9. Spatial profiles of reaction rate for selected reactions at (c) 830 K and (d) 660 K.

Table 4.3. List of relevant reactions in the different flame regimes. The primary direction of the reaction in each regime is indicated by F for forward and R for reverse.

Reaction	Hot Flame High T	Hot Flame Low T	Warm Flame	Cool Flame
1: $H + O_2 \leftrightarrow OH + O$	F			
3: $H_2 + OH \leftrightarrow H_2O + H$	F	F		
4: $H_2O + O \leftrightarrow 2OH$	F			
6: $H + OH + M \leftrightarrow H_2O + M$	F			
9: $H + O_2 (+ M) \leftrightarrow HO_2 (+ M)$	F	F	F	
10: $HO_2 + H \leftrightarrow 2OH$		F		
14: $HO_2 + OH \leftrightarrow H_2O + O_2$	F	F		
16: $2OH (+ M) \leftrightarrow H_2O_2 (+ M)$		R	R	
17: $2HO_2 \leftrightarrow H_2O_2 + O_2$		F	F	F
21: $H_2O_2 + OH \leftrightarrow H_2O + HO_2$			F	F
25: $CO + OH \leftrightarrow CO_2 + H$	F	F	F	F
26: $CO + HO_2 \leftrightarrow CO_2 + OH$		F	F	
28: $HCO + M \leftrightarrow CO + H + M$	F	F	F	
33: $HCO + O_2 \leftrightarrow CO + HO_2$		F	F	F
36: $CH_2O + H \leftrightarrow HCO + H_2$	F	F		
38: $CH_2O + OH \leftrightarrow HCO + H_2O$	F	F	F	F
40: $CH_2O + HO_2 \leftrightarrow HCO + H_2O_2$			F	F
51: $CH_3 + HO_2 \leftrightarrow CH_3O + OH$		F	F	
57: $2CH_3 (+ M) \leftrightarrow C_2H_6 (+ M)$	F			
81: $CH_3O + M \leftrightarrow CH_2O + H + M$	F	F	F	
91: $C_2H_5 + O_2 \leftrightarrow C_2H_4 + HO_2$			F	
92: $C_2H_5 + O_2 \leftrightarrow C_2H_4OOH$			F	
93: $C_2H_4OOH \leftrightarrow C_2H_4 + HO_2$			F	R
94: $C_2H_4OOH + O_2 \leftrightarrow OC_2H_3OOH + OH$				F
95: $OC_2H_3OOH \leftrightarrow CH2O + HCO + OH$				F
96: $C_2H_5 (+ M) \leftrightarrow C_2H_4 + H (+ M)$	F	R	R	
97: $C_2H_4 + H \leftrightarrow C_2H_3 + H_2$	F			
98: $C_2H_4 + OH \leftrightarrow C_2H_3 + H_2O$		F	F	F
106: $C_2H_4 + M \leftrightarrow C_2H_2 + H_2 + M$	F			
108: $C_2H_3 (+ M) \leftrightarrow C_2H_2 + H (+ M)$	F			
109: $C_2H_3 + O_2 \leftrightarrow CH_2O + HCO$		F	F	
110: $C_2H_3 + O_2 \leftrightarrow CH_2CHO + O$		F	F	
111: $C_2H_3 + O_2 \leftrightarrow C_2H_2 + HO_2$				
115: $C_2H_2 + OH \leftrightarrow CH_2CO + H$	F			
117: $CH_2CO + H \leftrightarrow CH_3 + CO$	F	F		
134: $CH_2OH + O_2 \leftrightarrow CH_2O + HO_2$		F	F	
135: $CH_2OH + M \leftrightarrow CH_2O + H + M$	F			
137: $CH_2CO + OH \leftrightarrow CH_2OH + CO$	F	F		
146: $CH_2CHO \leftrightarrow CH_2CO + H$		F		
151: $CH_2CHO + O_2 \leftrightarrow CH_2O + CO + OH$			F	F
157: $CH_3CO (+ M) \leftrightarrow CH_3 + CO (+ M)$		F	F	F
158: $CH_3CHO + OH \leftrightarrow CH_3CO + H_2O$			F	
166: $CH_3CHO + HO_2 \leftrightarrow CH_3CO + H_2O_2$			F	F
171: $C_2H_5OH + OH \leftrightarrow CH_2CH_2OH + H_2O$				F
172: $C_2H_5OH + OH \leftrightarrow CH3CHOH + H_2O$				F
173: $C_2H_5OH + OH \leftrightarrow CH_3CH_2O + H_2O$				F
183: $C_2H_5OH + HO_2 \leftrightarrow CH_3CHOH + H_2O_2$				F
184: $C_2H_5OH + HO_2 \leftrightarrow CH_2CH_2OH + H_2O_2$				R
186: $C_2H_4 + OH \leftrightarrow CH_2CH_2OH$				F
187: $C_2H_5 + HO_2 \leftrightarrow CH_3CH_2O + OH$			F	
188: $CH_3CH_2O + M \leftrightarrow CH_3CHO + H + M$			F	
189: $CH_3CH_2O + M \leftrightarrow CH_3 + CH_2O + M$			F	F
195: $CH_3CHOH + O_2 \leftrightarrow CH_3CHO + HO_2$				F

Net reaction rate and heat releases rate integrated across the entire computational domain for each relevant reaction is shown in Fig. 4.10 for peak temperatures of 2000 K and 1130 K. Elevated pressure increases the rates of third body reactions, making them crucial for combustion at all temperatures. At high temperature the majority of the heat release comes from R6, but at low temperature this has been replaced by R9. Fig. 4.11 shows the same data for peak temperatures of

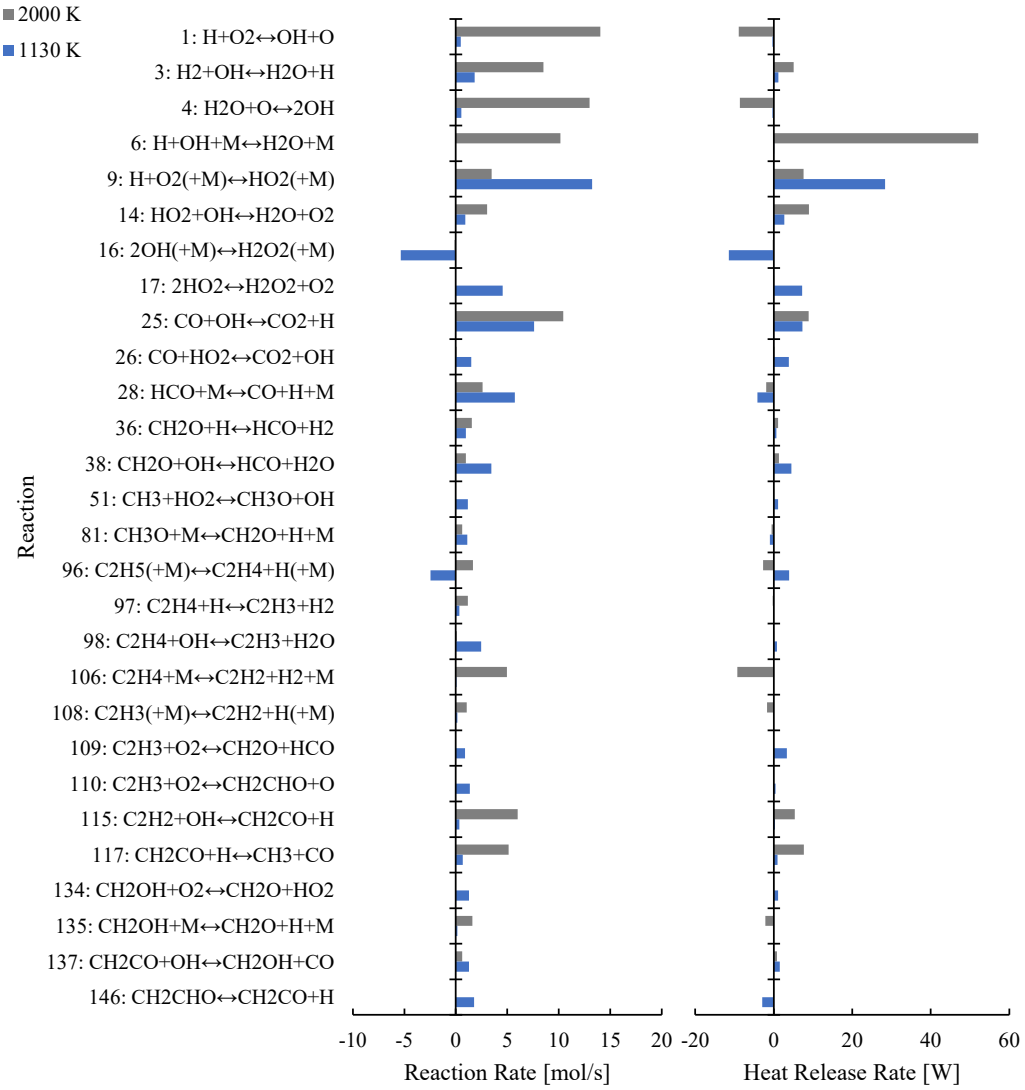

Fig. 4.10. Reaction rates and heat release rates integrated across the entire computational domain at 2000 K and 1130 K.

830 K and 660 K. In the warm flame regime R9, R17, R25, R33, R38, R96, and R109 provide the majority of the heat release. R17, R33, and R38 still have significant heat releases at 660 K, but the others have diminished. Additional heat release is provided by R94.

4.3.6 Reaction Pathways

The reaction pathway for high temperature hot flames is shown in Fig. 4.12. It is very similar to the same condition for the 1 atm case. C_2H_4 mainly reacts with H to form C_2H_3 and then C_2H_2 (R97) or reacts with M to form C_2H_2 directly (R106). C_2H_2

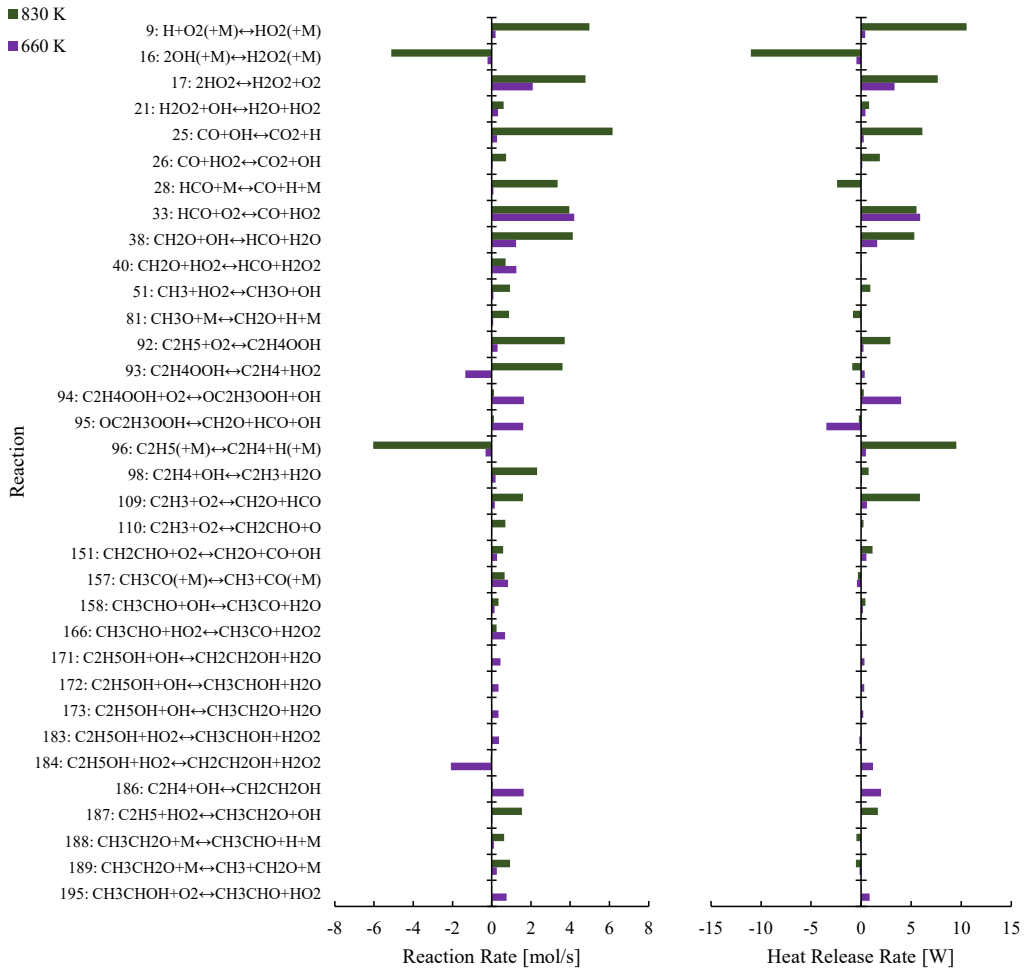

Fig. 4.11. Reaction rates and heat release rates integrated across the entire computational domain at 830 K and 660 K.

reacts with OH to form CH_2CO (R115), which then reacts with OH to form CH_2OH (R137), which reacts with a third body to form CH_2O (R135). The CH_2O reacts with either H (R36) or OH (R38) to form HCO. HCO then reacts with M to form CO (R28), and additional CO is produced through reaction of CH_2CO with H (R117). Finally, the CO reacts with OH to form CO_2 (R25).

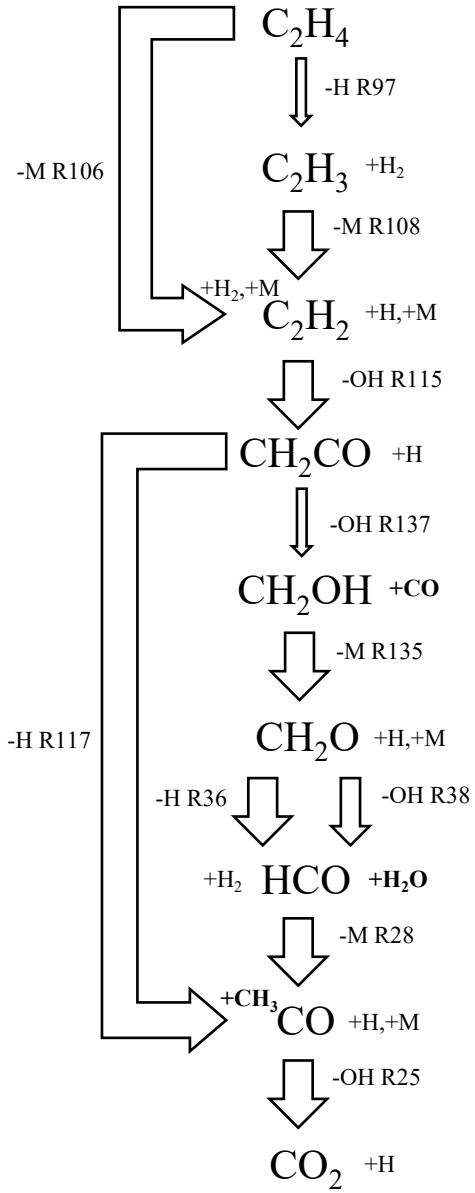

Fig. 4.12. High temperature hot flame reaction pathway.

Fig. 4.13 shows how the reaction pathway changes at 1130 K. Once again, little has changed from the atmospheric pressure case. C_2H_4 reacts with OH to form C_2H_3, which now reacts with O_2 (R110), rather than M, and consequently forms CH_2CHO instead of C_2H_2. CH_2CHO then dissociates to form CH_2CO (R146), which has two paths to reach CH_2O. In the first path, it reacts with H to form CH_3 (R117) which then reacts with HO_2 to form CH_3O (R51), which reacts with M to form CH_2O (R81). In the second path it reacts with OH to form CH_2OH (R137), which reacts

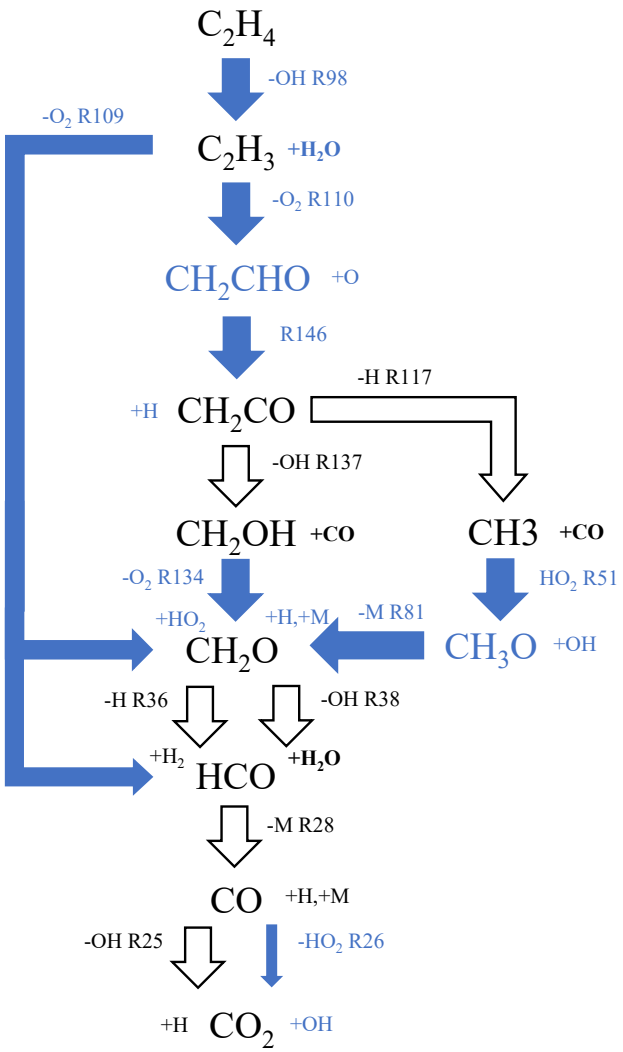

Fig. 4.13. Low temperature hot flame reaction pathway. New reactions and species at 1130 K are indicated in blue.

with O_2 to form CH_2O (R134). Additional CH_2O and HCO are produced through the reaction of C_2H_3 with O_2 (R109). CH_2O conversion to CO_2 proceeds through the same species between high and low temperature hot flames, and there is some additional conversion of CO to CO_2 by reaction with HO_2 (R26).

In the warm flame regime, the oxidation pathway is more varied, as shown in Fig. 4.14, Further increases in reactant leakage and HO_2 levels lead to the emergence of new species and reactions not seen in hot flames. There are two branches that lead to forming CH_2O from C_2H_4. The first branch is nearly identical to the low temperature hot flame regime, except the CH_2CHO now dissociates to form CH_2O and CO (R151), rather than proceeding through CH_2CO.

The second branch starts with C_2H_4 reacting with H to form C_2H_5, which reacts with HO_2 to form CH_3CH_2O or is converted back to C_2H_4 through C_2H_4OOH (R92, R93), resulting in net HO_2 formation. The CH_3CH_2O reacts with M to either form CH_3 and CH_2O (R189), connecting it back to the main branch, or CH_3CHO. The CH_3CHO reacts with OH (R158) or HO_2 (R166) to form CH_3CO, which forms CH_3 through reaction with M, connecting back to the main branch.

CH_2O conversion to CO_2 proceeds through the same species as in hot flames, though new reactions have emerged at low temperature. There is additional CH_2O to HCO formation through HO_2 (R40), and HCO also reacts with O_2 to form CO (R33) alongside R28. Overall CO_2 formation is similar between hot and warm flames.

In the cool flame reaction pathway, shown in Fig. 4.15, there are again two distinct branches. In the first branch, C_2H_4 reacts with HO_2 to form C_2H_4OOH (R93). The C_2H_4OOH reacts with O_2 to form OC_2H_3OOH, which dissociates to form CH_2O

and HCO. The CH_2O forms HCO through R38 and R40, which forms CO through R33, the same as in the warm flame.

The second branch starts with C_2H_4 reacting with OH to form CH_2CH_2OH. This reacts with H_2O_2 to form C_2H_5OH (R184), which reacts with OH (R172) or HO_2 (R183) to form CH_3CHOH, which reacts with O_2 to form CH_3CHO (R166), which produces CH_3CO though reaction with HO_2 (R166), which finally reacts with M to form CO. There is no significant production of CO_2 from CO in the cool flame, making CO the major product of combustion.

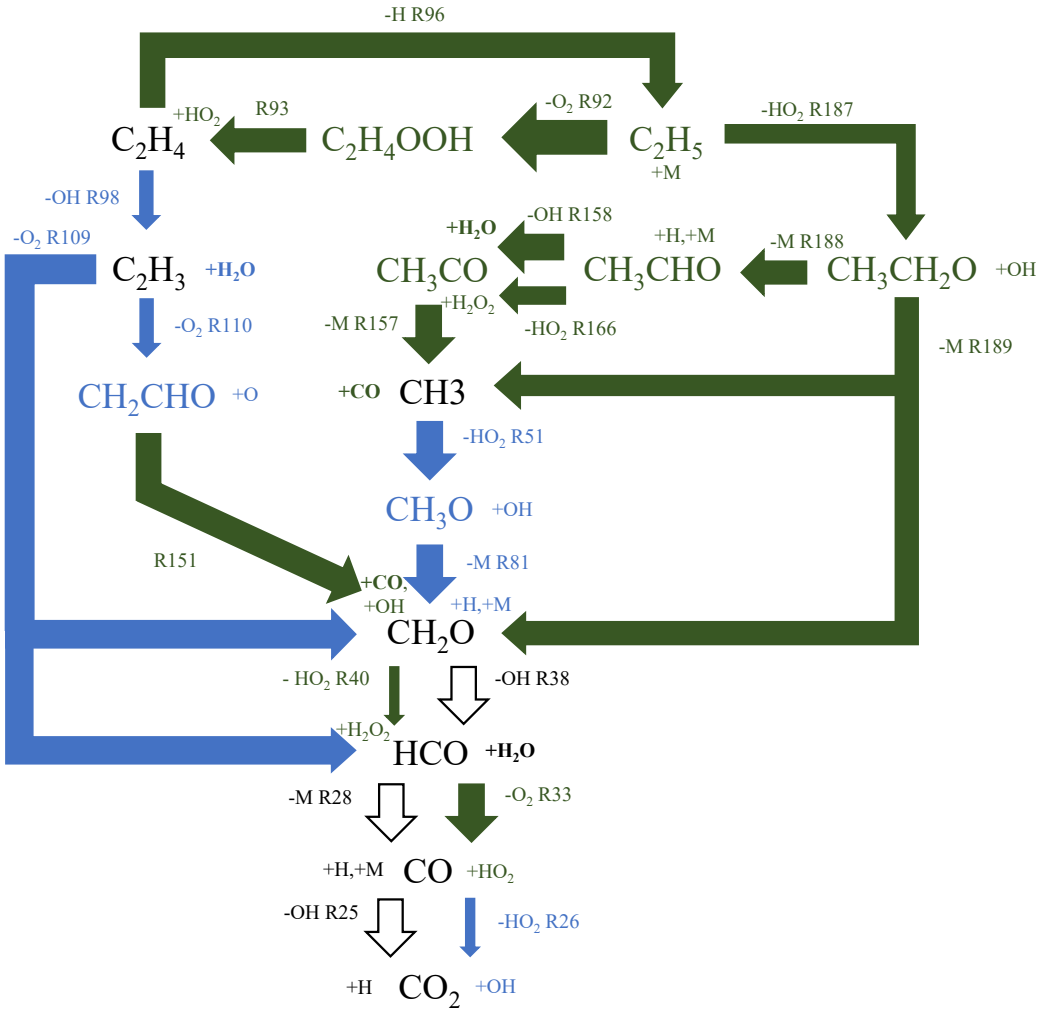

Fig. 4.14. Warm flame reaction pathway. New reactions and species at 1130 K and 830 K are indicated in blue and green, respectively.

One main difference between warm flame and cool flame burning is the direction of R93.

$$C2H4OOH \leftrightarrow C2H4 + HO2 \qquad (R93)$$

In the warm flame regime, the forward reaction dominates, with C_2H_4 being produced from C_2H_5 (R92). As the flame cools and enters the cool flame regime, the reverse reaction dominates.

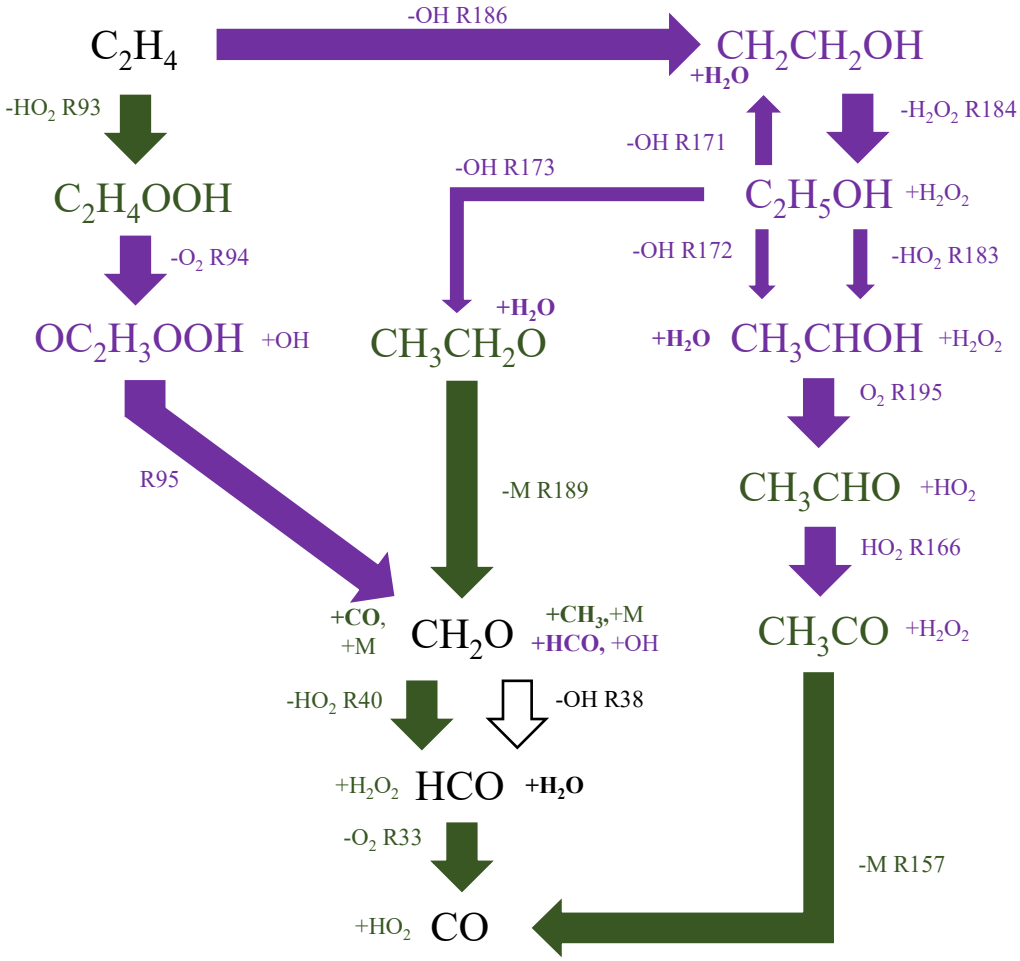

Fig. 4.15. Cool flame reaction pathway. New reactions and species at 1130 K, 830 K. and 660 K are indicated in blue, green, and purple, respectively.

4.4 Summary

In summary, decreasing temperatures leads to decreased reactant consumption and more leakage. The chemistry that sustains the flame at high temperature is no longer feasible as temperature drops, and new reactions emerge to provide the necessary heat release. While in a 1 atm flame these reactions cannot sustain the flame below 1130 K, this is possible in a 50 atm flame due to increased third body reactions that elevate HO_2 levels in the system. HO_2 becomes the dominant radical and participates in most of the chemistry that supports the flame throughout the warm flame region. As the flame extinguishes, cool flame chemistry kicks in to sustain the flame at a lower temperature, and conversion from CO_2 to CO ceases, making CO the main product. The lack of sufficient radiation to drop the temperature means flame temperature increases in the cool flame regime, until eventually a hot flame ignites again.

These results depend on the accuracy of the UCSD mechanism, for which the low temperature chemistry was validated using experimental ignition delay times from a rapid compression machine [49]. The mechanism was not specifically validated for C_2H_4 owing to a lack of experimental results, nor was it validated for diffusion flames. It was also unable to recreate the cool flame burning observed in [7] for butane without the pressure being increased to 50 atm, as opposed to 2 atm in the experiments. Other mechanisms faced similar challenges. This indicates a need for more experimental data to validate these mechanisms, especially for diffusion flames. The next chapter discusses a method to consistently produce cool diffusion flames

using a simple, inexpensive setup, with the aim of increasing access to cool flame research.

Chapter 5 Cool Diffusion Flames Above a Liquid Pool

5.1 Introduction

Despite recent advances in renewable energy, the world is still highly dependent on fossil fuel combustion for energy production. The need for cleaner and more efficient engines is imperative. Advances in internal combustion engine processes could help meet this need. Recently, low-emission engine technologies such as homogeneous charge compression ignition (HCCI), premixed charge compression ignition (PCCI), and reactivity controlled compression ignition (RCCI) have been pursued. In these engines, autoignition via cool flames is an integral part of the combustion process [25,26,21,19], but this process is not sufficiently understood. The thermal efficiency of current internal-combustion engines, typically 38%, could be increased to 60% with future ultra-lean and low-temperature engines that exploit cool flames [13].

Premixed cool flames were first observed in the early 19th century [14]. Their understanding has since evolved alongside advances in experimental and numerical techniques. Cool flames have peak temperatures of 500 – 1000 K and increase the local gas temperature on the order of 100 K [13]. They consume just a fraction of the reactants, and produce formaldehyde [16,17].

The existence of cool diffusion flames (CDFs) had been predicted by Cuoci, et. al [53], but they were not observed until 2012, in droplet experiments aboard the International Space Station (ISS) [54]. The two-stage burning that was observed on the ISS was numerically confirmed to be associated with CDFs [55].

This discovery of CDFs has led to a surge of interest in cool flame research. CDFs have been observed in microgravity with droplets of various fuels [56–59] and with a spherical porous burner [7]. They have also been observed in normal gravity counterflow flames [60–64]. Unfortunately, the spherical CDFs require costly long-duration microgravity, and past work in counterflow CDFs has involved cool flame enhancers (ozone addition, plasmas, or enriched oxygen), which perturb the fundamental chemistry.

Many of these studies used *n*-heptane as a fuel. Stable CDFs are favored when the fuel is a large alkane or an ether. Due to the low reaction rates they also require long residence times, which can be achieved using stagnation flow [60,65]. Temperatures must be elevated to slightly below the negative-temperature coefficient region, increasing the radical pool in the flame and helping the radical-deprived CDF autoignite [66]. Most CDFs stabilize on the rich side [56–59,7,61,62,64].

Modeled temperatures of CDFs are far more prevalent than measured. Won et al. [60] measured and predicted *n*-heptane CDF peak temperatures of 640 and 828 K in counterflow CDFs. The temperatures predicted for droplets have been lower: Seshadri et al. [67] predicted a cool flame crossover temperature of 770 K and Farouk et al. [55] predicted a cool flame temperature of 700 K.

A common theme of past observations of CDFs is that the burners or facilities used are available to only a limited number of researchers worldwide. This inhibits the potential for widespread research on CDFs. This study seeks to develop an inexpensive experimental setup for observing CDFs.

5.2 Experimental

The burner apparatus is illustrated in Fig. 5.1. The fuel is *n*-heptane, which has a molar mass of 100.2 g/mol, a boiling point of 372 K, and a flash point of 269 K [68]. This is contained in a PYREX borosilicate glass beaker with a capacity of 30 mL and an inner diameter of 32 mm. The beaker is placed on the lower heater, a flat cast iron heater with a diameter of 188 mm (Cusimax model CMHP-B101, 1.5 kW at 110 VAC). A second Cusimax heater (the upper heater) is inverted and mounted above the annular disk. The heater excitations (11 – 110 VAC) were controlled with external variable transformers. The lower heater is primarily used to heat the liquid *n*-heptane, while the upper heater is primarily used to heat the gas above the pool.

An annular aluminum disk, with a thickness of 3.3 mm, an inner diameter of 32 mm, and an outer diameter of 146 mm, is secured to the top of the beaker. The annular disk helps stabilize the CDFs, in regions with good optical access, by reducing unsteady flows near the reaction zone. It also provides uniform temperatures and long residence times near the reaction zone and allows more independent

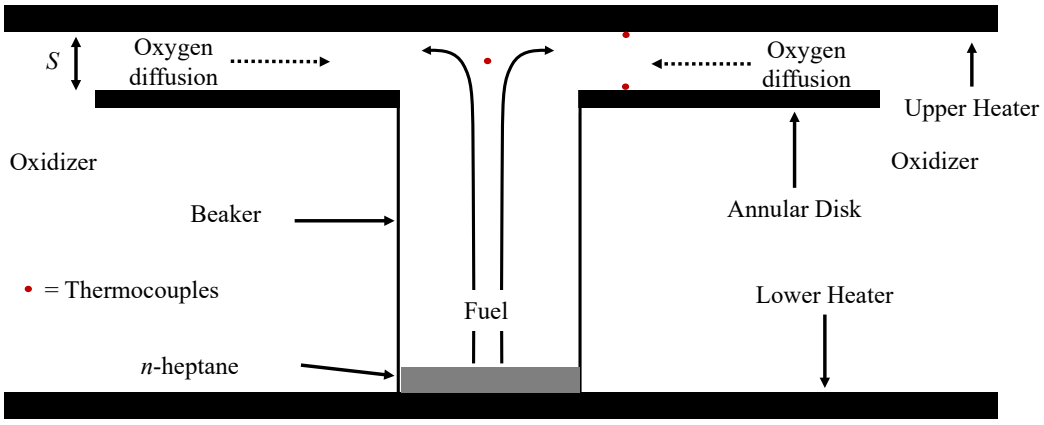

Fig. 5.1. Schematic of the burner apparatus showing approximate streamlines.

temperature control with the two heaters. The separation distance, *S*, between the annular disk and the upper heater varied from 1 – 15 mm.

The burner apparatus was installed in a rectangular hood with a footprint of 100 × 100 cm, a height of 60 cm, the front face open, and a vent flow rate of 2400 LPM. All the tests were in air at 1 atm.

The CDFs burned above the opening in the annular disk. Fuel vapor arrived at the reaction zone mainly by convection, as shown by streamlines in Fig. 1, while the oxidizer arrived mainly by diffusion. CDFs have extensive fuel and oxidizer leakage across the reaction zone. Although the gas was stably stratified above the annular disk, recirculation zones there are likely at such low bulk flow velocities.

Images were recorded with a Nikon D5300 digital color camera with a Nikkor 50 mm lens. Because the CDFs were dim, and barely visible to the naked eye, the *f*/# was 1.4, the ISO was 12,800, and the exposure time was 1 s. A Xybion ISG-750 intensified video camera was also used for real-time visual observations of the CDFs at 30 frames/s.

Temperatures were measured using three 250 μm diameter type K (nickel/chromium/alumel) uncoated bare-wire thermocouples. Two were in fixed locations in contact with the upper heater and disk at a radius of 20 mm. The third was in and near the CDFs, and for some tests it was translated radially or vertically. Because the thermocouple readings were low, and relatively close to the temperatures of the heater and disk, no radiation corrections were made. The uncertainty in measured temperatures is estimated at ± 5 K.

The *n*-heptane evaporation rates were measured gravimetrically, with an estimated uncertainty of ± 10%. Formaldehyde concentrations at the entrance to the exhaust vent were measured with a Temtop LKC-1000E formaldehyde sensor, with an estimated uncertainty of ± 1 ppm.

Each measurement was performed several times to confirm repeatability. The uncertainties stated herein consider both the measurement variance and estimates of bias.

5.3 Results

5.3.1 Flame Appearance and Formaldehyde Yields

With the heaters, beaker, and disk in thermal equilibrium, and the desired *S* established, the beaker and disk were removed and quickly returned after 1 mL of *n*-heptane was added to the beaker. For *S* between 5 – 10 mm, a CDF autoignited after 2 – 5 s and burned continuously until the fuel was depleted. The CDFs were nearly steady, but there was occasional flame motion. Continuously burning CDFs were not observed for *S* outside this range. Instead, the CDFs would fluctuate, extinguish, and reignite. For CDFs the pool temperature was maintained near 343 K to avoid fuel flow rates that were too low or too high for stable CDFs.

Fig. 5.2 shows representative images of three CDFs for various *S*. These flames were blue (because of excited formaldehyde) and so dim they could only be seen in a darkened laboratory. The CDF shapes varied with *S*. For $S = 5$ mm (see Fig. 5.2) the CDF was nearly flat with slight upward concavity. Its main reaction zone extended from the beaker centerline to nearly the disk walls. For $S = 7.5$ mm, the flame base was at the height of the annular disk and at a radius of 6.5 mm. The main reaction

zone curved upward and outward. For S = 10 mm, the brightest part of the CDF was much wider. At this S the CDFs were less steady. Stable CDFs were not observed for S below 5 mm or above 10 mm.

Autoignition to hot flames was not observed for any of these flames unless the upper heater was hotter than 800 K or an external butane flame was introduced. For S < 10 mm, the hot flame flashed briefly before being replaced by a CDF. For S between 10 – 12.5 mm, a blue hot flame burned for a few seconds but then extinguished and was replaced by a CDF. For S > 12.5 mm, a yellow, sooting hot flame appeared and burned until the fuel was depleted. It is noteworthy that only CDFs (i.e., not hot flames) burned continuously for S < 12.5 mm. For these

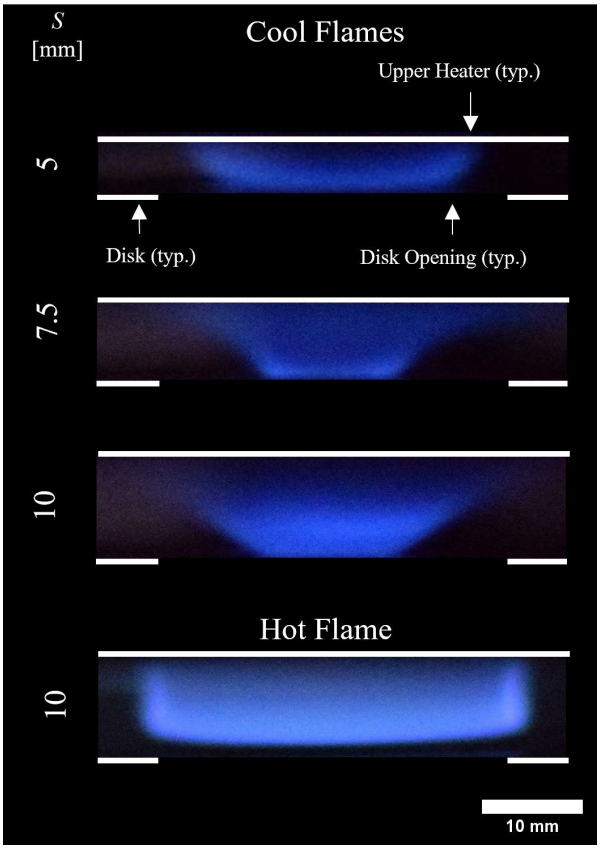

Fig. 5.2. Color images of representative n-heptane flames. The exposure times were 1 s and 10 ms for the cool and hot flames, respectively.

conditions the hot flames were quenched by the upper heater surfaces, whereas these surfaces have temperatures closer to the peak CDF temperatures.

A representative hot flame image is shown in Fig. 5.2. The hot flames were visible under normal ambient lighting and were about 140 times as luminous as the CDFs.

The measured *n*-heptane evaporation rates were 1.1 and 2.2 mg/s for CDFs and hot flames, respectively, and these were independent of *S* for the CDFs. Based on this, the gas velocities in the beaker (assuming *n*-heptane vapor at 600 K) were 0.65 and 1.3 mm/s for the CDFs and the hot flames, respectively. The increased evaporation rates for the hot flames resulted from heat feedback from the flame to the pool.

When CDFs were present, the measured formaldehyde concentration in the vent line was 2 ppm. Considering the vent flow rate and the *n*-heptane evaporation rate, and assuming all products are well mixed at the vent entrance, this corresponds to a formaldehyde yield of 0.1 g/g-fuel. The hot flames did not produce a detectable level (0.01 ppm or higher) of formaldehyde.

5.3.2 Temperatures

For some tests the thermocouple was translated vertically along the burner axis. Results for representative tests are shown in Fig. 5.3a. The temperature between the upper heater and the disk opening varied by 60 and 30 K for the no-fuel and CDF cases, respectively. The same power was supplied to the upper heater in both cases. Extrapolating these curves to the upper heater indicates its temperature on the axis was 640 and 710 K for the no-fuel and CDF cases, respectively.

For some tests the thermocouple was translated radially at the mid-plane between the disk and the upper heater. The results for the two cases in Fig. 5.3a are shown in Fig. 5.3b. This CDF had a peak temperature of 700 K (as determined from the mean

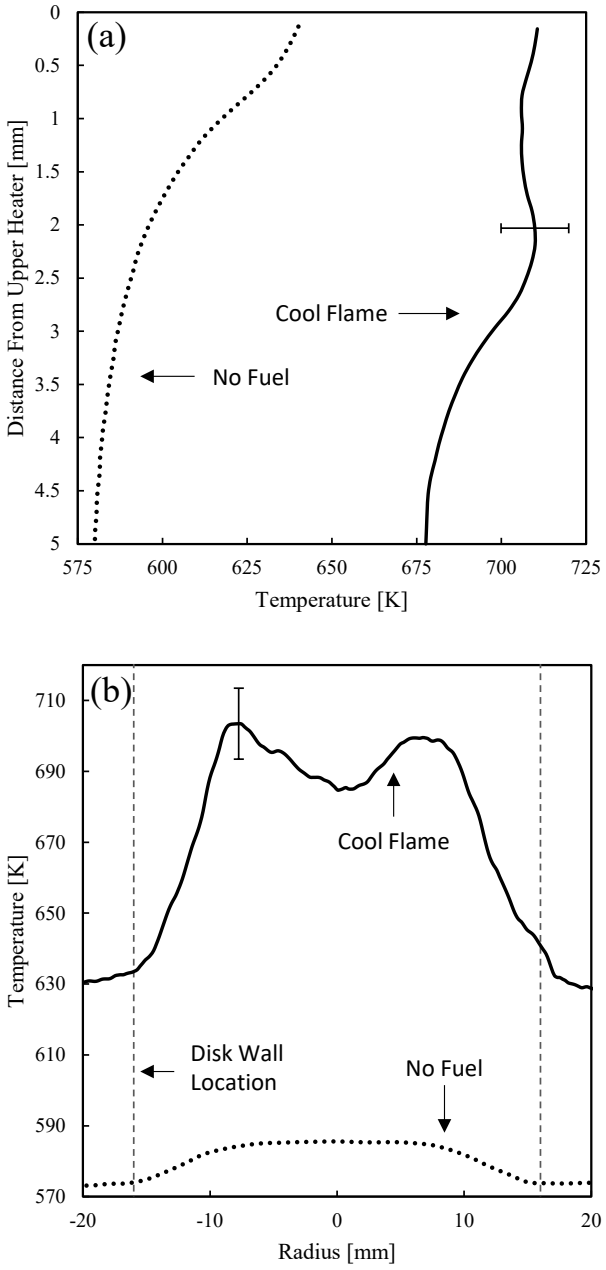

Fig. 5.3. (a) Gas temperatures on the burner axis versus distance from the upper heater for S = 5 mm. (b) Gas temperatures versus radius with S = 5 mm and with the thermocouple 2.5 mm below the upper heater.

of the left and right peaks in Fig. 5.3b). This behavior is unlike that for the hot flames, whose temperatures exceeded the thermocouple limit of 1533 K.

Fig. 5.4 shows the measured peak CDF temperatures plotted with respect to *S*. For these tests the same power was supplied to the upper heater as in Fig. 5.3. The temperatures in Fig. 5.4 increase linearly with increasing *S*. This behavior could result from variations in CDF equivalence ratios and/or heat losses via conduction to the metal surfaces or radiation. Increasing *S* is expected to decrease the equivalence ratio near the CDF by increasing the area available for oxygen to diffuse upstream. Zhao et al. [66] predicted that premixed cool flame temperatures increase with increasing equivalence ratio, but the measurements of Hajilou et al. [69] and Brown et al. [70] in premixed flames indicate the opposite.

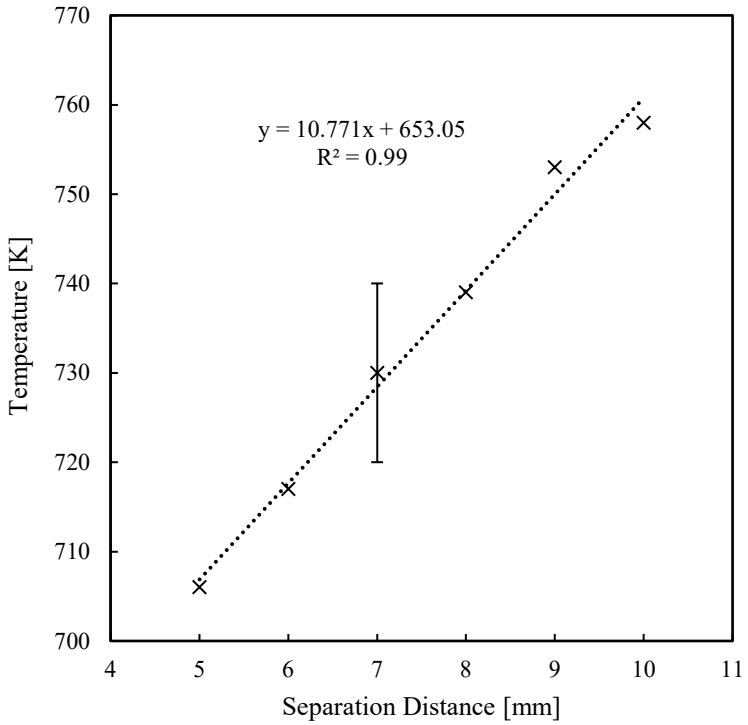

Fig. 5.4. Peak temperatures of the CDFs as a function of S. The thermocouple was 0.5 mm below the upper heater and at the radius of maximum temperature.

To observe the ignition and extinction of these CDFs, the temperature of the upper heater was ramped up and then down for some tests. This was performed both with and without fuel in the beaker. The upper heater and disk had the same temperatures whether not fuel (and a CDF) were present at fixed heater power. These CDFs were at times unsteady or extinguished, and thus were observed with the intensified video camera.

The resulting temperatures for a representative test are shown in Fig. 5.5. When no fuel was present, the gas temperature ramped up to 610 K and then decreased. When fuel was present, exothermic cool flame reactions commenced when the gas temperature first reached 560 K, and the gas temperature quickly increased by about 100 K upon ignition. The initial CDF was weak, and sharp oscillations in CDF

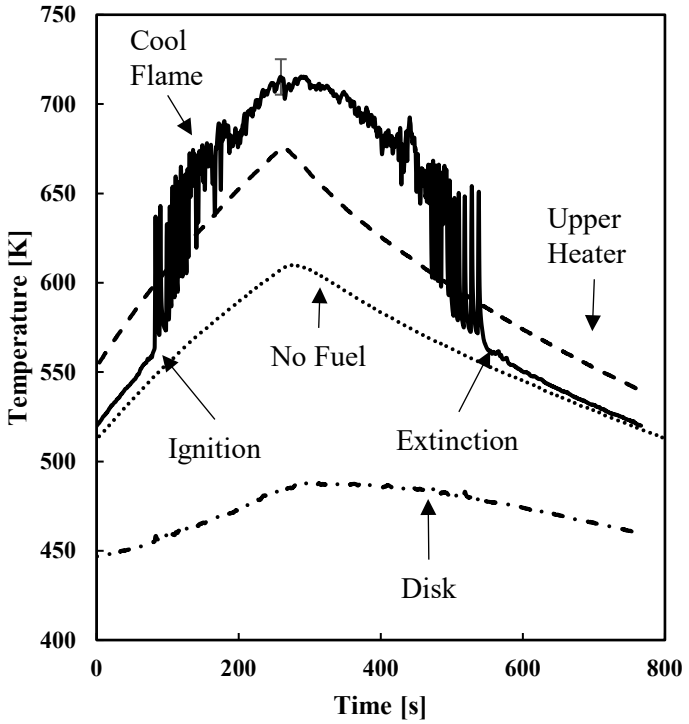

Fig. 5.5. Gas, heater, and disk temperatures versus time for S = 5 mm. The gas temperatures were measured 2.5 mm from the upper heater and at a radius of 8 mm. The heater and disk temperatures were measured at a radius of 20 mm.

temperature are seen in Fig. 5.5. As the heater temperature increased, the CDF strengthened and reached a peak temperature of 710 K. Then, as the heater cooled, the CDF cooled, then fluctuated in position with occasional extinction and re-ignition events, as evidenced by sharp 60 K swings in gas temperature. The gas temperature fluctuations after ignition and before extinction could not be eliminated with slower temperature ramping. When the gas temperature dropped below 560 K, the CDF extinguished and did not reignite. This test, and similar tests at other *S*, indicate that these CDFs ignited and extinguished at 550 ± 20 K, and that their peak temperatures increased with increasing temperature of the upper heater.

The measured CDF temperatures of Figs. 5.3 – 5.5 are among the first for *n*-heptane CDFs. The measured peak temperatures are in a similar range to those of past measurements and predictions [55,60,67]. These measurements provide support for past statements that cool flames increase the local gas temperature on the order of 100 K [5,17]. In Fig. 5.3b the peak CDF temperature is 70 K above the temperature of the surrounding air, while in Fig. 5.5 the initial ignition of a CDF increases the peak temperature by 80 K.

5.4 Summary

Cool diffusion flames were observed burning *n*-heptane in a stably-stratified stagnation flow. The flames burned between parallel plates with various separation distances. The measurements included flame imaging, gas temperatures, evaporation rates, and formaldehyde emissions. The main conclusions are as follows.

1. This configuration using a stably-stratified stagnation flow is an inexpensive alternative to most past experiments of CDFs. For separation distances of 5 – 10 mm, the CDFs burned until the fuel was depleted.
2. The peak temperatures of the CDFs were between 705 – 760 K, increased with increasing separation distance, and were 70 K above the temperature of the surrounding air. The CDFs autoignited at a temperature of 550 K.
3. The *n*-heptane evaporation rate was 1.1 mg/s, and the formaldehyde yield was 0.1 g/g-fuel.
4. Hot flames were also observed using the same apparatus. These had much higher temperatures, 140 times the luminosity, twice the *n*-heptane evaporation rate, and no formaldehyde emissions. For a separation distance below 12.5 mm, any hot flames extinguished and were replaced by CDFs.

This new approach to generating CDFs, being something that can be easily accomplished in any lab without cool flame enhancers such as ozone, plasmas, or enriched oxygen, should be valuable for future studies of CDFs.

Chapter 6 Conclusions and Future Directions

6.1 Spherical Diffusion Flames

6.1.1 Conclusions

Microgravity spherical diffusion flames were studied over a wide range of experimental conditions. Blackbody calibration data was successfully correlated to temperature for the ACME camera, and thin filament pyrometry (TFP) was used to measure flame temperatures. A transient numerical model was used to simulate experimental conditions. Flame temperature and radius measurements agreed well with numerical predictions. The behavior of the spherical porous burner was studied, and it was determined that there is minimal heating of the gas that passes through the porous sphere, especially at high flow rates.

The numerical model was used to elucidate the kinetics of ethylene microgravity spherical diffusion flames at atmospheric and elevated pressures. As temperature decreased, increased reactant leakage led to the emergence of new reaction pathways. HO_2 played a large part in the low temperature chemistry of these flames. At atmospheric pressure, warm flame chemistry is not strong enough to sustain the flame below its extinction point of 1130 K. Elevated pressures were found to promote HO_2 formation, which led to increased warm and cool flame behavior. At 50 atm the flame was able to extend its burn time by over 500 s due to the emergence of warm flame chemistry. Once the flame extinguished it stabilized to a cool flame, at which point the temperature increased towards hot flame ignition.

6.1.2 Future Directions

With regards to TFP, the focus so far has been on peak temperature vs. time, but one of the benefits of TFP is that it provides spatial data as well. In some tests the flame is large enough to cause multiple fibers to glow, meaning temperatures at various locations along the flame can be compared. Preliminary results indicate that the flame is hottest at the north pole, and temperature drops as you move along the flame.

Another aspect of these flames to be further analyzed is their sooting behavior. With the TFP measurements calibrated, the temperature at which visible soot dissipates can be determined. This can be related to the level of dilution in the flames, with the idea that higher reactant dilution leads to soot dissipation at higher temperatures.

6.2 Cool Pool Diffusion Flames

6.1.1 Conclusions

A new method was developed for producing cool diffusion flames (CDFs) in normal gravity. CDFs were observed above pools of n-heptane using an inexpensive parallel heater setup. The flames burned steadily for as long as fuel was present. The peak temperatures of the CDFs were between 705 – 760 K, increased with increasing separation distance, and were 70 K above the temperature of the surrounding air. The CDFs autoignited at a temperature of 550 K. Conditions were observed where hot flames would not ignite, but CDFs would.

6.2.2 Future Directions

These results provide a solid basis for future studies using this setup. Other fuels can be tested for cool flame behavior. Future work will seek to observe warm flames in this setup and produce CDFs that are self-sustaining. The success of these experiments shows it is possible to produce CDFs without special equipment or additives. The setup described here will provide access to cool flame research to the average researcher and generate more experimental targets for model validation, which is beneficial for advanced engine development.

Appendix A The UCSD Mechanism

The UCSD mechanism is a simplified chemical kinetics mechanism developed by researchers at the University of California at San Diego It incorporates 57 species and 270 reaction steps, and is valid for $C_1 - C_4$ hydrocarbons [45,49,52]. The elements considered are C, H, O, N, He, and Ar, and the species are listed in Table A.1. The reactions are listed in Table A.2.

Table A.1. Species considered in the UCSD mechanism.

N2	AR	HE	H	O2
OH	O	H2	H2O	HO2
H2O2	CO	CO2	HCO	CH3
CH4	CH2O	T-CH2	S-CH2	C2H4
CH3O	C2H5	C2H6	CH	C2H2
C2H4OOH	OC2H3OOH	C2H3	CH2CHO	C2H4O
HCCO	CH2CO	C2H	CH2OH	CH3OH
CH3CHO	CH3CO	C2H5OH	CH2CH2OH	CH3CHOH
CH3CH2O	C3H4	C3H3	C3H5	C3H6
C3H8	I-C3H7	N-C3H7	C3H6OOH	OC3H5OOH
C4H10	PC4H9	SC4H9	C4H8	SC4H9O2
C4H8OOH1-3	NC4KET13	CHCHO		

Table A.2. List of reactions in the UCSD mechanism

Number	Reaction	A	n	E
1	H+O2↔OH+O	3.52E+16	-0.7	17069.79
2	H2+O↔OH+H	5.06E+04	2.67	6290.63
3	H2+OH↔H2O+H	1.17E+09	1.3	3635.28
4	H2O+O↔2OH	7.00E+05	2.33	14548.28
5	2H+M↔H2+M	1.30E+18	-1	0
6	H+OH+M↔H2O+M	4.00E+22	-2	0
7	2O+M↔O2+M	6.17E+15	-0.5	0
8	H+O+M↔OH+M	4.71E+18	-1	0
9	H+O2(+M)↔HO2(+M)	4.65E+12	0.44	0
10	HO2+H↔2OH	7.08E+13	0	294.93
11	HO2+H↔H2+O2	1.66E+13	0	822.9
12	HO2+H↔H2O+O	3.10E+13	0	1720.84
13	HO2+O↔OH+O2	2.00E+13	0	0

Number	Reaction	A	n	E
14	HO2+OH↔H2O+O2	7.00E+12	0	-1094.65
15	HO2+OH↔H2O+O2	4.50E+14	0	10929.73
16	2OH(+M)↔H2O2(+M)	9.55E+13	-0.27	0
17	2HO2↔H2O2+O2	1.03E+14	0	11042.07
18	2HO2↔H2O2+O2	1.94E+11	0	-1408.94
19	H2O2+H↔HO2+H2	2.30E+13	0	7950.05
20	H2O2+H↔H2O+OH	1.00E+13	0	3585.09
21	H2O2+OH↔H2O+HO2	1.74E+12	0	1434.03
22	H2O2+OH↔H2O+HO2	7.59E+13	0	7272.94
23	H2O2+O↔HO2+OH	9.63E+06	2	3991.4
24	CO+O(+M)↔CO2(+M)	1.80E+11	0	2384.08
25	CO+OH↔CO2+H	4.40E+06	1.5	-740.92
26	CO+HO2↔CO2+OH	2.00E+13	0	22944.55
27	CO+O2↔CO2+O	1.00E+12	0	47700.05
28	HCO+M↔CO+H+M	1.86E+17	-1	17000.48
29	HCO+H↔CO+H2	5.00E+13	0	0
30	HCO+O↔CO+OH	3.00E+13	0	0
31	HCO+O↔CO2+H	3.00E+13	0	0
32	HCO+OH↔CO+H2O	3.00E+13	0	0
33	HCO+O2↔CO+HO2	7.58E+12	0	409.89
34	HCO+CH3↔CO+CH4	5.00E+13	0	0
35	H+HCO(+M)↔CH2O(+M)	1.09E+12	0.48	-260.04
36	CH2O+H↔HCO+H2	5.74E+07	1.9	2748.57
37	CH2O+O↔HCO+OH	3.50E+13	0	3513.38
38	CH2O+OH↔HCO+H2O	3.90E+10	0.89	406.31
39	CH2O+O2↔HCO+HO2	6.00E+13	0	40674
40	CH2O+HO2↔HCO+H2O2	4.11E+04	2.5	10210.33
41	CH4+H↔H2+CH3	1.30E+04	3	8037.76
42	CH4+OH↔H2O+CH3	1.60E+07	1.83	2782.03
43	CH4+O↔CH3+OH	1.90E+09	1.44	8675.91
44	CH4+O2↔CH3+HO2	3.98E+13	0	56890.54
45	CH4+HO2↔CH3+H2O2	9.03E+12	0	24641.49
46	CH3+H↔T-CH2+H2	1.80E+14	0	15105.16
47	CH3+H↔S-CH2+H2	1.55E+14	0	13479.92
48	CH3+OH↔S-CH2+H2O	4.00E+13	0	2502.39
49	CH3+O↔CH2O+H	8.43E+13	0	0
50	CH3+T-CH2↔C2H4+H	4.22E+13	0	0
51	CH3+HO2↔CH3O+OH	5.00E+12	0	0
52	CH3+O2↔CH2O+OH	3.30E+11	0	8941.2
53	CH3+O2↔CH3O+O	1.10E+13	0	27820.03
54	2CH3↔C2H4+H2	1.00E+14	0	32002.87

Number	Reaction	A	n	E
55	2CH3↔C2H5+H	3.16E+13	0	14698.85
56	H+CH3(+M)↔CH4(+M)	1.35E+14	0.091	87.721
57	2CH3(+M)↔C2H6(+M)	1.81E+13	0	0
58	S-CH2+OH↔CH2O+H	3.00E+13	0	0
59	S-CH2+O2↔CO+OH+H	3.13E+13	0	0
60	S-CH2+CO2↔CO+CH2O	3.00E+12	0	0
61	S-CH2+M↔T-CH2+M	6.00E+12	0	0
62	T-CH2+H↔CH+H2	6.02E+12	0	-1787.76
63	T-CH2+OH↔CH2O+H	2.50E+13	0	0
64	T-CH2+OH↔CH+H2O	1.13E+07	2	2999.52
65	T-CH2+O↔CO+2H	8.00E+13	0	0
66	T-CH2+O↔CO+H2	4.00E+13	0	0
67	T-CH2+O2↔CO2+H2	2.63E+12	0	1491.4
68	T-CH2+O2↔CO+OH+H	6.58E+12	0	1491.4
69	2T-CH2↔C2H2+2H	1.00E+14	0	0
70	C2H2+HO2↔CHCHO+OH	1.60E+08	1.36	15420
71	CHCHO+O2=CH2O+CO+O	1.30E+06	2.4202	1604
72	CH+O↔CO+H	4.00E+13	0	0
73	CH+O2↔HCO+O	1.77E+11	0.76	-478.01
74	CH+H2O↔CH2O+H	1.17E+15	-0.75	0
75	CH+CO2↔HCO+CO	4.80E+01	3.22	-3226.58
76	CH3O+H↔CH2O+H2	2.00E+13	0	0
77	CH3O+H↔S-CH2+H2O	1.60E+13	0	0
78	CH3O+OH↔CH2O+H2O	5.00E+12	0	0
79	CH3O+O↔OH+CH2O	1.00E+13	0	0
80	CH3O+O2↔CH2O+HO2	4.28E-13	7.6	-3537.28
81	CH3O+M↔CH2O+H+M	7.78E+13	0	13513.38
82	C2H6+H↔C2H5+H2	5.40E+02	3.5	5210.33
83	C2H6+O↔C2H5+OH	1.40E+00	4.3	2772.47
84	C2H6+OH↔C2H5+H2O	2.20E+07	1.9	1123.33
85	C2H6+CH3↔C2H5+CH4	5.50E-01	4	8293.5
86	C2H6(+M)↔C2H5+H(+M)	8.85E+20	-1.23	102222.8
87	C2H6+HO2↔C2H5+H2O2	1.32E+13	0	20469.89
88	C2H5+H↔C2H4+H2	3.00E+13	0	0
89	C2H5+O↔C2H4+OH	3.06E+13	0	0
90	C2H5+O↔CH3+CH2O	4.24E+13	0	0
91	C2H5+O2↔C2H4+HO2	7.50E+14	-1	4799.95
92	C2H5+O2↔C2H4OOH	2.00E+12	0	0
93	C2H4OOH↔C2H4+HO2	4.00E+34	-7.2	23000
94	C2H4OOH+O2↔OC2H3OOH+OH	7.50E+05	1.3	-5799.95
95	OC2H3OOH↔CH2O+HCO+OH	1.00E+15	0	43000

Number	Reaction	A	n	E
96	C2H5(+M)↔C2H4+H(+M)	1.11E+10	1.037	36768.64
97	C2H4+H↔C2H3+H2	4.49E+07	2.12	13360.42
98	C2H4+OH↔C2H3+H2O	5.53E+05	2.31	2963.67
99	C2H4+O↔CH3+HCO	2.25E+06	2.08	0
100	C2H4+O↔CH2CHO+H	1.21E+06	2.08	0
101	2C2H4↔C2H3+C2H5	5.01E+14	0	64700.05
102	C2H4+O2↔C2H3+HO2	4.22E+13	0	57623.09
103	C2H4+HO2↔C2H4O+OH	2.23E+12	0	17189.29
104	C2H4O+HO2↔CH3+CO+H2O2	4.00E+12	0	17007.65
105	C2H4+M↔C2H3+H+M	2.60E+17	0	96568.12
106	C2H4+M↔C2H2+H2+M	3.50E+16	0	71532.03
107	C2H3+H↔C2H2+H2	4.00E+13	0	0
108	C2H3(+M)↔C2H2+H(+M)	6.38E+09	1	37626.67
109	C2H3+O2↔CH2O+HCO	1.70E+29	-5.312	6503.11
110	C2H3+O2↔CH2CHO+O	7.00E+14	-0.611	5262.43
111	C2H3+O2↔C2H2+HO2	5.19E+15	-1.26	3312.62
112	C2H2+O↔HCCO+H	4.00E+14	0	10659.66
113	C2H2+O↔T-CH2+CO	1.60E+14	0	9894.84
114	C2H2+O2↔CH2O+CO	4.60E+15	-0.54	44933.08
115	C2H2+OH↔CH2CO+H	1.90E+07	1.7	999.04
116	C2H2+OH↔C2H+H2O	3.37E+07	2	14000.96
117	CH2CO+H↔CH3+CO	1.50E+09	1.43	2688.81
118	CH2CO+O↔T-CH2+CO2	2.00E+13	0	2294.46
119	CH2CO+O↔HCCO+OH	1.00E+13	0	2000.48
120	CH2CO+CH3↔C2H5+CO	9.00E+10	0	0
121	HCCO+H↔S-CH2+CO	1.50E+14	0	0
122	HCCO+OH↔HCO+CO+H	2.00E+12	0	0
123	HCCO+O↔2CO+H	9.64E+13	0	0
124	HCCO+O2↔2CO+OH	2.88E+07	1.7	1001.43
125	HCCO+O2↔CO2+CO+H	1.40E+07	1.7	1001.43
126	C2H+OH↔HCCO+H	2.00E+13	0	0
127	C2H+O↔CO+CH	1.02E+13	0	0
128	C2H+O2↔HCCO+O	6.02E+11	0	0
129	C2H+O2↔CH+CO2	4.50E+15	0	25095.6
130	C2H+O2↔HCO+CO	2.41E+12	0	0
131	CH2OH+H↔CH2O+H2	3.00E+13	0	0
132	CH2OH+H↔CH3+OH	2.50E+17	-0.93	5126.91
133	CH2OH+OH↔CH2O+H2O	2.40E+13	0	0
134	CH2OH+O2↔CH2O+HO2	5.00E+12	0	0
135	CH2OH+M↔CH2O+H+M	5.00E+13	0	25119.5
136	CH3O+M↔CH2OH+M	1.00E+14	0	19120.46

Number	Reaction	A	n	E
137	CH2CO+OH↔CH2OH+CO	1.02E+13	0	0
138	CH3OH+OH↔CH2OH+H2O	1.44E+06	2	-838.91
139	CH3OH+OH↔CH3O+H2O	4.40E+06	2	1505.74
140	CH3OH+H↔CH2OH+H2	1.35E+03	3.2	3490.68
141	CH3OH+H↔CH3O+H2	6.83E+01	3.4	7239.96
142	CH3OH+O↔CH2OH+OH	3.88E+05	2.5	3080.78
143	CH3OH+HO2↔CH2OH+H2O2	8.00E+13	0	19383.37
144	CH3OH+O2↔CH2OH+HO2	2.00E+13	0	44933.08
145	CH3OH(+M)↔CH3+OH(+M)	1.90E+16	0	91729.92
146	CH2CHO↔CH2CO+H	1.05E+37	-7.189	44340.34
147	CH2CHO+H↔CH3+HCO	5.00E+13	0	0
148	CH2CHO+H↔CH2CO+H2	2.00E+13	0	0
149	CH2CHO+O↔CH2O+HCO	1.00E+14	0	0
150	CH2CHO+OH↔CH2CO+H2O	3.00E+13	0	0
151	CH2CHO+O2↔CH2O+CO+OH	3.00E+10	0	0
152	CH2CHO+CH3↔C2H5+CO+H	4.90E+14	-0.5	0
153	CH2CHO+HO2↔CH2O+HCO+OH	7.00E+12	0	0
154	CH2CHO+HO2↔CH3CHO+O2	3.00E+12	0	0
155	CH2CHO↔CH3+CO	1.17E+43	-9.8	43799.95
156	CH3CHO↔CH3+HCO	7.00E+15	0	81700.05
157	CH3CO(+M)↔CH3+CO(+M)	3.00E+12	0	16700.05
158	CH3CHO+OH↔CH3CO+H2O	3.37E+12	0	-619.98
159	CH3CHO+OH↔CH2CHO+H2O	3.37E+11	0	-619.98
160	CH3CHO+O↔CH3CO+OH	1.77E+18	-1.9	2979.92
161	CH3CHO+O↔CH2CHO+OH	3.72E+13	-0.2	3559.99
162	CH3CHO+H↔CH3CO+H2	4.66E+13	-0.3	2989.96
163	CH3CHO+H↔CH2CHO+H2	1.85E+12	0.4	5359.94
164	CH3CHO+CH3↔CH3CO+CH4	3.90E-07	5.8	2200.05
165	CH3CHO+CH3↔CH2CHO+CH4	2.45E+01	3.1	5729.92
166	CH3CHO+HO2↔CH3CO+H2O2	3.60E+19	-2.2	14000
167	CH3CHO+HO2↔CH2CHO+H2O2	2.32E+11	0.4	14900.1
168	CH3CHO+O2↔CH3CO+HO2	1.00E+14	0	42200.05
169	C2H5OH(+M)↔CH3+CH2OH(+M)	5.00E+15	0	82000
170	C2H5OH(+M)↔C2H4+H2O(+M)	8.00E+13	0	65000
171	C2H5OH+OH↔CH2CH2OH+H2O	1.81E+11	0.4	717.02
172	C2H5OH+OH↔CH3CHOH+H2O	3.09E+10	0.5	-380.02
173	C2H5OH+OH↔CH3CH2O+H2O	1.05E+10	0.8	717.02
174	C2H5OH+H↔CH2CH2OH+H2	1.90E+07	1.8	5099.9
175	C2H5OH+H↔CH3CHOH+H2	2.58E+07	1.6	2830.07
176	C2H5OH+H↔CH3CH2O+H2	1.50E+07	1.6	3039.91
177	C2H5OH+O↔CH2CH2OH+OH	9.41E+07	1.7	5460.09

Number	Reaction	A	n	E
178	C2H5OH+O↔CH3CHOH+OH	1.88E+07	1.9	1820.03
179	C2H5OH+O↔CH3CH2O+OH	1.58E+07	2	4450.05
180	C2H5OH+CH3↔CH2CH2OH+CH4	2.19E+02	3.2	9619.98
181	C2H5OH+CH3↔CH3CHOH+CH4	7.28E+02	3	7950.05
182	C2H5OH+CH3↔CH3CH2O+CH4	1.45E+02	3	7650.1
183	C2H5OH+HO2↔CH3CHOH+H2O2	8.20E+03	2.5	10799.95
184	C2H5OH+HO2↔CH2CH2OH+H2O2	2.43E+04	2.5	15799.95
185	C2H5OH+HO2↔CH3CH2O+H2O2	3.80E+12	0	24000
186	C2H4+OH↔CH2CH2OH	2.41E+11	0	-2380.02
187	C2H5+HO2↔CH3CH2O+OH	4.00E+13	0	0
188	CH3CH2O+M↔CH3CHO+H+M	5.60E+34	-5.9	25299.95
189	CH3CH2O+M↔CH3+CH2O+M	5.35E+37	-7	23799.95
190	CH3CH2O+O2↔CH3CHO+HO2	4.00E+10	0	1099.9
191	CH3CH2O+CO↔C2H5+CO2	4.68E+02	3.2	5380.02
192	CH3CH2O+H↔CH3+CH2OH	3.00E+13	0	0
193	CH3CH2O+H↔C2H4+H2O	3.00E+13	0	0
194	CH3CH2O+OH↔CH3CHO+H2O	1.00E+13	0	0
195	CH3CHOH+O2↔CH3CHO+HO2	4.82E+13	0	5020.08
196	CH3CHOH+O↔CH3CHO+OH	1.00E+14	0	0
197	CH3CHOH+H↔C2H4+H2O	3.00E+13	0	0
198	CH3CHOH+H↔CH3+CH2OH	3.00E+13	0	0
199	CH3CHOH+HO2↔CH3CHO+2OH	4.00E+13	0	0
200	CH3CHOH+OH↔CH3CHO+H2O	5.00E+12	0	0
201	CH3CHOH+M↔CH3CHO+H+M	1.00E+14	0	25000
202	C3H4+O↔C2H4+CO	2.00E+07	1.8	1000
203	CH3+C2H2↔C3H4+H	2.56E+09	1.1	13643.88
204	C3H4+O↔HCCO+CH3	7.30E+12	0	2250
205	C3H3+H(+M)↔C3H4(+M)	3.00E+13	0	0
206	C3H3+HO2↔C3H4+O2	2.50E+12	0	0
207	C3H4+OH↔C3H3+H2O	5.30E+06	2	2000
208	C3H3+O2↔CH2CO+HCO	3.00E+10	0	2868.07
209	C3H4+H(+M)↔C3H5(+M)	4.00E+13	0	0
210	C3H5+H↔C3H4+H2	1.80E+13	0	0
211	C3H5+O2↔C3H4+HO2	4.99E+15	-1.4	22428.06
212	C3H5+CH3↔C3H4+CH4	3.00E+12	-0.32	-130.98
213	C2H2+CH3(+M)↔C3H5(+M)	6.00E+08	0	0
214	C3H5+OH↔C3H4+H2O	6.00E+12	0	0
215	C3H3+HCO↔C3H4+CO	2.50E+13	0	0
216	C3H3+HO2↔OH+CO+C2H3	8.00E+11	0	0
217	C3H4+O2↔CH3+HCO+CO	4.00E+14	0	41826
218	C3H6+O↔C2H5+HCO	3.50E+07	1.65	-972.75

Number	Reaction	A	n	E
219	C3H6+OH↔C3H5+H2O	3.10E+06	2	-298.28
220	C3H6+O↔CH2CO+CH3+H	1.20E+08	1.65	327.44
221	C3H6+H↔C3H5+H2	1.70E+05	2.5	2492.83
222	C3H5+H(+M)↔C3H6(+M)	2.00E+14	0	0
223	C3H5+HO2↔C3H6+O2	2.66E+12	0	0
224	C3H5+HO2↔OH+C2H3+CH2O	3.00E+12	0	0
225	C2H3+CH3(+M)↔C3H6(+M)	2.50E+13	0	0
226	C3H6+H↔C2H4+CH3	1.60E+22	-2.39	11185.47
227	CH3+C2H3↔C3H5+H	1.50E+24	-2.83	18618.55
228	C3H8(+M)↔CH3+C2H5(+M)	1.10E+17	0	84392.93
229	C3H8+O2↔I-C3H7+HO2	4.00E+13	0	47500
230	C3H8+O2↔N-C3H7+HO2	4.00E+13	0	50932.12
231	C3H8+H↔I-C3H7+H2	1.30E+06	2.4	4471.08
232	C3H8+H↔N-C3H7+H2	1.33E+06	2.54	6761.47
233	C3H8+O↔I-C3H7+OH	4.76E+04	2.71	2107.31
234	C3H8+O↔N-C3H7+OH	1.90E+05	2.68	3718.45
235	C3H8+OH↔N-C3H7+H2O	1.00E+10	1	1599.9
236	C3H8+OH↔I-C3H7+H2O	2.00E+07	-1.6	-99.9
237	C3H8+HO2↔I-C3H7+H2O2	9.64E+03	2.6	13917.3
238	C3H8+HO2↔N-C3H7+H2O2	4.76E+04	2.55	16491.4
239	I-C3H7+C3H8↔N-C3H7+C3H8	8.40E-03	4.2	8675.91
240	C3H6+H(+M)↔I-C3H7(+M)	1.33E+13	0	1560.71
241	I-C3H7+O2↔C3H6+HO2	1.30E+11	0	0
242	N-C3H7(+M)↔CH3+C2H4(+M)	1.23E+13	-0.1	30210.33
243	H+C3H6(+M)↔N-C3H7(+M)	1.33E+13	0	3260.04
244	N-C3H7+O2↔C3H6+HO2	3.50E+16	-1.6	3500
245	N-C3H7+O2↔C3H6OOH	2.00E+12	0	0
246	C3H6OOH↔C3H6+HO2	2.50E+35	-8.3	22000
247	C3H6OOH+O2↔OC3H5OOH+OH	1.50E+08	0	-7000
248	OC3H5OOH↔CH2CHO+CH2O+OH	1.00E+15	0	43000
249	C4H10(+M)↔2C2H5(+M)	2.72E+15	0	75609.94
250	C4H10+O2↔PC4H9+HO2	6.00E+13	0	52340.11
251	C4H10+O2↔SC4H9+HO2	4.00E+13	0	49799.95
252	C4H10+HO2↔PC4H9+H2O2	4.08E+01	3.59	17159.89
253	C4H10+HO2↔SC4H9+H2O2	1.26E+02	3.37	13719.89
254	C4H10+O↔PC4H9+OH	1.13E+14	0	7850
255	C4H10+O↔SC4H9+OH	5.62E+13	0	5200
256	C4H10+OH↔PC4H9+H2O	1.05E+10	0.97	1586.04
257	C4H10+OH↔SC4H9+H2O	9.34E+07	1.61	-34.89
258	C4H10+H↔H2+PC4H9	2.80E+06	2.54	6965.4
259	C4H10+H↔H2+SC4H9	1.69E+06	2.4	4493

Number	Reaction	A	n	E
260	PC4H9↔C2H5+C2H4	3.50E+12	0.463	29469.89
261	SC4H9↔C3H6+CH3	4.80E+10	1.044	30349.9
262	C4H8↔C3H5+CH3	1.00E+16	0	72896.75
263	C4H8+H↔H2+C2H3+C2H4	6.60E+05	2.54	6763.86
264	SC4H9+O2↔SC4H9O2	7.50E+12	0	0
265	SC4H9O2↔C4H8+HO2	5.08E+42	-9.41	41490
266	PC4H9+O2↔C4H8+HO2	8.37E-01	3.59	12000
267	PC4H9+O2↔C4H8OOH1-3	2.00E+12	0	0
268	C4H8OOH1-3↔C4H8+HO2	2.00E+12	0	24000
269	C4H8OOH1-3+O2↔NC4KET13+OH	3.50E+00	2.234	-16560
270	NC4KET13↔N-C3H7+CO2+OH	3.00E+16	0	41500

Appendix B Spherical Diffusion Flame Structure at 1 atm

Most of the plots in Chapters 3 and 4 are presented in mixture fraction space, but it useful to also examine the structure of the flame in physical space. Appendix B considers the flame structure at 1 atm, and Appendix C considers the flame structure at 50 atm.

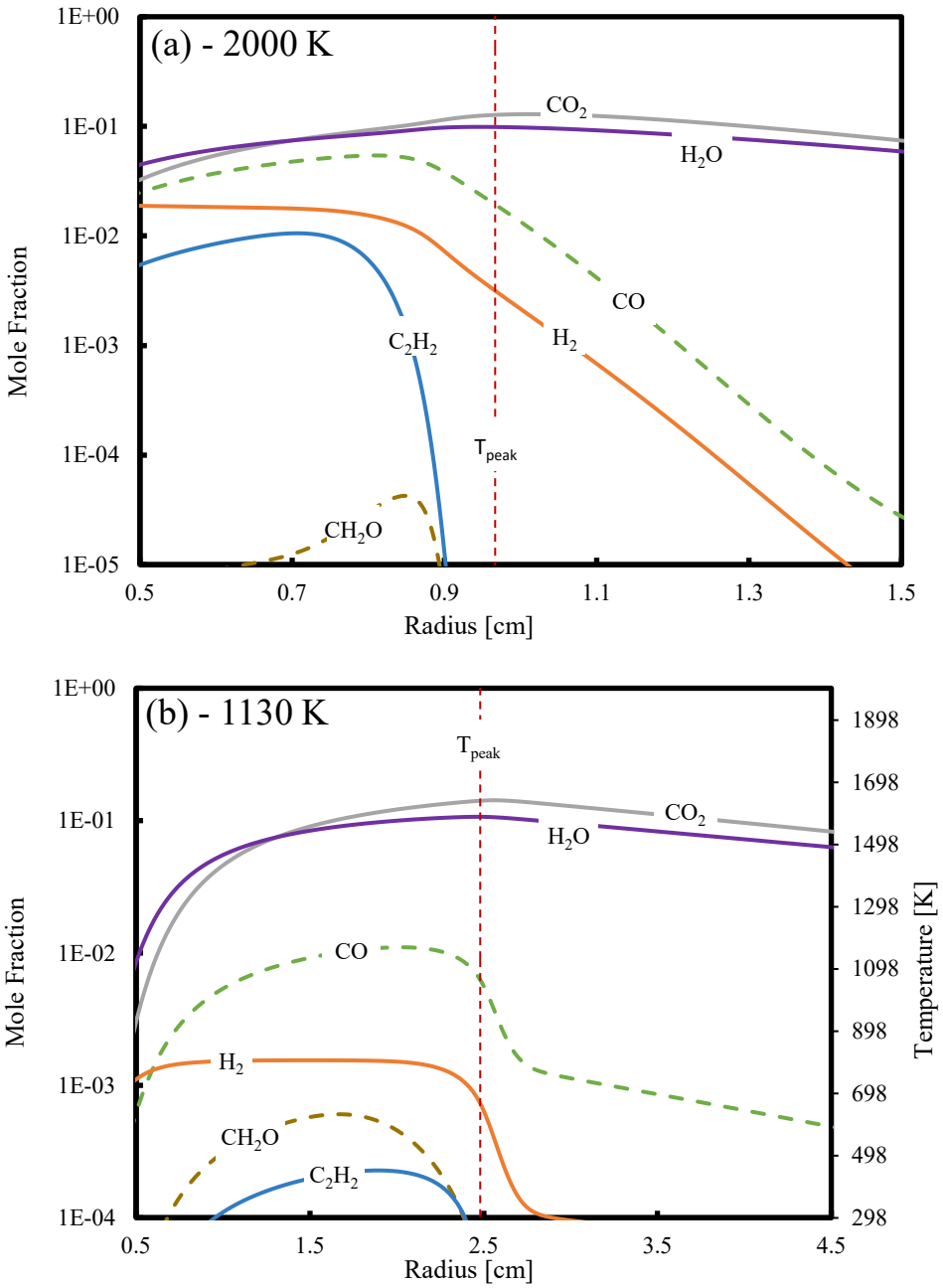

Fig. B.1. Spatial profiles of CO_2, H_2O, CO, H_2, CH_2O, and C_2H_2 mole fractions at (a) 2000 K and (b) 1130 K.

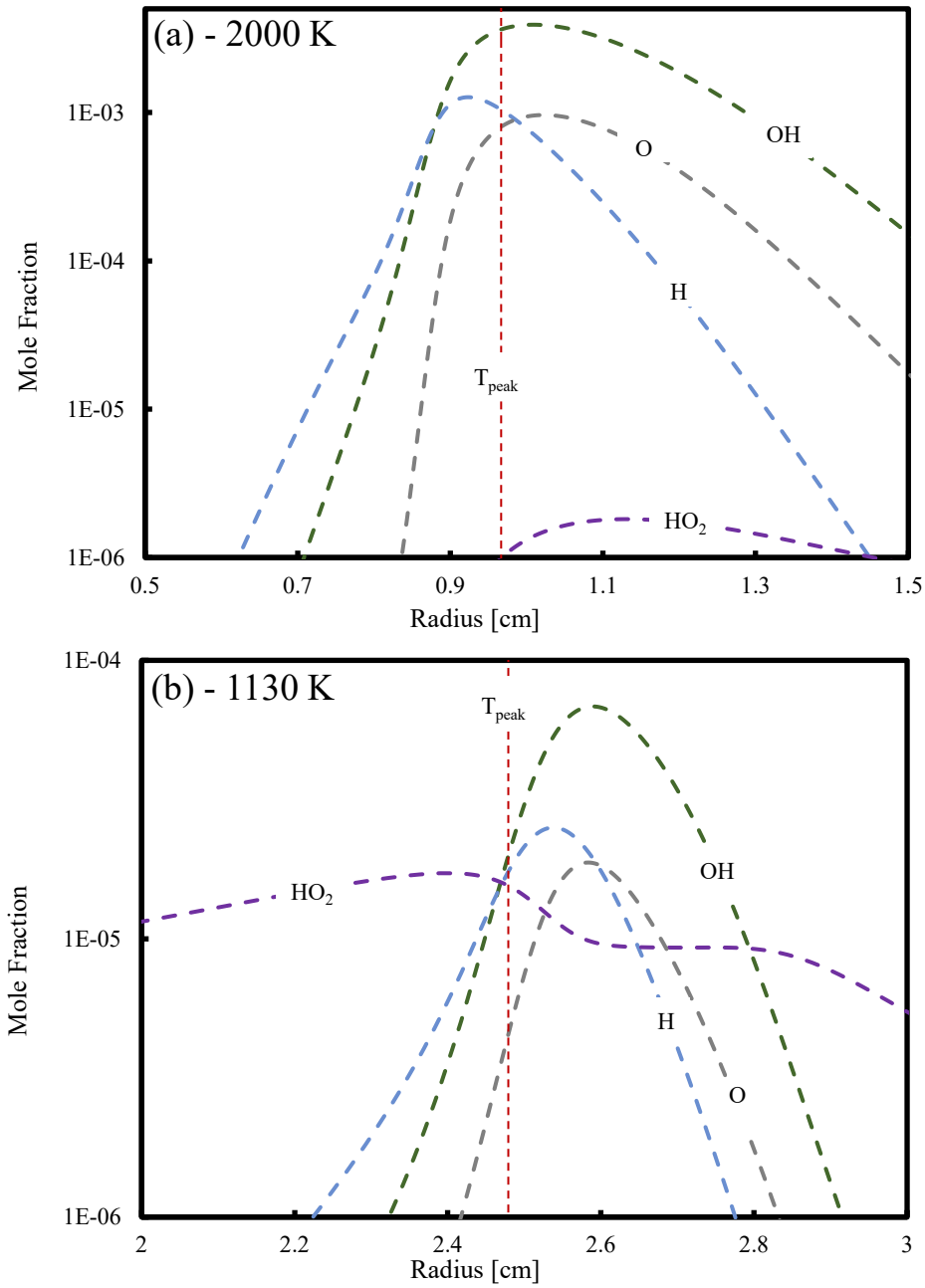

Fig. B.2. Spatial profiles of O, OH, H, and HO_2 mole fractions at (a) 2000 K and (b) 1130 K.

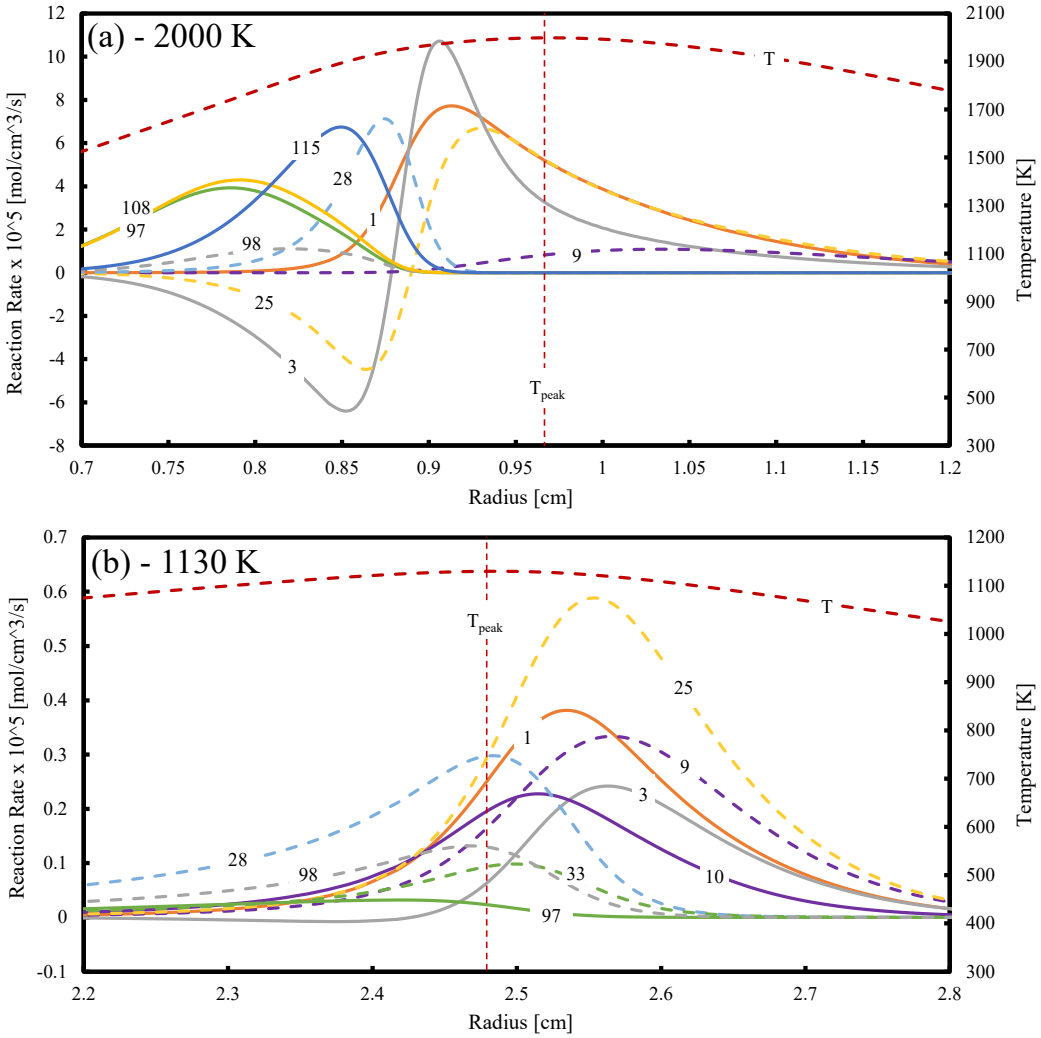

Fig. B.3. Spatial profiles of reaction rate for selected reactions at (a) 2000 K and (b) 1130 K.

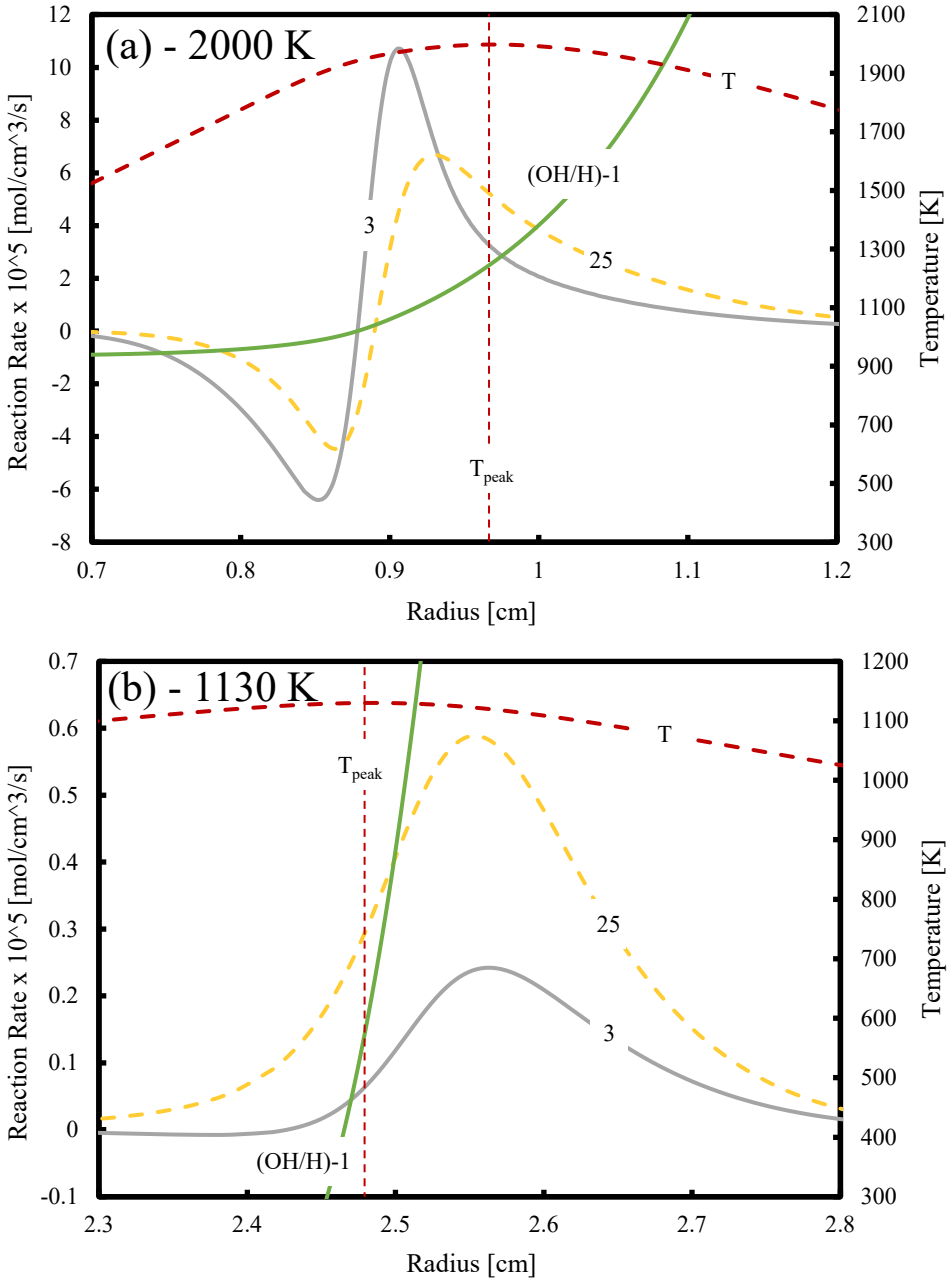

Fig. B.4. Spatial profiles of reactions R3 and R25, temperature, and OH/H ratio at (a) 2000 K and (b) 1130 K.

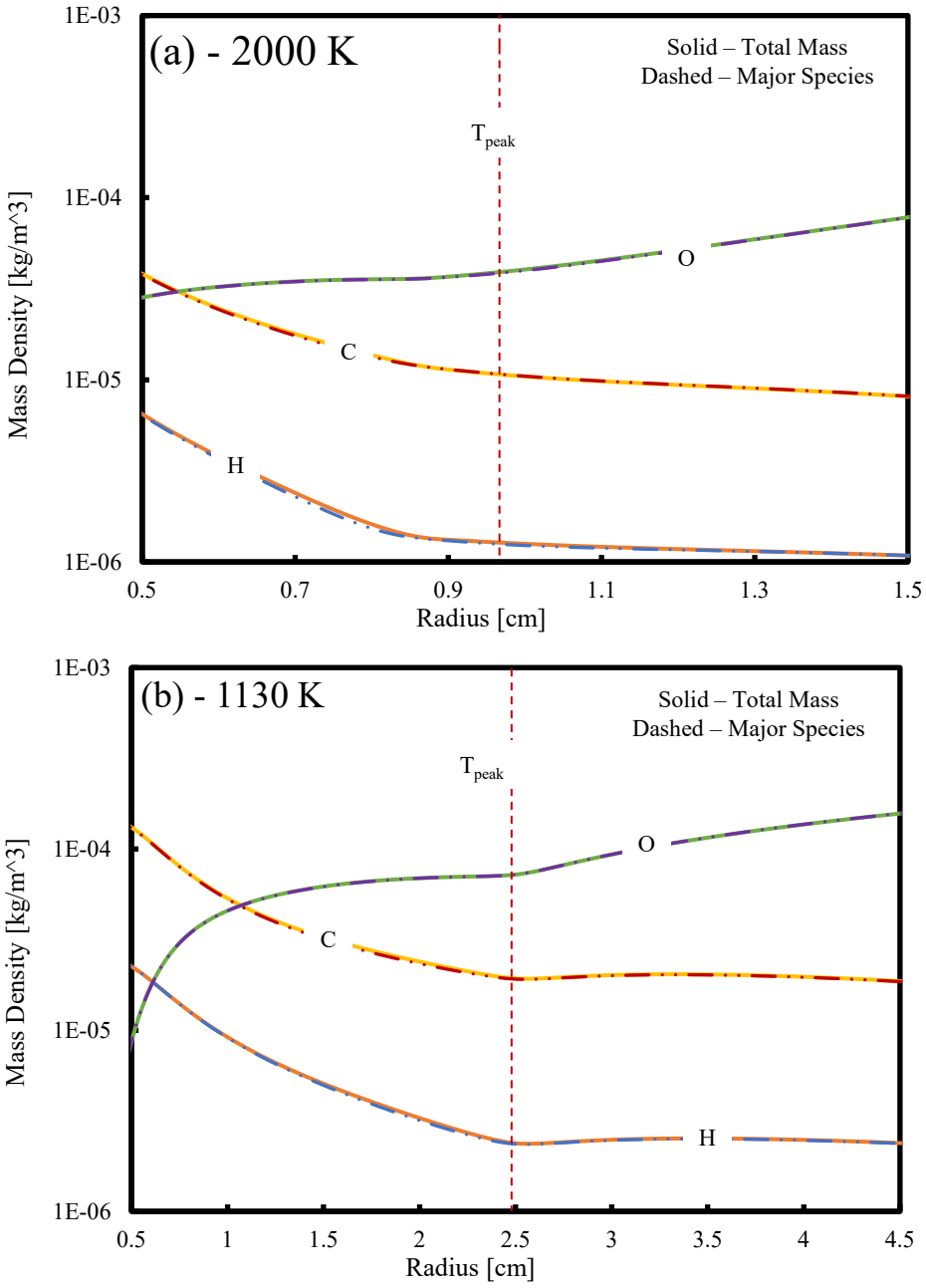

Fig. B.5. Contribution of major species to total C, H, and O atoms in the system at (a) 2000 K and (b) 1130 K.

Appendix C Spherical Diffusion Flame Structure at 50 atm

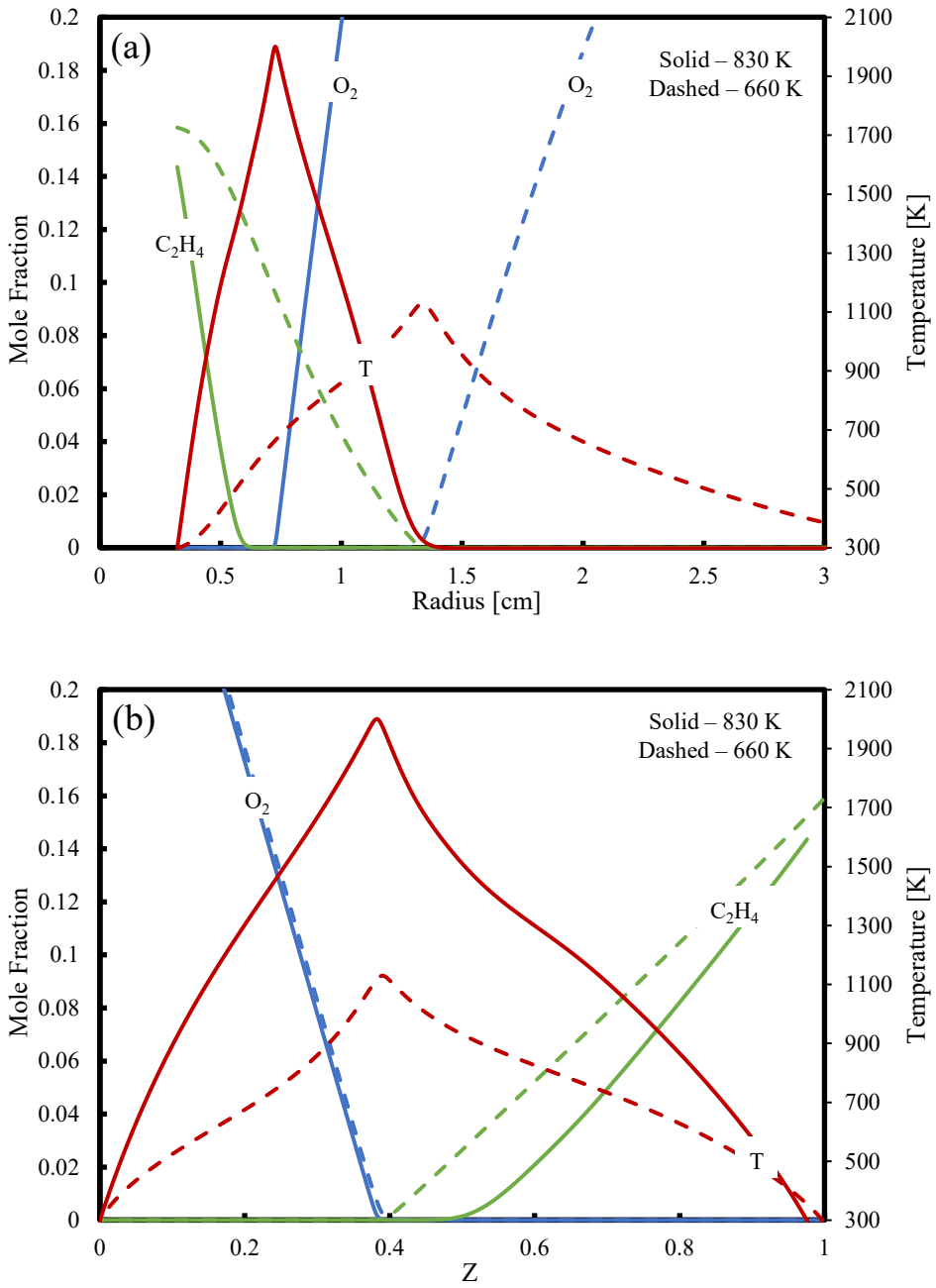

Fig. C.1. Spatial profiles of peak temperature and fuel and oxidizer mole fraction in (a) physical space and (b) mixture fraction space.

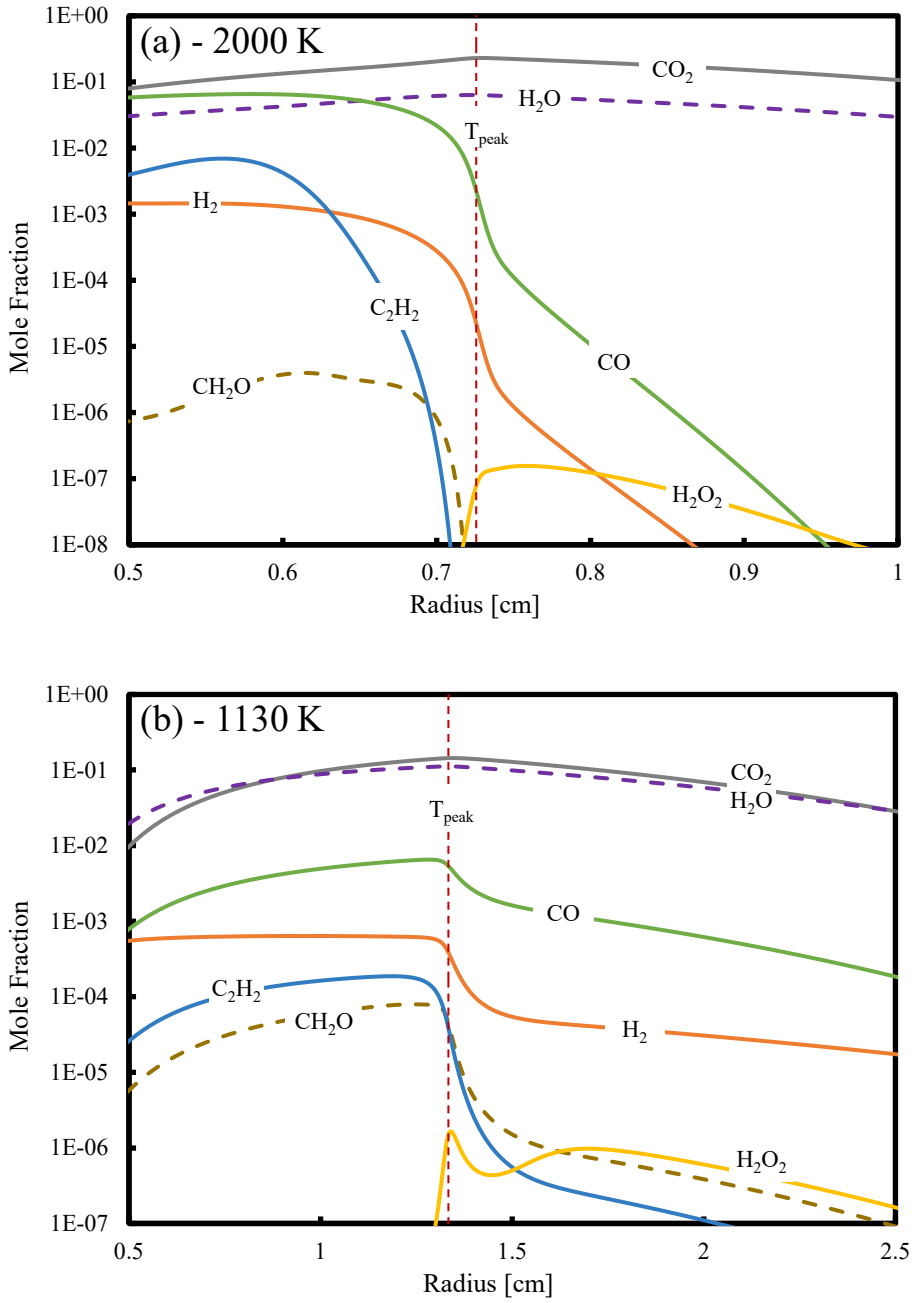

Fig. C.2. Spatial profiles of CO2, H2O, CO, H2, CH2O, C2H2 and H2O2 mole fractions at (a) 2000 and (b) 1130 K.

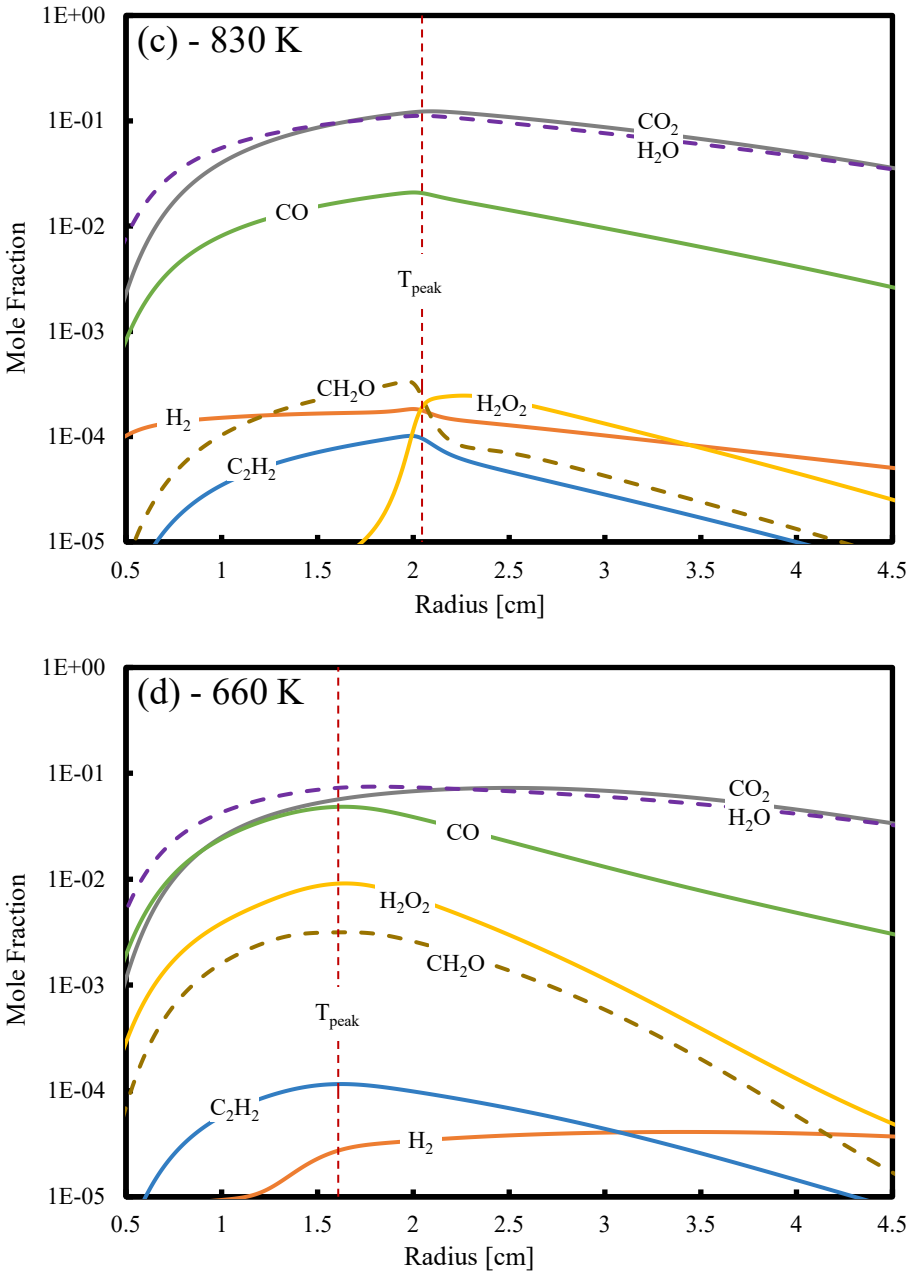

Fig. C.3. Spatial profiles of CO2, H2O, CO, H2, CH2O, C2H2 and H2O2 mole fractions at (c) 830 K and (d) 660 K.

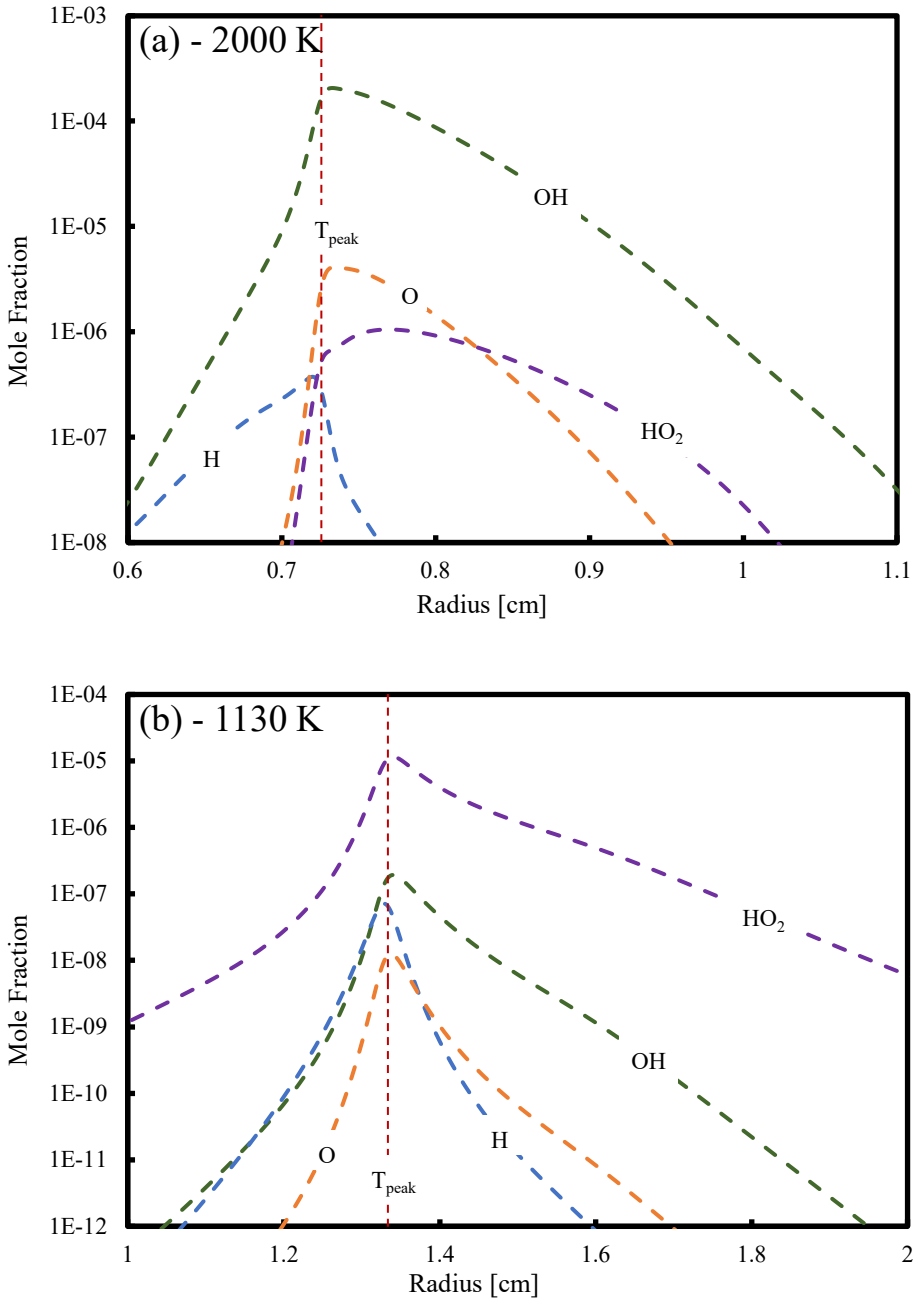

Fig. C.4. Spatial profiles of O, OH, H, and HO_2 mole fractions at (a) 2000 and (b) 1130 K.

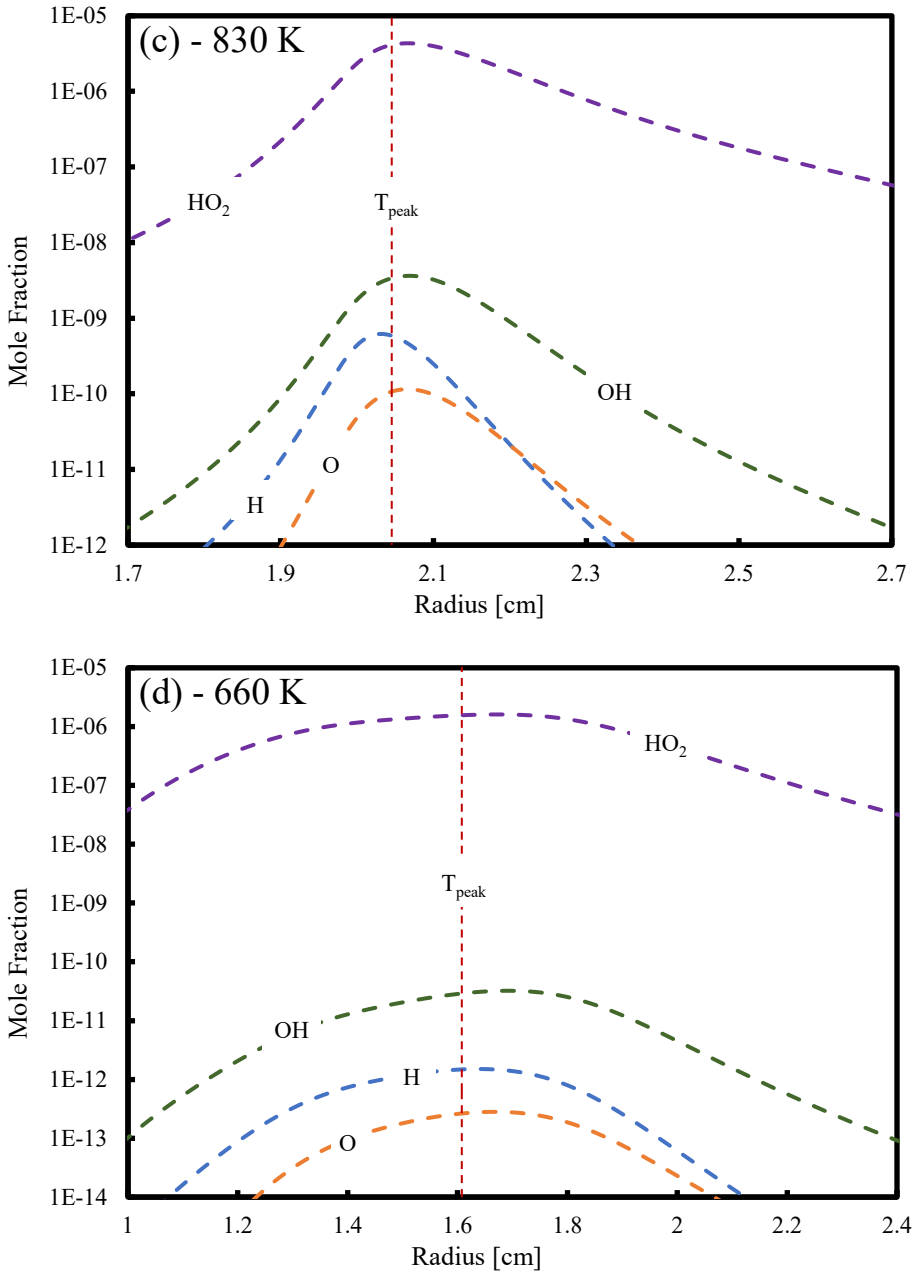

Fig. C.5. Spatial profiles of O, OH, H, and HO_2 mole fractions at (c) 830 K and (d) 660 K.

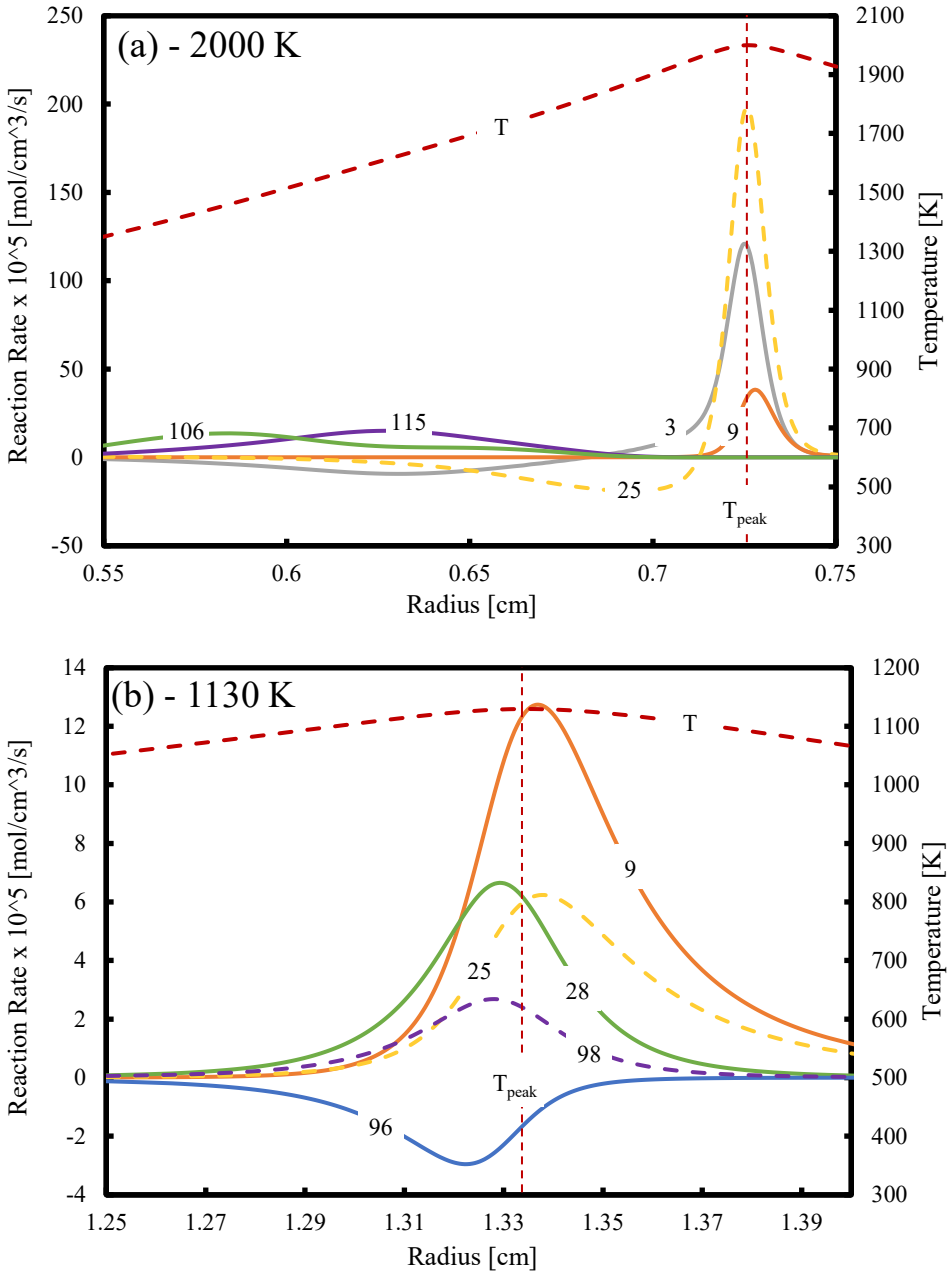

Fig. C.6. Spatial profiles of reaction rate for selected reactions at (a) 2000 and (b) 1130 K.

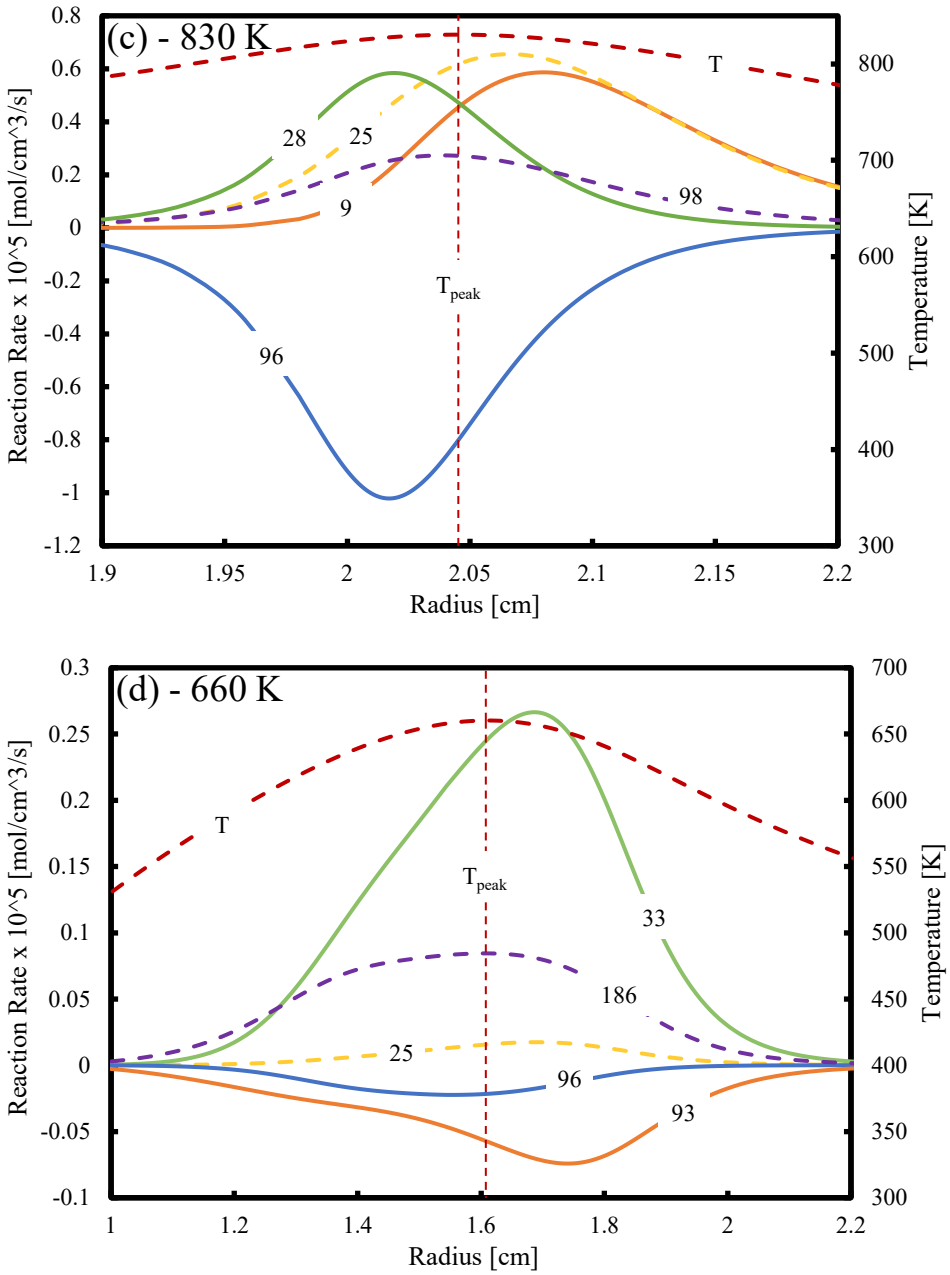

Fig. C.7. Spatial profiles of reaction rate for selected reactions at (c) 830 K and (d) 660 K.

Bibliography

[1] J.B. Heywood, Internal combustion engine fundamentals, Second edition, McGraw-Hill Education, New York, 2018.

[2] W.W. Pulkrabek, ed., Engineering fundamentals of the internal combustion engine, Second edition, Pearson new international edition, Pearson, Harlow, Essex, 2014.

[3] C. Middlecamp, ed., Chemistry in context: applying chemistry to society, 7th ed, McGraw-Hill, Dubuque, 2012.

[4] P.H. Irace, H.J. Lee, K. Waddell, L. Tan, D.P. Stocker, P.B. Sunderland, R.L. Axelbaum, Observations of long duration microgravity spherical diffusion flames aboard the International Space Station, Combust. Flame, 229 (2021) 111373.

[5] P.H. Irace, K.A. Waddell, D. Constales, P.B. Sunderland, R.L. Axelbaum, Critical temperature and reactant mass flux for radiative extinction of ethylene microgravity spherical diffusion flames at 1 bar, Proc. Combust. Inst., (2022) S1540748922000670.

[6] P.H. Irace, K.A. Waddell, D. Constales, M. Kim, G. Yablonsky, P.B. Sunderland, R.L. Axelbaum, On the existence of steady-state gaseous microgravity spherical diffusion flames in the presence of radiation heat loss, Proc. Combust. Inst., (2022) S1540748922000736.

[7] M. Kim, K.A. Waddell, P.B. Sunderland, V. Nayagam, D.P. Stocker, D.L. Dietrich, Y. Ju, F.A. Williams, P. Irace, R.L. Axelbaum, Spherical gas-fueled cool diffusion flames, Proc. Combust. Inst., (2022) S1540748922000414.

[8] S.M. Frolov, V.S. Ivanov, F.S. Frolov, P.A. Vlasov, R. Axelbaum, P.H. Irace, G. Yablonsky, K. Waddell, Soot Formation in Spherical Diffusion Flames, Mathematics, 11 (2023) 261.

[9] K. Mills, M. Matalon, Burner-Generated Spherical Diffusion Flames, Combust. Sci. Technol., 129 (1997) 295–319.

[10] K. Mills, M. Matalon, Extinction of spherical diffusion flames in the presence of radiant loss, Symp. Int. Combust., 27 (1998) 2535–2541.

[11] S.D. Tse, D. Zhu, C.-J. Sung, Y. Ju, C.K. Law, Microgravity burner-generated spherical diffusion flames: experiment and computation‡‡Currently at Department of Mechanical and Aerospace Engineering, Case Western Reserve University, Cleveland, OH 44106, Combust. Flame, 125 (2001) 1265–1278.

[12] Y. Ju, C.B. Reuter, O.R. Yehia, T.I. Farouk, S.H. Won, Dynamics of cool flames, Prog. Energy Combust. Sci., 75 (2019) 100787.

[13] Y. Ju, Understanding cool flames and warm flames, Proc. Combust. Inst., 38 (2021) 83–119.

[14] H. Davy, VIII Some new experiments and observations on the combustion of gaseous mixtures, with an account of a method of preserving a continued light in mixtures of inflammable gases and air without flame, Philos. Trans. R. Soc. Lond., 107 (1817) 77–85.

[15] J.F. Griffiths, S.K. Scott, Thermokinetic interactions: Fundamentals of spontaneous ignition and cool flames, Prog. Energy Combust. Sci., 13 (1987) 161–197.

[16] P.G. Lignola, E. Reverchon, Cool flames, Prog. Energy Combust. Sci., 13 (1987) 75–96.
[17] G. Paczko, N. Peters, K. Seshadri, F.A. Williams, The role of cool-flame chemistry in quasi-steady combustion and extinction of *n*- heptane droplets, Combust. Theory Model., 18 (2014) 515–531.
[18] J.E. Dec, Advanced compression-ignition engines—understanding the in-cylinder processes, Proc. Combust. Inst., 32 (2009) 2727–2742.
[19] T. Jin, Y. Wu, X. Wang, K.H. Luo, T. Lu, K. Luo, J. Fan, Ignition dynamics of DME/methane-air reactive mixing layer under reactivity controlled compression ignition conditions: Effects of cool flames, Appl. Energy, 249 (2019) 343–354.
[20] X. Lu, D. Han, Z. Huang, Fuel design and management for the control of advanced compression-ignition combustion modes, Prog. Energy Combust. Sci., 37 (2011) 741–783.
[21] R.D. Reitz, Directions in internal combustion engine research, Combust. Flame, 160 (2013) 1–8.
[22] R.D. Reitz, G. Duraisamy, Review of high efficiency and clean reactivity controlled compression ignition (RCCI) combustion in internal combustion engines, Prog. Energy Combust. Sci., 46 (2015) 12–71.
[23] S. Saxena, I.D. Bedoya, Fundamental phenomena affecting low temperature combustion and HCCI engines, high load limits and strategies for extending these limits, Prog. Energy Combust. Sci., 39 (2013) 457–488.
[24] D.K. Srivastava, A.K. Agarwal, A. Datta, R.K. Maurya, eds., Advances in Internal Combustion Engine Research, Springer Singapore, Singapore, 2018.
[25] M. Yao, Z. Zheng, H. Liu, Progress and recent trends in homogeneous charge compression ignition (HCCI) engines, Prog. Energy Combust. Sci., 35 (2009) 398–437.
[26] C.S. Yoo, T. Lu, J.H. Chen, C.K. Law, Direct numerical simulations of ignition of a lean n-heptane/air mixture with temperature inhomogeneities at constant volume: Parametric study, Combust. Flame, 158 (2011) 1727–1741.
[27] A. Atreya, S. Agrawal, K. Sacksteder, H. Baum, Observations of methane and ethylene diffusion flames stabilized around a blowing porous sphere under microgravity conditions, in: 32nd Aerosp. Sci. Meet. Exhib., American Institute of Aeronautics and Astronautics, Reno,NV,U.S.A., 1994.
[28] A. Atreya, S. Agrawal, Effect of radiative heat loss on diffusion flames in quiescent microgravity atmosphere, Combust. Flame, 115 (1998) 372–382.
[29] S. Tang, M.K. Chernovsky, H.G. Im, A. Atreya, A computational study of spherical diffusion flames in microgravity with gas radiation Part I: Model development and validation, Combust. Flame, 157 (2010) 118–126.
[30] S. Tang, H.G. Im, A. Atreya, A computational study of spherical diffusion flames in microgravity with gas radiation Part II: Parametric studies of the diluent effects on flame extinction, Combust. Flame, 157 (2010) 127–136.
[31] K.J. Santa, Z. Sun, B.H. Chao, P.B. Sunderland, R.L. Axelbaum, D.L. Urban, D.P. Stocker, Numerical and experimental observations of spherical diffusion flames, Combust. Theory Model., 11 (2007) 639–652.

[32] K. Santa, B. Chao, P. Sunderland, D. Urban, D. Stocker, R. Axelbaum, Radiative extinction of gaseous spherical diffusion flames in microgravity, Combust. Flame, 151 (2007) 665–675.
[33] V.R. Lecoustre, Numerical Investigations of Gaseous Spherical Diffusion Flames, PhD Dissertation, University of Maryland, 2009.
[34] V.R. Lecoustre, P.B. Sunderland, B.H. Chao, R.L. Axelbaum, Numerical investigation of spherical diffusion flames at their sooting limits, Combust. Flame, 159 (2012) 194–199.
[35] V.R. Lecoustre, P.B. Sunderland, B.H. Chao, R.L. Axelbaum, Modeled quenching limits of spherical hydrogen diffusion flames, Proc. Combust. Inst., 34 (2013) 887–894.
[36] A. Markan, P.B. Sunderland, J.G. Quintiere, J.L. de Ris, H.R. Baum, Measuring heat flux to a porous burner in microgravity, Proc. Combust. Inst., 37 (2019) 4137–4144.
[37] A. Markan, H.R. Baum, P.B. Sunderland, J.G. Quintiere, J.L. de Ris, Transient ellipsoidal combustion model for a porous burner in microgravity, Combust. Flame, 212 (2020) 93–106.
[38] J.D. Maun, P.B. Sunderland, D.L. Urban, Thin-filament pyrometry with a digital still camera, Appl. Opt., 46 (2007) 483.
[39] B. Ma, G. Wang, G. Magnotti, R.S. Barlow, M.B. Long, Intensity-ratio and color-ratio thin-filament pyrometry: Uncertainties and accuracy, Combust. Flame, 161 (2014) 908–916.
[40] J. Tinajero, D. Giassi, D.P. Stocker, M.B. Long, Experimental study on the influence of gravity on highly diluted and sooting coflow flames, in: 2019.
[41] D. Giassi, B. Liu, M.B. Long, Use of high dynamic range imaging for quantitative combustion diagnostics, Appl. Opt., 54 (2015) 4580.
[42] P.B. Kuhn, B. Ma, B.C. Connelly, M.D. Smooke, M.B. Long, Soot and thin-filament pyrometry using a color digital camera, Proc. Combust. Inst., 33 (2011) 743–750.
[43] M.B. Long, Optical multi-channel analyzer 2 (OMA2) for Mac OS X, (2019).
[44] R.J. Kee, J.F. Grcar, M.D. Smooke, J.A. Miller, E. Meeks, Premix: A FORTRAN Program for Modeling Steady Laminar One-Dimensional Premixed Flames, (1987).
[45] Chemical-Kinetic Mechanisms for Combustion Applications, San Diego Mech. Web Page Mech. Aerosp. Eng. Combust. Res. Univ. Calif. San Diego Httpcombustionucsdedu, (n.d.).
[46] S.A. Skeen, G. Yablonsky, R.L. Axelbaum, Characteristics of non-premixed oxygen-enhanced combustion: I The presence of appreciable oxygen at the location of maximum temperature, Combust. Flame, 156 (2009) 2145–2152.
[47] C.J. Sun, C.J. Sung, H. Wang, C.K. Law, On the structure of nonsooting counterflow ethylene and acetylene diffusion flames, Combust. Flame, 107 (1996) 321–335.
[48] D. Constales, G.S. Yablonsky, G.B. Marin, The C-matrix: Augmentation and reduction in the analysis of chemical composition and structure, Chem. Eng. Sci., 110 (2014) 164–168.

[49] J.C. Prince, F.A. Williams, Short chemical-kinetic mechanisms for low-temperature ignition of propane and ethane, Combust. Flame, 159 (2012) 2336–2344.
[50] J.R. Abbott, S.A. Miller, Observation of Cool Flames with Ethylene, Nature, 168 (1951) 474–475.
[51] Y. Ju, J.K. Lefkowitz, C.B. Reuter, S.H. Won, X. Yang, S. Yang, W. Sun, Z. Jiang, Q. Chen, Plasma Assisted Low Temperature Combustion, Plasma Chem. Plasma Process., 36 (2016) 85–105.
[52] J.C. Prince, C. Treviño, F.A. Williams, A reduced reaction mechanism for the combustion of n-butane, Combust. Flame, 175 (2017) 27–33.
[53] A. Cuoci, M. Mehl, G. Buzzi-Ferraris, T. Faravelli, D. Manca, E. Ranzi, Autoignition and burning rates of fuel droplets under microgravity, Combust. Flame, 143 (2005) 211–226.
[54] V. Nayagam, D.L. Dietrich, P. V. Ferkul, M.C. Hicks, F.A. Williams, Can cool flames support quasi-steady alkane droplet burning?, Combust. Flame, 159 (2012) 3583–3588.
[55] T.I. Farouk, F.L. Dryer, Isolated n-heptane droplet combustion in microgravity: "Cool Flames" - Two-stage combustion, Combust. Flame, 161 (2014) 565–581.
[56] V. Nayagam, D.L. Dietrich, M.C. Hicks, F.A. Williams, Cool-flame extinction during n-alkane droplet combustion in microgravity, Combust. Flame, 162 (2015) 2140–2147.
[57] D.L. Dietrich, R. Calabria, P. Massoli, V. Nayagam, F.A. Williams, Experimental Observations of the Low-Temperature Burning of Decane/Hexanol Droplets in Microgravity, Combust. Sci. Technol., 189 (2017) 520–554.
[58] T.I. Farouk, D. Dietrich, F.L. Dryer, Three stage cool flame droplet burning behavior of n-alkane droplets at elevated pressure conditions: Hot, warm and cool flame, Proc. Combust. Inst., 37 (2019) 3353–3361.
[59] V. Nayagam, F.A. Williams, D.L. Dietrich, Asymptotic analysis of cool-flame propagation in mixtures of an n-alkane, oxygen, and nitrogen, Combust. Theory Model., (2021) 1–13.
[60] S.H. Won, B. Jiang, P. Diévart, C.H. Sohn, Y. Ju, Self-sustaining n -heptane cool diffusion flames activated by ozone, Proc. Combust. Inst., 35 (2015) 881–888.
[61] C.B. Reuter, M. Lee, S.H. Won, Y. Ju, Study of the low-temperature reactivity of large n-alkanes through cool diffusion flame extinction, Combust. Flame, 179 (2017) 23–32.
[62] C.H. Sohn, H.S. Han, C.B. Reuter, Y. Ju, S.H. Won, Thermo-kinetic dynamics of near-limit cool diffusion flames, Proc. Combust. Inst., 36 (2017) 1329–1337.
[63] A. Alfazazi, A. Al-Omier, A. Secco, H. Selim, Y. Ju, S.M. Sarathy, Cool diffusion flames of butane isomers activated by ozone in the counterflow, Combust. Flame, 191 (2018) 175–186.
[64] O.R. Yehia, C.B. Reuter, Y. Ju, On the chemical characteristics and dynamics of n-alkane low-temperature multistage diffusion flames, Proc. Combust. Inst., 37 (2019) 1717–1724.

[65] M. Lee, Y. Fan, Y. Ju, Y. Suzuki, Ignition characteristics of premixed cool flames on a heated wall, Combust. Flame, 231 (2021) 111476.
[66] P. Zhao, C.K. Law, The role of global and detailed kinetics in the first-stage ignition delay in NTC-affected phenomena, Combust. Flame, 160 (2013) 2352–2358.
[67] K. Seshadri, N. Peters, F.A. Williams, V. Nayagam, G. Paczko, Asymptotic analysis of quasi-steady *n* -heptane droplet combustion supported by cool-flame chemistry, Combust. Theory Model., 20 (2016) 1118–1130.
[68] PubChem, Compound Summary for CID 15600, Decane, (2022).
[69] M. Hajilou, M.Q. Brown, M.C. Brown, E. Belmont, Investigation of the structure and propagation speeds of n-heptane cool flames, Combust. Flame, 208 (2019) 99–109.
[70] M.C. Brown, E.L. Belmont, Experimental characterization of ozone-enhanced n-decane cool flames and numerical investigation of equivalence ratio dependence, Combust. Flame, 230 (2021) 111429.